

Investigation of the Wetting Behavior of Cerium Dioxide Coatings

BY

SIN PUI FU

B.S., University of Illinois at Chicago, 2012

THESIS

Submitted as partial fulfillment of the requirements
for the degree of Doctor of Philosophy in Mechanical Engineering
in the Graduate College of the
University of Illinois at Chicago, 2016

Chicago, Illinois

Defense Committee:

Professor Jeremiah Abiade, chair and advisor
Professor W.J Minkowycz
Professor Alexander L. Yarin
Professor Yayue Pan
Professor Christos G. Takoudis, chemical engineering

ACKNOWLEDGMENTS

I would like to express the deepest appreciation to my advisor, Professor Jeremiah Abiade, who mentored me in this area of material science. I would thank him for all of his thoughtful advice and invaluable guidance to me in my 5 years of study at the University of Illinois at Chicago. I would also like to formally thank Dr. W.J. Minkowycz, Dr. Alexander L. Yarin, Dr. Yayue Pan and Dr. Christos G. Takoudis for their time and effort to review this manuscript. I would like to especially thank Professor Takoudis and his student, J. Rossero, for their assistance with x-ray photoelectron spectroscopy characterization. In addition, I would also like to thank for Professor Yarin and his post-doc, Rakesh Prasad Sahu, for their assistance in setting up the bouncing experiments.

I want to acknowledge the Nanotechnology Core Facility (NCF) at University of Illinois at Chicago for the assistance with optical profiler measurements, atomic force microscopy and scanning electron microscopy. I also acknowledge NUANCE at Northwestern University for their assistance with x-ray photoelectron spectroscopy.

I want to acknowledge Chen Chen for his contribution in this thesis. He took the scan electrons microscopy images for the cerium dioxide thin films, titanium doped cerium dioxide thin films, superhydrophobic cerium dioxide coating and cerium dioxide nano-composite coating.

I have enjoyed the friendship Chen Chen and Riad Alzghier during my graduate study. It has been my pleasure to spend this wonderful time with them. Finally, I would like to express my greatest love to my parents for their kind support.

TABLE OF CONTENTS

<u>CHAPTER</u>	<u>PAGE</u>
I. Introduction.....	1
A. Motivation	1
B. Introduction to Research	1
C. Organization of Thesis	2
II. Literature Review.....	4
A. Wetting Behavior and Contact Angle	4
1. Static Contact Angle	4
2. Contact Angle Hysteresis (CAH)	5
3. Roll-off Angle	5
B. Types of Wetting: Wenzel State and Cassie-Baxter State.....	6
1. The Challenges to Wenzel model.....	9
2. Influence of Temperature, Pressure, Humidity and Vibration.....	11
3. Challenges in Measuring Contact Angle.....	12
4. Dynamic Wetting of Surfaces: Water Droplets Bouncing on Surfaces.....	14
C. Hydrophobicity in Metals, Polymers, Oxides	16
D. The Properties of Ceria and its Application	17
1. Oxygen Vacancy and Surface Defects of Ceria.....	18
2. The bandgap of Ceria.....	19
E. Photocatalytic Activity and Reversible Wetting Behavior.....	20
F. Annealing Treatment on Ceria	22
G. Applications for Superhydrophobic Surfaces.....	22
1. Self-Cleaning.....	23
2. Heat Transfer.....	23
3. Anti-Bacteria.....	24
4. Anti-Icing.....	25
H. Fabrication Methods of Superhydrophobic Surface.....	27
1. Lithography.....	27
2. Deposition.....	28
3. Etching.....	29
I. Research Objectives.....	30
III. Materials and Methods.....	30
A. Pulsed Laser Deposition	30
B. Wettability Characterization	31

C.	Bouncing Experiment	33
D.	Surface Morphology Characterization	34
E.	X-ray Photoelectron Spectroscopy.....	34
1.	Peak Fit of Ce 3d Spectrum.....	36
2.	Peak Fit of O 1s Spectrum.....	37
3.	Peak Fit of C 1s Spectrum.....	37
F.	Ultraviolet (UV) Irradiation Treatment.....	38
G.	Annealing Treatment	39
H.	Durability Test.....	39
I.	Stability Test.....	39
J.	Ice Accumulation Test.....	40
K.	Nano-Structure Synthesis Method.....	41
IV.	Wetting Behavior of Ceria Films.....	42
A.	The Effect of Oxygen Partial Pressure and Substrate Temperature on the Wetting Behavior of Ceria Films	43
1.	Roughness of Ceria Thin Films.....	44
2.	The Crystal Structure of Ceria Thin Films Grown by PLD.....	45
3.	Compositional Analysis by XPS.....	46
B.	The Effect of UV Irradiation Treatment in Air on Wetting Behavior of Ceria Films.....	48
1.	XPS Results for Ceria Films Exposed to UV Irradiation Treatment in Air...	49
C.	The Effect of Annealing Treatment in Air on Wetting Behavior of Ceria Films...	51
1.	XPS Results for Ceria Films Annealing in Air.....	52
D.	Wetting Behavior of CeO ₂ Films Storage in Air and Vacuum.....	53
1.	XPS Results for CeO ₂ Films Storage in Vacuum.....	55
V.	UV Irradiation Effect on the Titanium Doped Cerium Films.....	57
A.	The Effect of Electronegativity and Hydrophobicity in Oxides.....	58
1.	Roughness of the Titanium Doped Cerium Films.....	59
2.	XPS Results for the Titanium Doped Cerium Films.....	59
B.	UV Irradiation Activity and Wetting Behavior on the Titanium Doped Cerium Films.....	62
1.	Wetting Characteristics in UV Irradiation Effect.....	62
2.	XPS Results for Titanium Doped Cerium Films exposed to UV Irradiation in Air.....	64
VI.	Fabrication of Cerium Dioxide Superhydrophobic Surface by Hydrothermal Method.....	69
A.	Wetting Behavior of Superhydrophobic Cerium Dioxide Surface.....	70

1.	Water Static Contact Angle Measurements	71
2.	Contact Angle Hysteresis and Roll-off Angle Measurements.....	71
3.	Anti-icing Behavior.....	73
B.	Surface Morphology and Surface Chemistry for the Cerium Dioxide Superhydrophobic Surface.....	74
1.	Stoichiometry of the Superhydrophobic Cerium Dioxide Surface...	75
2.	Surface Roughness of the Superhydrophobic Cerium Dioxide Surface.....	77
3.	Surface Morphology of the Superhydrophobic Cerium Dioxide Surface.....	77
C.	Dynamic Effect of Superhydrophobic Cerium Dioxide Surface.....	79
VII. Fabrication of Chemical and Thermal Stable Cerium Dioxide Nano-composite Superhydrophobic Surface.....		83
A.	Wetting Behavior of Cerium Dioxide Nano-composite Coating.....	84
1.	Surface Roughness and Surface Morphology of Cerium Dioxide Nano-composite Coating.....	85
B.	Stability of Cerium Dioxide Nano-composite Coating.....	86
1.	Stability in Boiling Conditions.....	87
2.	Chemical Stability in Acidic Conditions.....	88
2.	Chemical Stability in Base Conditions.....	89
C.	Dynamic Wetting of Nano-composite Coating.....	91
1.	Observation of Water Droplet Bouncing at Room Temperature.....	91
2.	Observation of Water Droplet Bouncing at sub-Zero Temperature.....	92
VIII. Fabrication of Mechanically Durable Superhydrophobic Cerium Dioxide Surfaces.....		94
A.	Wetting Behavior of Improved Mechanically Durable Superhydrophobic Cerium Dioxide Surface.....	95
1.	Surface Roughness and Surface Morphology.....	96
2.	Observation of Water Droplet Bouncing at Room Temperature.....	97
3.	Observation of Water Droplet Bouncing at sub-Zero Temperature.....	98
B.	Durability of Cerium Dioxide Nano-composite Coating.....	99
1.	Peels Test.....	99
2.	Abrasion Test.....	101
3.	UV Irradiation Effect.....	103
IX.	Summary, Conclusion and Ongoing Work.....	107
References.....		109

VITA.....	117
------------------	------------

LIST OF TABLES

<u>TABLE</u>	<u>PAGE</u>
1. Relative concentration of various surface species on ceria thin films of the UV irradiation treatment in air.....	50
2. Relative concentration of various surface species on ceria thin films of the annealing heat treatment at 200 °C in air.....	53
3. Relative concentration of various surface species on ceria thin films of after 5 days of storage in vacuum and after 1 week exposure in air.....	56
4. Relative concentration of various surface species on Ti doped CeO ₂ thin films which deposited in vacuum at 200 °C.....	61
5. Electronegative for TiO ₂ and CeO ₂	62
6. The surface roughness for the cerium dioxide nano-particles in different reaction time.....	77

LIST OF FIGURES

<u>FIGURE</u>	<u>PAGE</u>
1. Schematic depiction of (a) static contact angle, (b) contact angle hysteresis and (c) roll-off angle	5
2. Schematic depiction of surface tension	6
3. Schematic depiction of (a) solid-liquid state, (b) Cassie-Baxter state and (c) Wenzel state	9
4. Schematic depiction of the amphiphile's head and amphiphile's tail effect on the vertical surface and horizontal surface.....	10
5. Morphology of drop impact on dry surface: (a) deposition, (b) prompt splash, (c) corona splash, (d) receding break-up, (e) partial rebound and (f) complete rebound.....	16
6. Schematic depiction of photocatalytic activity on TiO ₂	22
7. General fabrication techniques for forming superhydrophobic surfaces.....	27
8. Schematic depiction of pulsed laser deposition.....	31
9. Image showing custom apparatus used to measure water contact angle.....	32
10. Schematic depiction of (a) advancing contact angle and (b) receding contact angle measurement.....	33
11. Schematic of the drop impact experimental setup.....	34
12. Schematic depiction of X-ray photoelectron spectroscopy.....	35
13. Ce 3d XPS peaks for CeO ₂ films.....	36
14. O 1s XPS peak for CeO ₂ films.....	37
15. C 1s XPS peaks for CeO ₂ films.....	37
16. Image of showing custom apparatus used to ice accumulation test.....	40
17. Image of showing hydrothermal nano-particles synthesis setup.....	41

18.	(a) Wetting behavior of ceria thin films on the effect of substrate temperature and oxygen partial pressure and (b) time-dependent exposure in air to wetting behavior of ceria thin films deposited at 200 °C in vacuum.....	44
19.	Roughness of ceria thin films deposited in different partial pressure.....	45
20.	XRD diffraction pattern for ceria thin films deposited in vacuum and 50 mTorr oxygen at 200 °C	46
21.	XPS spectrum for the ceria thin films grown in different oxygen partial pressure at 200 °C (a) Ce 3d, (b) O 1s and (c) C 1s. The XPS spectrum was collected in different time after the deposition for the samples grown in vacuum (d) Ce 3d, (e) O 1s and (f) C 1s.....	48
22.	(a) The reversible wetting behavior over 72 hours after UV irradiation treatment in air. (b) The wetting behavior after 6 cycles of UV irradiation treatment in air.....	49
23.	XPS spectrum for the ceria thin films of the UV irradiation treatment in air (a) Ce 3d, (b) O 1s and (c) C 1s.....	51
24.	The wetting behavior after 6 cycles of annealing heat treatment at 200 °C in air.....	52
25.	XPS spectrum for the ceria thin films of the annealing heat treatment at 200 °C in air (a) Ce 3d, (b) O 1s and (c) C 1s.....	53
26.	The wetting behavior of ceria thin films storage in vacuum for 5 days and after exposure to ambient air for 1 week.....	55
27.	XPS spectrum for the ceria thin films of after 5 days of storage in vacuum and after 1 week exposure in air (a) Ce 3d, (b) O 1s and (c) C 1s.....	56
28.	Wetting behavior of Ti doped CeO ₂ thin films for those samples were deposited at 200 °C in vacuum condition.....	58
29.	Roughness of Ti doped CeO ₂ thin films which deposited in vacuum at 200 °C	59
30.	XPS spectrum for Ti doped CeO ₂ thin films which deposited in vacuum at 200 °C (a) C 1s, (b) O 1s, (c) Ti 2p and (d) Ce 3d.....	62
31.	(a) The wetting behavior after UV irradiation treatment in ambient condition for Ti doped CeO ₂ thin films. (b) Wetting behavior in 6 cycles of UV irradiation for the Ti doped CeO ₂ thin films.....	64

32.	XPS spectrum for Ti 50 CeO ₂ 15 thin films after the UV irradiation treatment in air. (a) C 1s, (b) O 1s, (c) Ti 2p and (d) Ce 3d.....	66
33.	XPS spectrum for Ti 50 CeO ₂ 30 thin films after the UV irradiation treatment in air. (a) C 1s, (b) O 1s, (c) Ti 2p and (d) Ce 3d.....	66
34.	XPS spectrum for CeO ₂ 50 thin films after the UV irradiation treatment in air. (a) C 1s, (b) O 1s, (c) Ti 2p and (d) Ce 3d.....	67
35.	Static contact angle measurement for the superhydrophobic cerium dioxide surface stearic acid treatment.....	71
36.	Wetting behavior for the cerium dioxide superhydrophobic coating after stearic acid treatment: (a) roll-off angle measurement and (b) contact angle hysteresis.....	72
37.	The anti-icing behavior for the superhydrophobic cerium dioxide surface.....	74
38.	The XPS spectra for (a) C 1s, (b) O 1s, (c) Al 2p and (d) Ce 3d before and after the stearic acid treatment.....	76
39.	Scan electron microscopy images for the cerium dioxide nano-particles which synthesis in different reaction time, (a) 1.5 hours, (b) 3 hours, (c) 12 hours and (d) 24 hours.....	78
40.	Schematic depiction of the cerium dioxide nano-particles coating on aluminum alloy substrate with Cassie-Baxter state.....	79
41.	Bouncing effect on cerium dioxide nano-particles surface at room temperature with impact velocity of 1.98 m/s.....	80
42.	Bouncing effect on cerium dioxide nano-particles surface at -25 with impact velocity of 1.98 m/s.....	81
43.	The wetting behavior for the novel superhydrophobic cerium dioxide nano-composite coating: static contact angle, contact angle hysteresis and surface roughness.....	85
44.	(a) The optical profiler results and (b) surface morphology for the cerium dioxide nano-composite coating.....	86
45.	Boiling test results for cerium dioxide nano-composite coating (a) top view of the surface, (b) static contact angle and (c) contact angle hysteresis.....	88
46.	Immersion in acidic test results for cerium dioxide nano-composite coating (a) top view , (b) static contact angle and (c) contact angle hysteresis.....	89

47.	Immersion in base test results for cerium dioxide nano-composite coating (a) top view of the surface, (b) static contact angle and (c) contact angle hysteresis.....	91
48.	Bouncing behavior of a novel cerium dioxide nano-composite coating on mirror like aluminum alloy at room temperature.....	92
49.	Bouncing behavior of a novel cerium dioxide nano-composite coating on mirror like aluminum alloy at -25	92
50.	The wetting behavior for the refined cerium dioxide nano-composite superhydrophobic coating on etched aluminum alloy surface: static contact angle, contact angle hysteresis and surface roughness.....	96
51.	The TEM images for the cerium dioxide nano-particles size.....	97
52.	Bouncing behavior of a novel cerium dioxide nano-composite on etched aluminum alloy at room temperature.....	98
53.	Bouncing behavior of a novel cerium dioxide nano-composite coating on etched aluminum alloy at -25	98
54.	The wetting behavior for the refined cerium dioxide nano-composited coating after the tape test, (a) static contact angle and (b) contact angle hysteresis.....	100
55.	The surface roughness and the surface morphology for the refined cerium dioxide nano-composited coating after the tape test.....	101
56.	The wetting behavior for the refined cerium dioxide nano-composited coating after the mechanical abrasion test, (a) static contact angle and (b) contact angle hysteresis.....	102
57.	The surface roughness and the surface morphology for the refined cerium dioxide nano-composited coating after the mechanical abrasion test.....	103
58.	The UV irradiation in wetting behavior of refined cerium dioxide nano-composite coating.....	105
59.	XPS analysis of UV irradiation for refined cerium dioxide nano-composite coating, (a) survey scan before UV irradiation, (b) C 1s spectra and (c) O 1s spectra.....	106

LIST OF ABBREVIATIONS

CAH	Contact angle hysteresis
CeO ₂	Cerium dioxide
CVD	Chemical vapor deposition
DFT	Density functional theory
DI	Deionized
FSM	Fluorinated silane molecules
HCL	Hydrochloric
HMT	Hexamethylenetetramine
NaOH	Sodium hydroxide
OTS	Octadecyltrichlorosilane
PA 6.6	Polyamide 6.6
PDMS	Polydimethylsiloxane
PE	Polyethylene
PF ₃	Tetrahydroperfluorodecyltrichlorosilane
PLD	Pulsed laser deposition
PMMA	Polymethyl methacrylate
PP	Polypropylene
PS	Polystyrene
PSi	Polysiloxane
PTFE	Poly-tetrafluoroethylene
PVD	Physical vapor deposition
PVDF	Polyvinylidene fluoride

REO	Rare-earth oxide
SEM	Scan electron microscope
SiC	Silicon carbide
STA	Stearic Acid
TEM	Transmission electron microscope
TiO ₂	Titanium dioxide
UV	Ultra-violet
XPS	X-ray photoelectron spectroscopy
XRD	X-ray diffraction

Summary

Superhydrophobic surfaces have received a lot of attention because water repellent materials have many good properties, such as self-cleaning, anti-icing, anti-bacterial, drag reduction and good thermal transfer. Superhydrophobic surfaces may be applied to air-crafts, used as exterior coatings for buildings, automobiles, hospital equipment, wind turbines, etc. However, superhydrophobic surfaces have limited usage in high wear conditions due to their poor mechanical durability. Therefore, a water repellent material with good durability, good thermal stability and good chemical stability is a requirement for more widespread use of these remarkable materials.

In this study, the wetting behavior of cerium dioxide will be studied. Cerium dioxide belongs to the group of rare earth oxides. Cerium dioxide has been studied widely because of its attractive properties such as high hardness, high thermal stability, high wear resistance, high chemical stability and good transparency. There are three main subjects that will be discussed in this dissertation. First, the intrinsic wetting behavior of cerium dioxide will be investigated. Second we will investigate methods for the development of robust, water repellent coatings. Third, the development of scalable techniques for coating of large structures will be presented.

Cerium dioxide thin films were fabricated by pulsed laser deposition method. The effect of the oxygen pressure, substrate temperature, UV irradiation treatment and annealing treatment were investigated to understand the hydrophobicity of cerium dioxide. In addition, cerium dioxide nano-particles were synthesized by a hydrothermal method. Nano-flake structures create the

surface texture that can result in superhydrophobicity after chemical modification to lower the surface energy. A novel superhydrophobic cerium dioxide nano-composite coating was developed using polyurethane and cerium dioxide nano-particles. Boiling tests, immersion in various acidic and basic solutions, peel tests and mechanical abrasion tests were performed to understand the long-term durability and stability of the superhydrophobic cerium dioxide nano-composite coating.

Finally, the x-ray photoelectron spectroscopy results show that the oxide materials that we studied are intrinsically hydrophilic, but may become hydrophobic when the surface adsorbs hydrocarbon species in the ambient environment. However, cerium dioxide nano-particles can be used to fabricate superhydrophobic surfaces. The durability of the cerium dioxide composite coating can be improved by etching the aluminum alloy surface. Our novel cerium dioxide polymer composite coating has superior thermal stability, chemical stability and good adhesion.

Chapter I: Introduction

I. A. Motivation for this Research

Superhydrophobic surfaces have received a lot of attention because they tend to have good corrosion resistance, low hydrodynamic friction, anti-bacterial, anti-icing and water repellency. Superhydrophobic surfaces can be fabricated by sol-gel methods¹², chemical vapor deposition¹³, electrospinning¹⁴, lithographic methods¹⁵, laser ablation¹⁶, phase separation¹⁷, plasma etching¹⁸, electrochemical deposition¹⁹ and template lamination methods²⁰. There is a critical need to develop water-repellant surfaces with good wear resistance, high thermal stability and good chemical stability. The industrial applications for superhydrophobic surfaces have been limited due to poor durability of state-of-the-art materials.

I. B. Introduction to Research

Ceria has been widely used in three way catalytic converters⁹, fuel cells¹⁰ and corrosion protection¹¹ because ceria has high capability to release and store oxygen. The realization of hydrophobic ceria thin film coatings may extend their use to the aircraft industry, kitchen equipment, smart glass and biomedical equipment. For this reason, we are interested in understanding the wetting behavior of cerium dioxide (CeO_2). This study details our investigation of the effect of oxygen partial pressure and substrate deposition temperature during pulsed laser deposition, annealing treatment and ultraviolet irradiation treatment. The fabrication of cerium dioxide superhydrophobic surface is discussed. The durability and stability of the cerium dioxide

superhydrophobic coating is tested after boiling various mechanical impact and immersion in acidic and basic solutions.

I.C. Organization of Document

Chapter 2 provides an overview of the various properties used to characterize the wetting properties of materials, the types of contact angles, types of wetting and the hydrophobicity of the various classes of materials. The chapter also covers the wetting properties of rare earth oxides, the properties of ceria and the tunable wetting behavior of oxide materials.

Chapter 3 details the materials, methods and devices used for the research study including the methods for film deposition, water contact angle measurement, UV irradiation treatment and annealing treatment. In addition, the assignment of the XPS spectrum peak fits will be demonstrated.

Chapter 4 shows results for my study of the effects of oxygen partial pressure and substrate temperature, the effect of UV irradiation treatment in air and vacuum and the effect of the annealing treatment in air and vacuum on the wetting behavior of ceria films.

Chapter 5 shows the wetting behavior for two mixed oxide thin films, cerium dioxide and titanium oxide. The UV irradiation resistance was also studied for the titanium doped cerium thin films.

Chapter 6 is a study of the superhydrophobicity of cerium dioxide nano-structures. Flower-like nano-structures were fabricated by hydrothermal method. The coating was then modified by the stearic acid to achieve very high water repellency.

Chapter 7 is a study of the chemical and thermal stability of the improved superhydrophobic cerium dioxide nano-composite on aluminum alloy substrates. Boiling tests, immersion in acidic and basic solutions was performed to determine the stability of the novel cerium dioxide nano-composite superhydrophobic coating.

Chapter 8 is a study of the mechanical durability on the cerium dioxide nano-composite coating. The durability of the coating is improved by etching the aluminum alloy. Peel tests and mechanical abrasion tests were performed to determine the durability of the cerium dioxide nano-composite coating.

Chapter 9 is a summary and conclusion for the thesis. Suggestions for future work are also included in this chapter.

Chapter II: Literature Review

II. A. Wetting Behavior and Contact Angle

The wetting behavior of a surface can be classified by measuring the water contact angle.

The water contact angle depends on the surface energy, surface roughness^{21, 22, 23}, pressure, temperature, humidity and surface contamination. Different kinds of contact angle measurements are used to determine the wetting properties of surfaces, like the static contact angle, advancing angle, receding angle and roll-off-angle. In addition, the water droplet bouncing experiment can be used to determine the dynamic wetting effects and the adhesion properties of water-repellant surfaces.

II.A.1. Static Contact Angle

Static contact angles as shown in figure 1a are obtained for stationary droplets measured at the interface between liquid and solid. Static contact angles are usually used in quality control, fundamental research and product development²⁸. For example, the advancements in automotive windshield technology are based partially on understanding how rain droplets behave on the glass surface. The wetting behavior as determined by water contact angle measurements can change the performance of the part and appearance and performance of the automobile. The static contact angle is usually used to define the wetting behavior of a surface. Superhydrophilic surfaces usually have contact angles less than 10°. Hydrophilic surfaces have contact angles between 11° and 89°. Hydrophobic or water repellent surfaces are normally considered to have contact angles between 90° and 149°, contact angles greater than 150° are used to describe superhydrophobic surfaces.

II.A.2. Contact Angle Hysteresis (CAH)

Contact angle hysteresis is the difference between the advancing contact angle and receding contact angle as shown in figure 1b. The contact angle at the front of the droplet is called advancing (maximal) contact angle; the contact angle at the back of the droplet is called receding (minimal) contact angle. Surfaces with high adhesion normally have high contact angle hysteresis. Therefore, superhydrophobic surfaces should have very small contact angle hysteresis, so the droplets can roll-off easily.

II.A.3. Roll-Off-Angle

The roll-off angle shown in figure 1c is also called the sliding angle or tilt angle. It is defined as the angle between the sample surface and horizontal plane when the liquid droplet starts to slide off of the surface. The roll-off angle can be measure by tilting the surface with respect to the horizontal surface. Superhydrophobic surfaces usually have roll-off angles less than 10°.

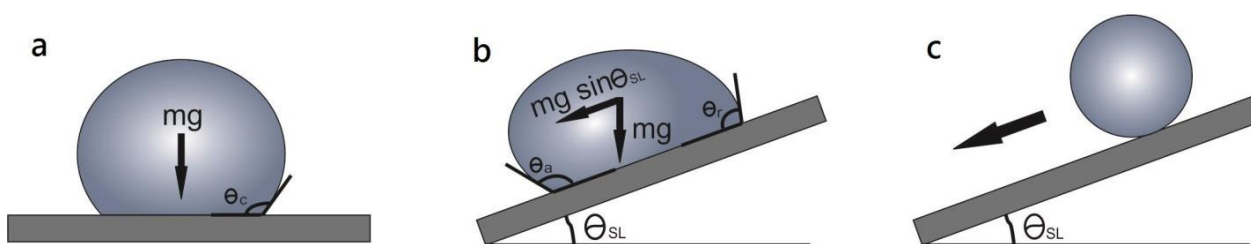


Figure 1. Schematic depiction of (a) static contact angle, (b) contact angle hysteresis and (c) roll off angle.

II.B. Wenzel State and Cassie-Baxter State

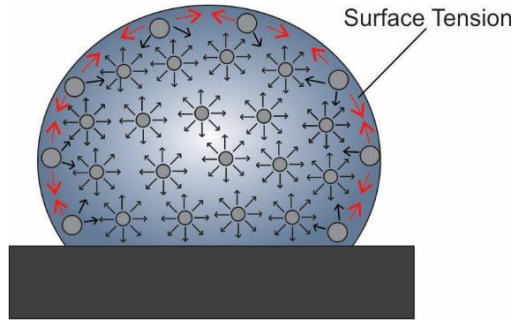


Figure 2. Schematic depiction of surface tension

The surface tension and gravity play an important role in determining the droplet's shape²¹. Figure 2 shows how the distribution of the cohesive forces between each water molecule inside of the materials and at the surface. Surface tension forms when an interface is formed, such as liquid-air, liquid-solid and solid-air. For example, the atoms of water at the surface do not tend to bond with other atoms in air, so atoms tend to bond with the neighboring atoms inside of the water droplet. The contact angle is an equilibrium condition between solid-air-liquid state. Therefore, the surface energy can be determined by the Dupre equation, Eq (1).

$$(1)$$

is the work of adhesion per unit area
 is the surface tension between solid and vapor
 is the surface tension between solid and liquid
 is the surface tension between liquid and vapor

The water contact angle is formed by a three-phase boundary, liquid, surrounded vapor and solid surface. In the situation of chemically heterogeneous substrate, the contact angle equation is based on the dipole moments at the molecular level. At equilibrium,

the characteristic angle between three phases is called static contact angle. The static contact angle can be determined by net surface energy equation ²⁸.

(2)

is the total energy in the system
 is the surface area between solid and vapor
 is the surface area between solid and liquid
 is the surface area between liquid and vapor

Assuming the volume does not change, $\frac{dV}{dt} = 0$ and $\frac{dE}{dt} = 0$. The relationship between the various components of the surface tension is given in the equation Eq.3 below:

———— (3)

is the contact angle on the flat solid

There are three different concepts used to describe the wetting behavior on the dry solid surface: solid state, Wenzel state and Cassie-Baxter state²⁵. Figure 3a-c shows the schematic depictions of wetting behavior for solid state, Wenzel state and Cassie-Baxter state, respectively. For the solid state, the water droplets sit on the solid surface and are surrounded by vapor. For Wenzel state, the water droplets penetrate into the surface structure at the rough surface. For the Cassie-Baxter state, the water droplets sit on the surface structure at the rough surface. The type of the wetting can be predicted by the Cassie and Wenzel equations.

The Cassie and Wenzel equations are used to theoretically predict the contact angle of the droplet on the rough surface, which combines with the chemical heterogeneity. In the Cassie-Baxter state in figure 3b, the water droplet partially sits on air leading to a contact angle that ranges between 120 and 180°. The contact area between liquid and solid surfaces in the Cassie-Baxter state is less than the droplet in the Wenzel state. Therefore, the adhesion force decreases as the contact area is decreased. The contact angle in the Cassie-Baxter effect is based on the interfacial surface free energy per unit area between the liquid and the vapor and the solid. Then, the surface energy on the flat surface of γ_{lv} can be modified to $\gamma_{lv}f_{lv}$ for the liquid-air interfaces on the rough surface. The Cassie-Baxter equation Eq.4 can be defined as:

$$(4)$$

f_{lv} is the area fraction of the solid contact with the liquid

θ is the contact angle on the flat solid

θ_r is the contact angle on the micro-structures surface

In the Wenzel state in figure 3c, the water molecules penetrate into the surface asperities of the rough surface, which can increase the water contact area on the surface. The surface adhesion increases as the contact area increases at the liquid and solid interface. The roughness factor r is induced by the Wenzel equation, which is the ratio of the total actual contact area in the liquid-solid interface on the rough surface to the planar projected area of the rough solid surface. Then the surface free energy can be changed to $\gamma_{lv}r$ on the rough surface in the Wenzel effect. Meanwhile, the surface adhesion force increases because the contact area increases due to the roughness represented by surface asperities. The Wenzel equation predicts that the contact angle decreases when roughness increases on

the hydrophilic surface. In contrast, it predicts that the contact angle increases when roughness increases on the hydrophobic surface. Therefore, the surface roughness controls the wetting behavior of the surface in Wenzel state. The Wenzel equation Eq.5 can be defined as:

$$(5)$$

is the surface roughness factor and $r > 1$

is the contact angle on the solid

is the contact angle on the micro-structures surface

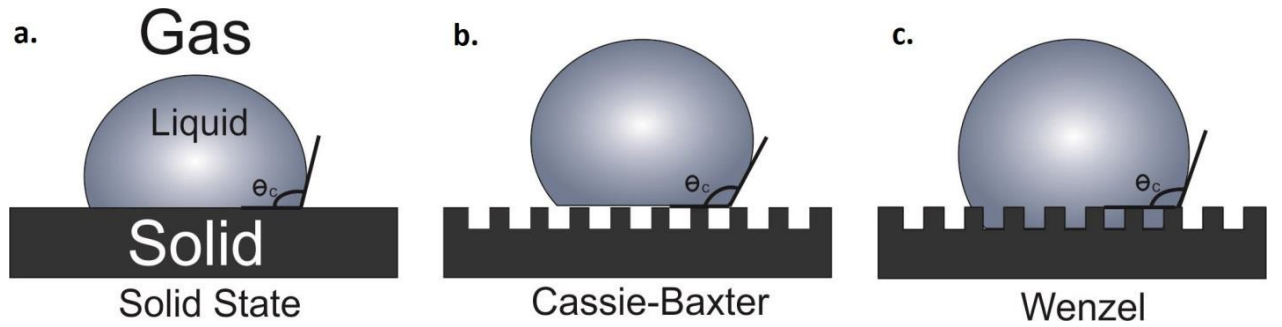


Figure 3. Schematic depiction of various types of wetting (a) solid-liquid state, (b) Cassie-Baxter state and (c) Wenzel state.

II. B. 1. The Challenges of Wenzel model

Some researchers suggested that the Wenzel equation is sufficient to predict the contact angle on micro-scale rough surfaces, but it fails when the droplets are placed on nano-scale rough surfaces^{63, 64}. The van der Waals bonds in the materials can attract the water molecules to form a thin mono-layer which cause the Wenzel model to fail. Errington *et al.* and co-workers have constructed a molecular simulation model based on the Wenzel equation, they found out the Wenzel's predictions failed when the surface roughness is smaller to 20 molecular diameters^{63, 65}. Leroy *et al.* tested the water wetting behavior on

a rough model graphite surface with superficial defects and they found that the wetting behavior is controlled by the contour length of the defect pattern. He suggested the corner effect is one reason for the failure of Wenzel's equation to predict the contact angle on the nano-scale structure⁶⁶. The corner effect is when the surface free energy is concentrated at the corner on the structure wall. In addition, Acharya *et al.* and Leroy *et al.* suggested that the vertical wall and horizontal wall have different surface free energy which affects the interaction of the water molecules. They created the surface roughness by controlling the length of the carbon chain with $-\text{CF}_3$ headgroup. Figure 4 shows the schematic of the vertical surface that would be dominated by the amphiphile's tail while the horizontal surface would be dominated by amphiphile's headgroup^{66, 67}. Therefore, the prediction of the wetting behavior on nano-scale rough surfaces needs to be studied more.

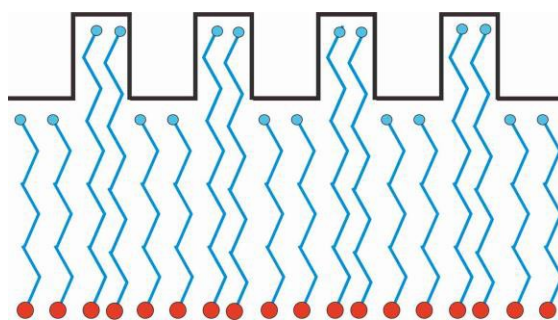


Figure 4 Schematic depictions of the amphiphile's head and amphiphile's tail effect on the vertical surface and horizontal surface. (Hari Acharya; Nicholas J. Mozdierz; Pawel Keblinski; Shekhar Garde, *How Chemistry, Nanoscale Roughness, and the Direction of Heat Flow Affect Thermal Conductance of Solid-Water Interfaces*, *Ind. Eng. Chem. Res.*, 2012, Vol. 51, 1767-1773.)

II. B. 2. Temperature, Pressure, Humidity Influences and Vibration

Surface tension depends on the temperature. The water surface tension at 20 is 72.75 mN/m. The water surface tension decreases as the temperature increases²⁴. According to the Eötvös rule, the surface tension of an arbitrary pure liquid can be predicted at all temperatures. The density, molar mass and the critical temperature of the liquid substance must be known⁵⁹ from the Eq.6:

(6)

V is the molar volume
 T_c is the critical temperature of a liquid
 σ is the surface tension

—

M is molar mass
 ρ is the density

Therefore, the surface tension of water between 273 K and 373 K can be expressed in Eq. 7:

—

(7)

The water contact angle also depends on the pressure. The water drops can be switched between Cassie-Baxter and Wenzel states on superhydrophobic surfaces when pressure is applied. It has been reported that pressing on the drops may change the contact angle^{25, 26}. This effect is caused by the impalement of the drop due to surface roughness. For example, the contact angle decreases with the larger droplets because the pressure is increased due to gravity and the water penetrates between two surface asperities.

The humidity of the environment also influences the accuracy of the water contact angle measurement. Quere *et al.* have studied the condensing water vapor effect on superhydrophobic surfaces²⁵. When the water vapor condenses on the superhydrophobic surface, the water contact angle of the condensed water is lower than the case of just depositing the droplets on the same surface. This implies that the wetting of the condensing water vapor on the surface is in the Wenzel state.

Jung *et al.* and Bhushan *et al.* proved that the vibration of the droplet on the surface can influence the transition of Cassie state to Wenzel state. They observed the effect of the resonance frequency of the droplet and the vibration amplitude. Celestini *et al.* and Kofman *et al.* shows that the resonance frequency depends on the contact angle of the structured surface⁷⁰. Bhushan *et al.* found that the contact angle decreases after the vibration with 2.4 mm and 2.0 mm amplitude for the 0.12 g/mm² nanostructure with n-hexatriacontane and microstructure, respectively. For the other three samples, 0.2 g/mm² nanostructure with n-hexatriacontane, 0.4 g/mm² nanostructure with n-hexatriacontane and hierarchical structure, they observed that the vibrating droplets bounced off before the solid-air-liquid interface got damaged⁷¹. Therefore, the vibration of the droplets can reduce the static contact angle because the vibration perturbs the solid-air-liquid interface.

II. B. 3. Contact angle measurement challenges and errors

Measuring the contact angle is very important to determine the true wetting behavior on solid surfaces. However, there are many different factors that can affect the accuracy of

the contact angle measurement. Nosonovsky and Bhushan reported that the liquid-air interface comes in contact with the solid surface at the micro and nano-scale may be different ²⁷. Based on the Wenzel and Cassie equation, the contact angle is based on a macro-scale parameter. The contact angle also depends upon the pressure balance between two surfaces at the solid water interface. In general, a thin wetting film is formed between the solid surface and liquid phase inside of the droplet because water molecules tend to form a thin layer due to a long distance Van der Waals adhesion forces ²⁸. Bash and Sharma reported that the thickness of the stable wetting films plays an important role on the contact angle ²⁹. In this case, the curvature of the droplet is changed near the triple line from the spherical surface into the thin wetting film. Thus, the nano-scale contact angle is much smaller than the apparent contact angle.

The other factors that will affect the accuracy of the contact angle measurement is the surface defects. Even though smooth hydrophobic surfaces are readily available, there are still usually some hydrophilic spots on the surface. The water molecules tend to bond at the hydrophilic spots first, which results in low contact angle. Therefore, the hydrophilic spots affect the accuracy of the contact angle measurement ²⁸.

In addition, the definition of the static contact angle is unclear. Static contact angle is known as the contact angle that is measured when the droplet is not moving on the surface. However, in reality the contact angle changes with time. After deposition of the droplet on the surface, the water evaporates, causing the volume of the liquid to decrease. It is very difficult to avoid this dynamic effect.

Even though there are many challenges to measuring the contact angles accurately, accuracy can be increased by several methods. At least 10 contact angle measurements were taken on different spots of the surface to reduce the contact angle measurement error. In addition, the humidity should be controlled because it can affect the water evaporate rate. The droplets should be placed on the surface gently because the impact pressure can be affected the shape of the droplets.

II. B. 4. Dynamic Wetting of Surfaces: Water Droplets Bouncing on Surfaces

The subject of water droplets bouncing on dry surfaces is intriguing for mathematicians, physicists and engineers. Bouncing effects on dry surfaces depend on the surface roughness, impact velocity, surface adhesion, surface temperature and surface chemistry. *Yarin et al.* have observed the bouncing behavior on the dry surface and characterized the various wetting responses. He found that there are six different morphologies of drop impact on a dry surface: deposition, prompt splash, corona splash, receding break-up, partial rebound and complete rebound ⁷². Figure 5a is called deposition, a scenario in which the droplet spreads over the surface at the end of the spreading stage and stays there. Figure 5b is called prompt splash scenario. The prompt splash occurs when the droplet impact velocity increases on the rough surface. As a result, the droplet splashes and becomes a liquid lamella from a spreading droplet. Figure 5c is called corona splash, in which the surface tension is reduced and the droplet is detached from the thin lamella wall to form a crown. Figure 5d is called receding break-up, which occurs when the droplet recedes after the spreading stage. The receding velocity is sufficiently high and it

breaks up into a number of parts. Figure 5e is called partial rebound scenario in which the droplet can partly launch one or more droplets at the top of lamella. There is remaining kinetic energy after the receding stage. The sufficiently high kinetic energy can squeeze the liquid upward from the surface due to the capillary wave. Figure 5f shows a complete rebound in which the droplet bounces off of the surface after impact.

Even though the experimental data was able to uncover the relationship between roughness and wettability for water droplet impact on dry surfaces, the fundamental mechanisms are still not clear. For example, the transition from spreading to the receding stage is not well understood. In addition, the effect of surface temperature and the droplet viscosity in droplet impact on a dry surface is still incompletely understood. It is important to study the droplet impact on a cold dry surface because it can determine the anti-icing ability on superhydrophobic surfaces.

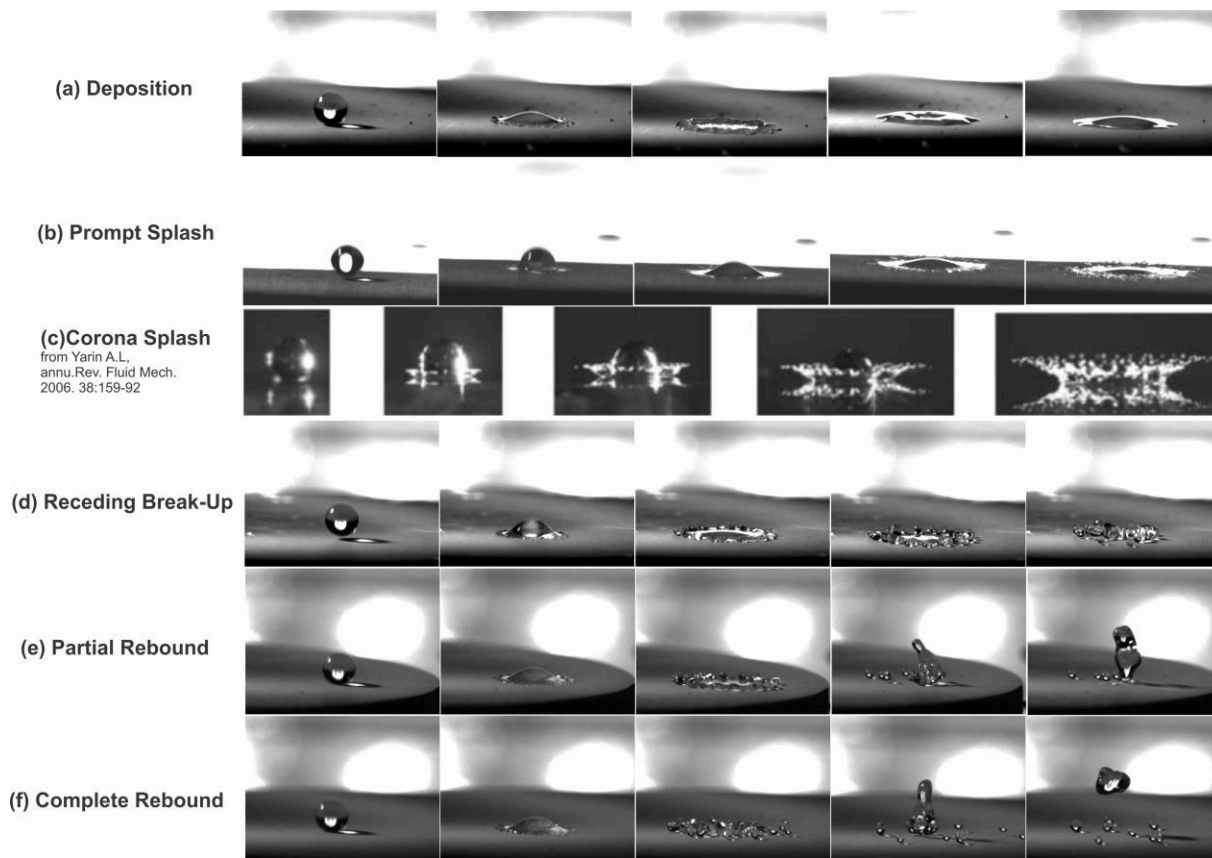


Figure 5. Morphology of drop impact on dry surface: (a) deposition, (b) prompt splash, (c) corona splash, (d) receding break-up, (e) partial rebound and (f) complete rebound.

II. C. Hydrophobicity in Metals, Polymers, Oxides and Rare Earth Oxides

Metal:

Metals are hydrophilic materials. Metals have a very high tendency to share the outer-shell electron with all atoms to form a sea of free electrons. The free electrons are the source of the attractive forces that hold the atoms together forming the solid-state. The result is that metals have polar surfaces that attract the water molecules, forming hydrophilic surfaces.

Polymers:

Polymers can be hydrophilic or hydrophobic. For example, polyamide 6.6 (PA 6.6), polyethylene (PE), polystyrene (PS) and polypropylene (PP) have water contact angles of 64 , 85 , 91 and 99 respectively ⁴⁸. The long-chain structure of the polymer can affect the water contact angle. Polymers have been widely used in the industrial application for several decades. However, the applications are often limited to use due to the unstable surface properties, such as wetting behavior, low thermal stability ⁷³.

Ceramics:

Ceramics are intrinsically hydrophilic because the ionic bonding generates a charge between the attracted metal atoms and non-metal atoms, which is based on the electronegativity of the atoms. A recent report suggests that electronegativity is a main factor in determining the wettability of oxide materials. The electronegativity in oxide materials controls the surface polarity, the adsorbed hydroxide species and the adsorbed hydrocarbon ³¹. In addition, oxide materials have traditionally been categorized as hydrophilic because the oxygen atoms easily react with the water molecules to form hydrogen bonds.

II. D. The Properties of Ceria and applications

Cerium dioxide (CeO₂) belongs to the group of rare-earth oxides. Ceria has been studied widely because of its attractive properties such as, high hardness ³², high thermal stability ³³, high wear resistance ³⁴, high chemical stability ³⁵, high transparency ³⁶, high refractive index³⁷ and wide band gap of ~4.1-6 eV ^{44, 45, 46}. Ceria has also been always used in solid oxide fuel cells and three-ways catalysis because of the very high ability to

release and storage oxygen. In addition, ceria thin films are deposited on steel as corrosion protective layer. However, there are very few studies on the wetting properties of ceria. It is very important to understand the wetting behavior of ceria to apply in many engineering applications.

II. D. 1. Oxygen Vacancies and other Ceria Surface Defects

Oxygen vacancies create very reactive defect sites on the oxide surface. The surface oxygen vacancies involve many applications such as, three-way catalytic ⁶⁰, self-cleaning glass ⁶¹ and fuel cells ⁶². CeO₂ is the main material in modern automotive exhaust treatment catalysis because it can form oxygen vacancies rapidly. The oxygen vacancy sites provide a capacity to store and release oxygen in different environment.

Both Ce₂O₃ and CeO₂ can be formed by exposure of cerium to high hydrogen (clarify this) or oxygen partial pressure^{40, 41}. The oxidation states of Ce³⁺ and Ce⁴⁺ can be observed by x-ray photoelectron spectroscopy (XPS) due to the charge transfer from O 2*p* (initial state) to the Ce 4*f* (final state) orbitals³⁹.

Esch et al. has reported the structure model of oxygen vacancies on ceria substrates to understanding the reduction processes in detail ³⁸. Their density functional theory (DFT) calculations showed that the surface O atoms surrounding the vacancy relax outward from the closest Ce ions. A positive electrostatic field centered on the vacancy that repels the nearest neighbor Ce cations so that electron localization occurs on the Ce ions in the defect sites. In consequence, Ce³⁺ ions, which are larger than Ce⁴⁺ ions, push the neighboring O atoms farther away.

There are many studies that suggest that oxygen defects can affect the wetting behavior of oxide surfaces^{42, 43}. The defect sites are known to be very reactive and easily bond with water, which results in hydrophilic surfaces. For example, nanostructured TiO₂ has been shown to generate oxygen defects during ultraviolet irradiation, which are responsible for switching of its wetting properties from hydrophobic to hydrophilic. In addition, cerium has been studied for fuel cell applications because of its capability of dissociating water and the very high mobility of the oxygen vacancy in its lattice⁸⁹. However, the effect of the hydrophobicity on the smooth ceria thin films against the oxygen vacancy is still unknown.

II. D. 2. The bandgap of Ceria

There has been considerable debate regarding the bandgap of the ceria. Many research groups have measured the bandgap of ceria and the values were between 4.1 eV to 7.2 eV. *G. Dutta et al.* reported that CeO₂ layers epitaxially grown on (100) silicon substrates by electron-beam evaporation had a bandgap of ~4.1 eV. The reduced CeO_{1.75} layers had a bandgap of ~0.3 eV⁴⁴. D.R. Mullins et al. have grown CeO₂ thin films by laser ablation on single crystal SrTiO₃ substrate resulting in a bandgap of 6 eV⁴⁵. A. Pfau deposited CeO₂ thin films on Pt foils by electron beam evaporation and measured a bandgap of 5.6 eV⁴⁶. *R. Gillen et al.* has calculated the CeO₂ bandgap by using different methods such as, hybrid density functionals HSE03, HSE06 and screened-exchange (sX-LDA). The calculating results showed that the CeO₂ bandgap was between 6.5 eV to 7.2 eV. In fact, the CeO₂ bandgap is dependent upon the crystallization, lattice size,

oxygen vacancy, different fabrication methods, the film composition, temperature and stress.

II. E. Photocatalytic Activity and Reversible Wetting Behavior

Figure 6 is a schematic depiction of the mechanisms governing the photocatalytic activity of TiO_2 . Photocatalytic activity is a catalytic type of reaction that starts from generating electron-hole pairs due to UV irradiation at the material surface. When the UV irradiation energy is larger than the bandgap of the semi-conducting materials, the electrons are excited from the valence band and transferred to the conduction band, generating holes in the valence band. The holes capture electrons from moisture in air and form hydroxyl radicals. The electrons that are excited to the conduction band react with oxygen in the atmosphere to form superoxide anions. The superoxide anions and hydroxyl radicals decompose organic molecules close to the surface, producing carbon dioxide and water.

The hydrophobicity and the photocatalytic activity of nanostructured TiO_2 materials has been studied widely because it may be used as a self-cleaning glass due to its high transparency and good sensitivity to incoming radiation. Similarly, CeO_2 has a lot of attractive properties such as high transparency, good wear resistance, good chemical stability, good thermal stability and high hardness. However, there are very few studies on the photocatalytic activity of CeO_2 thin films. It is important to understand the effect of oxygen vacancies on the photocatalytic activity and the tunable wetting behavior.

The reversible wetting behavior has also received a lot of attention. *M. Stepien et al.* has successfully fabricated reversible superhydrophobic TiO_2 thin films by liquid flame spray technique⁴². The water contact angle switched from 160 degrees to 27 degrees after UV irradiation treatment. The water contact angle recovered its original value after placing the samples in an oven for 3 minutes at 150 °C. *H. Liu et al.* have reported the reversible wetting between superhydrophobicity and superhydrophilicity of ZnO films⁴⁷. There are three main mechanisms that have been used to explain the reversible wetting behavior. The first is similar to the aforementioned mechanism for TiO_2 where UV irradiation generates holes creating oxygen vacancies. The oxygen vacancies easily adsorb water, which results in hydrophilicity. Second, the electrons generate hydroxyl groups on the surface. The hydroxyl groups are very reactive, attracting water molecules, which also results in hydrophilicity. Third, the photocatalytic decomposition of organic contaminants like hydrocarbons at the oxide surface can result in hydrophilicity. To recover the contact angle, oxygen will replace the oxygen vacancies and the hydroxyl groups for mechanisms following the first case and second case. Alternatively, the water contact angle can be recovered by formation of new contaminant layers for the third case. Therefore, the question, can ceria thin films display reversible wetting behavior naturally arises? If yes, the question what is the mechanism for this behavior should be answered.

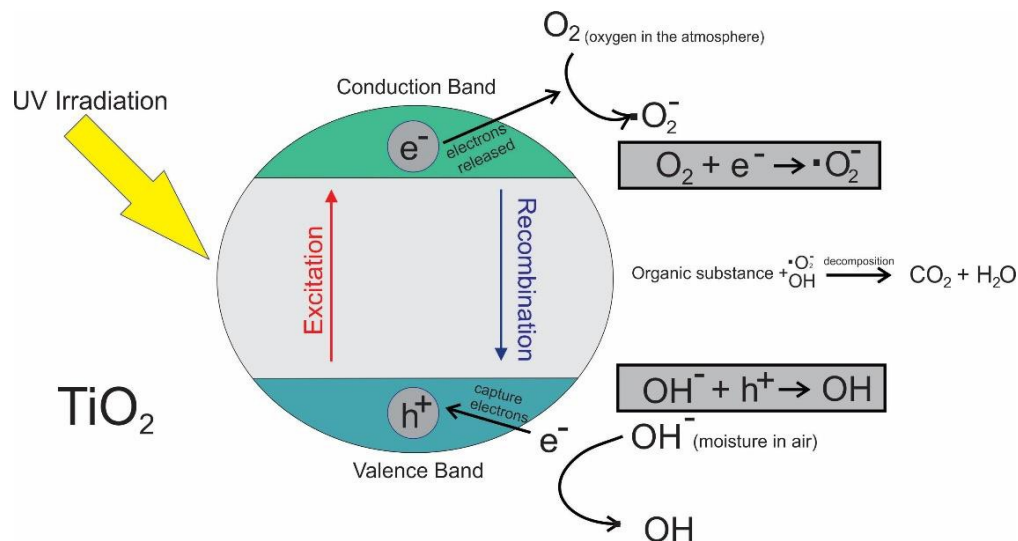


Figure 6. Schematic depiction of photocatalytic activity on TiO_2

II. F. Annealing treatment on Ceria

There are reports that suggest annealing in air or H_2 can cause the reduction processes on the ceria surface resulting in oxygen vacancies^{38, 46}. It is known that ceria has high thermal stability and chemical stability. However, the effect of annealing processes and the role of the oxygen vacancies on the wetting behavior are unknown.

II. G. Applications for Superhydrophobic Surfaces

Superhydrophobic surfaces have been studied widely in past decades. Superhydrophobic surfaces have extreme high water repellency making the surface difficult to wet. Superhydrophobic coatings have several important properties, such as self-cleaning, anit-bacterial, anti-icing and high heat transfer capability. Superhydrophobic coatings can be used in many applications.

II. G. 1. Self-Cleaning

Bhushan et al. tested the self-cleaning efficiency of superhydrophobic surfaces by measuring the number of silicon carbide (SiC) particles on the surface after 2 minutes of cleaning with water⁷⁴. The water droplets were deposited on the surface with nearly zero impact velocity and the volume of the water used was about 10 mL. The surface was tilted slight larger than the roll-off angle, so that the droplets would be mobile on the contaminated surface. After the 2 minutes of water cleaning, hierarchical structures were found to have fewer remaining particles (20%-30% remaining) on the surface, meanwhile the flat waxy epoxy resin had 50%-80% of the particles remaining on the surface. The droplets easily roll off of the contaminated hierarchical surface. However, the droplets first adhered to the epoxy resin and then rolled off after the volume of the droplet increased. This result shows that water droplets can collect the dust particles as they roll off of the surface resulting in the high self-cleaning efficiency for superhydrophobic surfaces. Even though superhydrophobic surfaces have good self-cleaning properties, the droplets cannot collect the dust trapped in the cavities of the microstructures, causing some dust particles to remain on the surface. Therefore, superhydrophobic surfaces can be used on the self-cleaning glass, automobile body and exterior painting for building and solar panels.

II. G. 2. Heat Transfer

Vakarelski et al. showed that superhydrophobic surfaces can produce conditions sufficient for boiling of water without bubbles⁷⁵. A superhydrophobic coating was

fabricated on the surface of a metal ball. The superhydrophobic, coated metal ball was heated to 400 and then cooled down to room temperature. They observed that the superhydrophobic, coated metal ball did not have air bubbles on the surface and there was no explosive boiling during the cooling processes. In contrast, for the hydrophilic metal, a layer of water vapor was formed at the surface leading to explosive bubbling. *Vakarelski et al.* suggested that this phenomenon occurred due to the Leidenfrost effect. In this case, the water may be boiled without bubbling if the vapor cushion is broken down on the surface. Without a doubt, the superhydrophobic surfaces can be used to increase the heat transfer rate because it can reduce the bubble layer on the hot surface. The bubble layer is a heat isolation substance that reduces the heat transfer rate. Therefore, superhydrophobic surfaces may be applied to automobile engines or used power plants for cooling applications.

II. G. 3. Anti-Bacterial

Anti-bacterial materials have been studied for some time. Bacteria are killed by metallic ions like Ag^+ and highly reactive species like hydroxyl radicals, hydrogen peroxide and superoxide. However, overuse of anti-bacterial medications may increase the bacterial resistance, which makes treatment by medication difficult and harmful to human health. A new strategy was developed involving the use of superhydrophobic surfaces. Superhydrophobic surface do not kill bacteria at the surface. Bacteria are removed because of their low, adhesion on superhydrophobic surfaces. Superhydrophobic surfaces may easily remove the bacteria before a thick biofilm is

fully formed at the surface⁷⁶. *Tang et al.* studied the adhesion of staphylococcus aureus on different surfaces: a hydrophilic surface (contact angle ~54 degrees), a hydrophobic surface (~133 degrees) and a superhydrophobic surface (contact angle ~156 degrees)⁷⁷. The results suggest that the amount of the bacteria on the surface decreases when the water contact angle increases. The superhydrophobic surface had the smallest amount of bacteria on the surface after 4 hours of adhesion. Therefore, superhydrophobic surfaces can efficiently reduce the bacteria on the surface. Superhydrophobic surfaces may be applied on the ceilings and walls of hospital buildings among other places to reduce bacteria adhesion.

II. G. 4. Anti-icing

Some reports suggest that superhydrophobic surfaces provide anti-icing capability because the surface roughness can reduce the contact area between the impact droplet and the cold surface. The basic concept involves reduction of the impact droplet contact time on the cold surface⁷⁸. There is a correlation to the droplet diameter and the contact time. *Quere et al.* proves that the contact time depends on the droplet radius and surface tension^{79, 80}. Increases in the contact time are related to droplet spreading across less water repellant surfaces. *Alzenberg et al.* observed the critical droplet temperature via the surface contact time. They found that the 15 L of water droplet will bounce off water repellant surfaces if the surface temperature is above the critical transition temperature between -20 to -25 . If the droplet contact time is larger than critical transition time, the droplets will freeze⁸¹. The critical contact time is shown below:

$$\left(\frac{\rho}{\rho_0} \right) \quad (8)$$

ρ is the density of the liquid.

σ is the surface tension.

R is the initial radius of impact droplets.

In reality, superhydrophobic surfaces may be “hydrophobic”, but not “icephobic”. Physisorbed water in the material can be condensed when the surface temperature is sufficiently low. A thin liquid mono-layer can form between surface asperities, increasing the wettability. Usually, frost will be formed on the surface due to the humidity and the surface impurity, such as dust. Even though the surface is superhydrophobic, ice formation starts at defect sites and continuous until sheets of ice are formed via ice bridging. Eventually, the superhydrophobic surface loses the anti-icing property due to frost formation. The other challenges for the anti-icing on the superhydrophobic surface are the durability. The surface roughness and surface energy are the main factor that determine whether surfaces will be superhydrophobic. The stress due to ice formation at the surface can damage the surface structure, which degrades the anti-icing ability after several icing cycles. Therefore, the development of the anti-icing on superhydrophobic surface still needs to be studied. The superhydrophobic surface may be able to apply to air-craft, power transmission lines and radar or telecommunication antennas.

II. H. Fabrication Methods of Superhydrophobic Surface

Surface roughness and surface energy are the main factors that can be varied to form a superhydrophobic surface. There are two basic methods for fabricating the superhydrophobic surface. One involves creating micro/nano structure on low surface energy substrates. The second involves chemical modification of the micro/nano structured surface. Several different fabrication methods have been developed for superhydrophobic surfaces. Sol-gel methods¹², chemical vapor deposition¹³, electrospinning¹⁴, lithographic methods¹⁵, laser ablation¹⁶, phase separation¹⁷, plasma etching¹⁸, electrochemical deposition¹⁹ and template lamination methods²⁰ have all been used. The general fabrication techniques for forming superhydrophobic surface are given in figure 7.

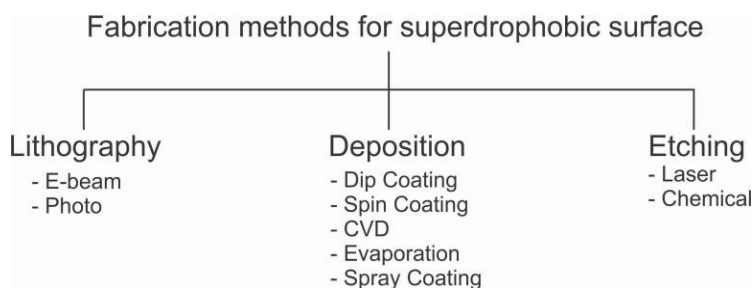


Figure 7. General fabrication techniques for forming superhydrophobic surfaces

II. H. 1. Lithography

Lithography provides is a high precision method for creating the micro/nano structures over large areas. However, this technique requires a high cost equipment and the fabrication time is long. Bhushan and Jung fabricated Si microstructures by photolithography⁸². The sample was then modified by depositing 1,1,2,2,-tetrahydroperfluorodecyltrichlorosilane (PF₃) using a vapor phase deposition technique

to achieve superhydrophobicity with 170 degree contact angle. *Martines et al.* fabricated nano-pits and nano-pillars by using electron beam lithography. The nano-structure was then coated by octadecyltrichlorosilane (OTS) to increase the superhydrophobicity (164 degree contact angle⁸³).

II. H. 2. Deposition

Deposition methods can also be used to make a superhydrophobic surface. These methods are flexible, capable of processing a variety of materials and are low cost. However, the size and the pitch of the micro-structure are limited by the nano-particles synthesis processes. *Klein et al.* fabricated a superhydrophobic surface by dip coating method with slurry containing nano-silica spheres⁸⁶. *Fan et al.* use electrospinning method to fabricate a superhydrophobic surface by combining polyvinylidene fluoride (PVDF) and fluorinated silane molecules (FSM) on the glass. The samples have water contact angles of 170 degree and a very low water roll off angle less than 1 degree¹⁴. *Thieme et al.* modified a micro-structure on aluminum alloy substrate by chemical vapor deposition (CVD). A poly(tetrafluoroethylene)-like polymer (PTFE) was deposited and hexafluoropropylene oxide was used as precursor. For the other set of samples, a fluorine-free polysiloxane (PSi) was deposited by CVD with 1,3,5-trivinyltrimethylcyclotrisiloxane as precursor and di-tert-butyl peroxide as a free-radical-generating initiator¹³.

II. H. 3. Etching

Etching is another method to fabricate a superhydrophobic surface. The advantage for the etching method is the fabrication speed is fast. However, the etching method provides very little control for the size and the morphology of the micro-structure. In addition, contamination always obtains during the etching processes. A report suggests that etched surfaces may result in more durable water repellant surfaces. *Peng et al.* developed a durable superhydrophobic surface on aluminum by etching method. The aluminum plates were etched in a 2.5 M HCL solution for 8 minutes to form micro-structured surface. The micro-structured aluminum surfaces were dipped in a 1.0 wt % ethanol solution of PDES for 30 minutes to obtain superhydrophobicity with 160 degree contact angle⁸⁴. *A. Y. Vorobyev et al.* and *C. Guo et al.* were using femtosecond laser pulses to fabricate superhydrophobic surfaces on platinum, titanium and brass samples. The laser treated metal surfaces were initially hydrophilic, but the surface became superhydrophobic after exposure to air. They believed that the chemical reaction on the surface absorbs the carbon species, so that the surface can be tuned from hydrophilic to superhydrophobic after the laser ablation⁸⁵

II. I. Research Objectives

There are several questions related to the wetting behavior of rare earth oxide materials.

- Understanding factors that control wetting behavior
- Development of robust, water repellant coatings
- Development of scalable techniques for coating of large structures

Chapter III: Methods

III. A. Pulsed Laser Deposition

Ceria thin films can be fabricated by several methods, such as spray pyrolysis⁴⁹, ion-beam assisted deposition⁵⁰, thermal evaporation⁵¹, radio frequency magnetron sputtering⁵², plasma-enhanced chemical vapor deposition⁵³, sol-gel method⁵⁴, electron spray assisted vapor deposition⁵⁵ and pulsed laser deposition (PLD)⁵. We used pulsed laser deposition (PLD) to deposition the ceria thin films on substrate because PLD is a simple process for the deposition of oxide films. PLD allows processes in low temperature with the potential of accurately reproducing the stoichiometry of the target. In addition, PLD allows forming good quality and smooth thin films to reduce the roughness effect during the static water contact angle measurement.

PLD is one of the Physical vapor deposition (PVD) methods. PLD requires a high-powered excimer laser with wavelength in the UV range (157-400nm) and a high vacuum chamber. In figure 8, the PLD processes include rapid heating, vaporization of the target, and absorption by the vapor to form dense plasma, the ablation materials on the substrate and the nucleation growth of the films on the substrate. The high oscillating free electrons that are generated by laser light in the electromagnetic field collide with the atoms of the bulk material. Then, that energy transfers to the lattice of the target material. Finally the target materials are heated rapidly and removal the atoms from the bulk materials by vaporization.

The plasma consisting of ablated material expands normal to the target surface, which is then collected on the substrate of choice. This plasma is referred as laser plume. The

laser plume consists of atoms and molecules. The shape of the plume can be changed by the background pressure, background gas, laser energy and duration of the pulses. Therefore, the laser energy, number of pulses, the background pressure and background gas were specified during the ceria thin film growths.

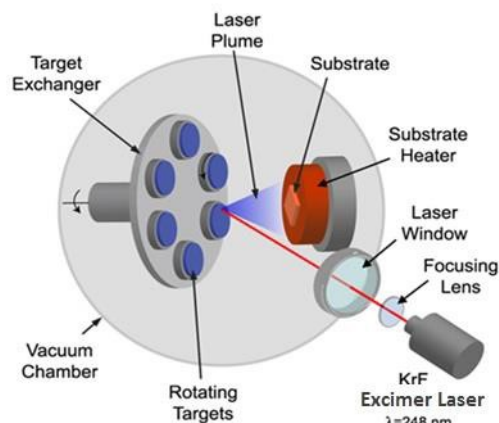


Figure 8. Schematic depiction of pulsed laser deposition

III. B. Wettability Characterization

The wetting behavior can be found by the measurement of the static water contact angle, roll off angle, contact angle hysteresis. A custom setup in figure 9 was used to determine water contact angle. A Nikon D3100 DSLR camera with macro-focusing teleconverter lens (Vivitar 2X) and Nikon 35 mm f/2.0-22.0 lens were used. A fixed 5 l volume of water was placed on the dry ceria thin films at room temperature generally (40–50% humidity). Then, the water contact angle images were captured and the contact angles were determined by image J software with “contact angle” plugins.



Figure 9. Image showing custom apparatus used to measure water contact angle

The roll off angle is the angle of inclination of a surface that the droplets begin to roll off. Hydrophilic surface results in larger roll off angle and contact angle hysteresis. To measure the roll-off angle, a sessile drop was placed on the surface and generally tilts the surface until the drop rolls off.

The contact angle hysteresis was measured by adding and reducing the volume of water. Figure 10a is the advancing contact angle which can be captured by adding the volume of water. Figure 10b is the receding contact angle which can be captured by reducing the volume of water. The contact angle hysteresis is determined by the difference between advancing contact angle and receding contact angle.

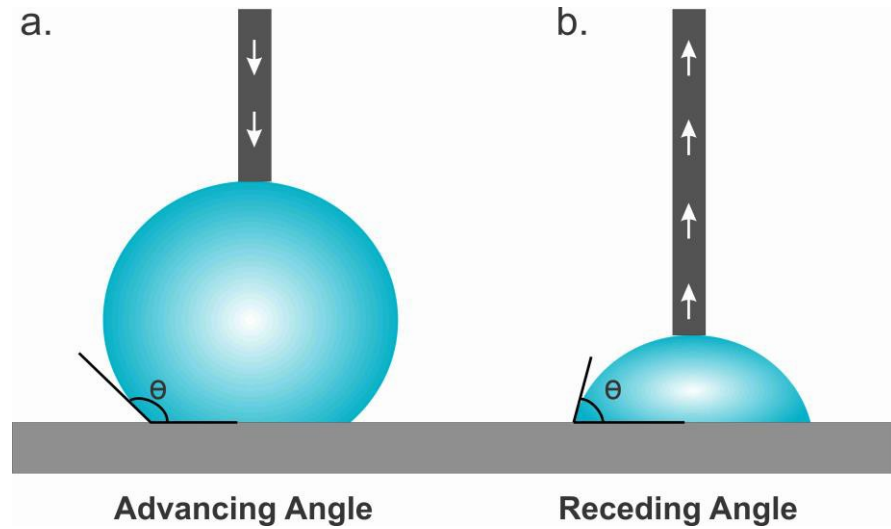


Figure 10. Schematic depiction of a) advancing contact angle and b) receding contact angle measurement

III. C. Bouncing Experiment

The wetting behavior on the dry surface also can be determined by droplets bouncing experiment. The setup for the bouncing experiment is shown in figure 11. The bouncing behavior of the impact droplets will be recorded by high speed camera (phantom V210) with film speed of 4100 fps. A fixed 5 l volume of water droplet with approximately 2 mm diameter was dropped on the surface at room temperature and 25% in ambient condition (40 ± 5% humidity). The impact velocity is varied.

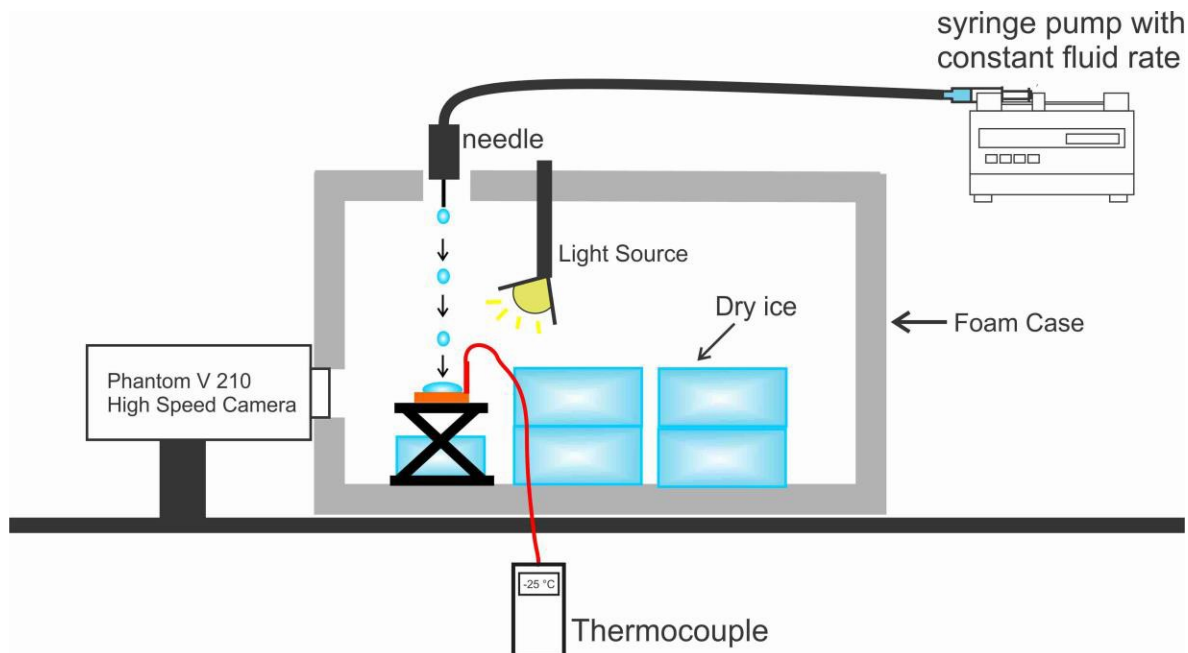


Figure 11. Schematic of the drop impact experimental setup.

III. D. Surface Morphology Characterization

The surface roughness was measured by atomic force microscopy (Burker Dimension Icon) Topographic images of the surface were captured using 2 m x 2 m scan area. In addition, optical profiler (Burker Contour GT-K) was used to measure the micro-scale surface roughness. The scanning area is 0.4 mm X 0.6 mm. The surface morphology was determined by scan electron microscopy (Raith 100).

III. E. X-ray photoelectron Spectroscopy

X-ray photoelectron spectroscopy (Thermo Scientific ESCALAB 250Xi) was used to determine the element composition, chemical state, and valence state of cerium and oxygen near the surface. In the figure 12, the principle of XPS is the X-ray source excites the photoelectrons on the material surfaces. The Ejected photoelectrons are

detected by the electron detector. The amount of detected electrons is referred to the amount of elements on the surface. The binding energy peak position is referred to the specific electron configuration of each element. The samples were analyzed using aluminum K radiation with an excitation energy of 1486 eV at Torr base pressure. The results were collected at a normal angle of 90 degrees with 50 eV pass energy and 500 m spot size. Software Advantage 5.9 was used to peak fitting and determine the surface stoichiometry. A static Shirley background was used to XPS results. The binding energy of the C 1s peak at 284.6 was used to as reference for the peak shifts. The concentration of the element can be determined by the equation below:

(9)

$\Sigma -$

is the concentration of the element.

is the area of I photoemission peak

is the sensitivity factor for the element

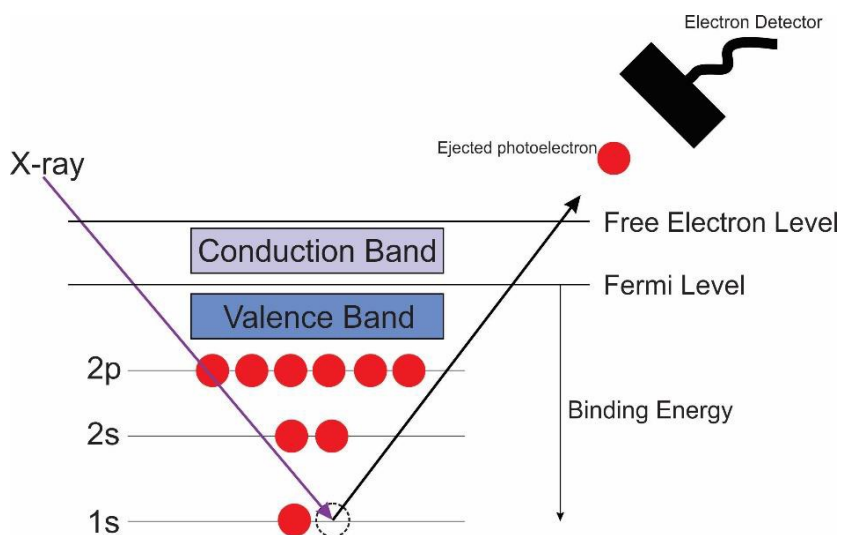


Figure 12. Schematic depiction of X-ray photoelectron spectroscopy

III. E. 1. Peak Fit of Ce 3d spectrum

The two most common oxidation state of cerium, Ce (IV) and Ce (III) can be resolved into five features in the Ce 3d_{5/2} and Ce 3d_{3/2}. V and U indicate the spin-orbit coupling for the Ce 3d_{5/2} and Ce 3d_{3/2} respectively. Ce (IV) has been matched to six peak listed below V (BE 880.6 eV), V'' (BE 888.85 eV), V''' (BE 898.4 eV), U (BE 901.05 eV), U'' (BE 907.45 eV), and U''' (BE 916.7 eV). V, V'' and V''' were respectively assigned to 3d⁹ 4f² Vⁿ⁻², 3d⁹ 4f¹ Vⁿ⁻¹ and 3d⁹ 4f⁰ Vⁿ Ce^{IV} final states. Ce³⁺ has been fitted with 4 peaks, V₀ (BE 880.6 eV), V' (BE 885.45 eV), U₀ (BE 898.9 eV) and U' (BE 904.05 eV). V₀ and V' were respectively assigned to 3d⁹ 4f¹ Vⁿ⁻¹ and 3d⁹ 4f⁰ Vⁿ Ce^{III} final states^{57, 58}. The valence states of Ce (III) and Ce (IV) are labeled on the curve-fitted regions of the Ce 3d spectrum in figure 13.

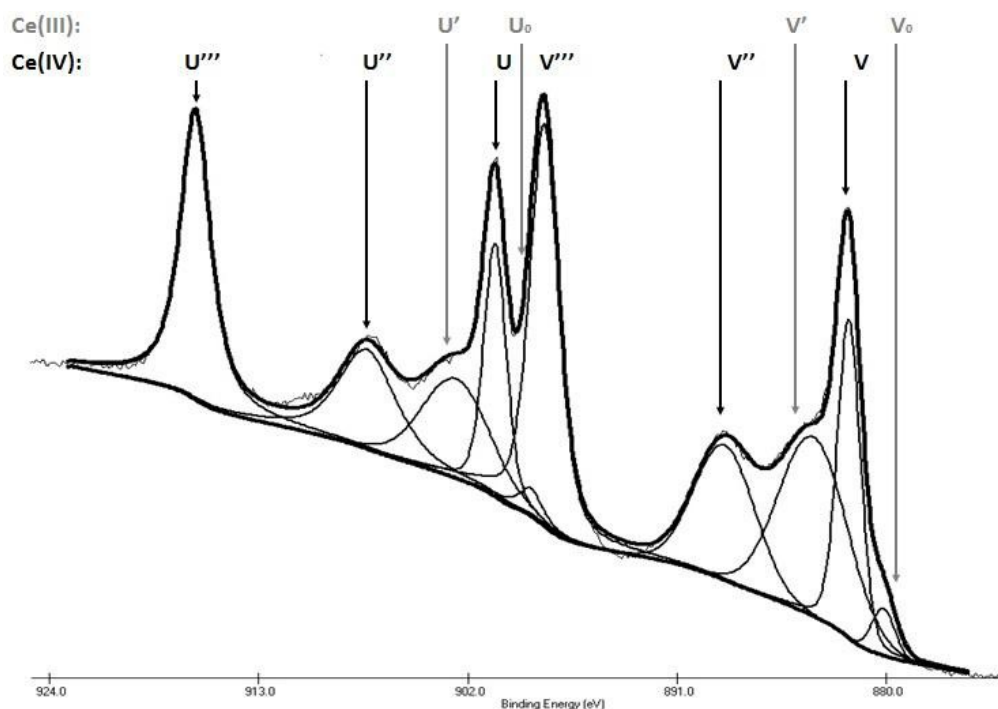


Figure 13. Ce 3d XPS peaks for CeO₂ films

III. E. 2. Peak Fit of O 1s spectrum

There are three main features for the O 1s spectrum in figure 14 of the ceria samples. O1 (~ 529 eV) is associated with O^{2-} anions in lattice of cerium. O2 (~531 eV) is a combination of surface hydroxyl and carbonates. O3 (~535 eV) is associated with adsorbed water on the surface.

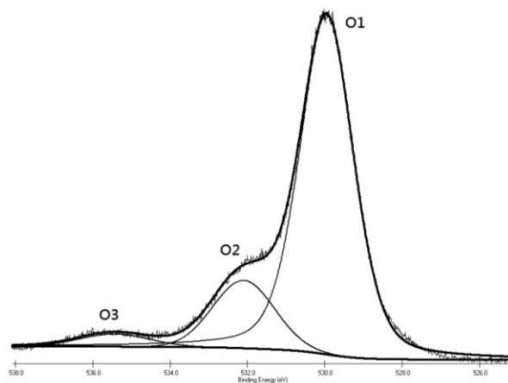


Figure 14. O 1s XPS peaks for CeO₂ films

III. E. 3. Peak Fit of C 1s spectrum

C 1s spectrum can be fitted in three main features in the ceria samples. In figure 15, C1 (~284.6 eV) is assigned to the carbon or hydrocarbon chains (C-C). C2 (~286 eV) is assigned as the carbon bonded to one oxygen as in alcohols or ether groups. C3 (~288 eV) is assigned as the carbon double bonded with oxygen (O-C-O, C=O) as in aldehydes or ketones. C4 (~289 eV) is assigned as the carboxyl or ester groups (O=C-O) ^{42, 56}.

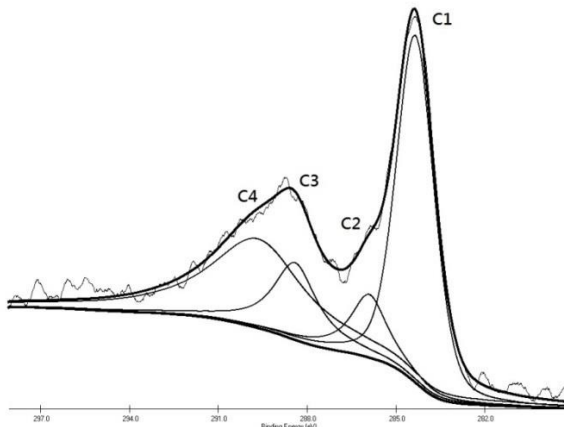


Figure 15. C 1s XPS peaks for CeO₂ films

III. F. UV Irradiation Treatment

The setup of the UV irradiation treatment was used to understand the reversible ability of wetting behavior on ceria thin films. A 254 nm wavelength UV lamp (ultra violet product S-52U) was used to irradiate the ceria samples at room temperature in air. The ambient annealing treatment was taken in 20% to 40% humidity. The ceria samples were irradiated inside of the UV absorbent chamber for 1 hour. The water contact angle was measured before the treatment, after the irradiation and after three days of storage in darkness at atmospheric conditions. Each sample was repeated for 6 cycles of the UV irradiation treatment.

III. G. Annealing Treatment

Annealing experiment was performed in ambient at 200 for 1 hour inside of the PLD chamber. The samples were placed on the PLD sample holder and annealed. The ambient annealing treatment was taken in 20% to 40% humidity. The samples were kept

inside of the chamber until cooling down to room temperature. In addition, the water contact angle was measured before the treatment, after cooling down to room temperature and after 3 days of storage in darkness at atmospheric conditions. Each sample was repeated for 6 cycles of the annealing treatment.

III. H. Durability Test

The durability of the coating was determined by two different tests: peels test and mechanical abrasion test. Peels test was performed by Scotch Transparent Tape (3M, Cat. 3157S). The tape was taped on the surface and then 500 g of weight was pressed for 10 seconds. The tape was peeled immediately at peels angle of 90 degrees normal to the surface. Mechanical abrasion test was performed by brushing the surface using flow-thru siding brush (Quickie). The abrasion speed was approximately 0.25 m/s with total weight of 340 g.

III. I. Stability Test

The stability of the coating was determined by boiling test, immersion in acidic environment and immersion in basic environment. For the boiling test, the samples were placed in a 70 mm diameter beaker with 200 mL hot boiling DI water for 24 hours. The hot plate temperature was set at 280 °C. For the immersion in acidic environment test, 0.01 M of hydrochloric (HCL) solution (~ 2 pH) was prepared. The samples were immersed in the acidic solution for 3 days at room temperature. For the immersion in basic environment test, 0.01 M of sodium hydroxide (NaOH) solution (~ 13 pH) was

prepared. The samples were immersed in the basic solution for 3 days at room temperature.

III. J. Ice Accumulation Test

The ice accumulation test customs setup was shown in figure 16. The samples were cooled down in the custom aluminum chamber at -10 (RH) environment for 1 hour. Sayon cooled incubator (MIR-154) was used to control the temperature and humidity condition. Then, fog was generated by humidifier and import inside to the chamber for 5 minutes. Ice crystals started to accumulate on the surface. The experiment was completed by defrosting the ice at the room temperature (40 % RH).

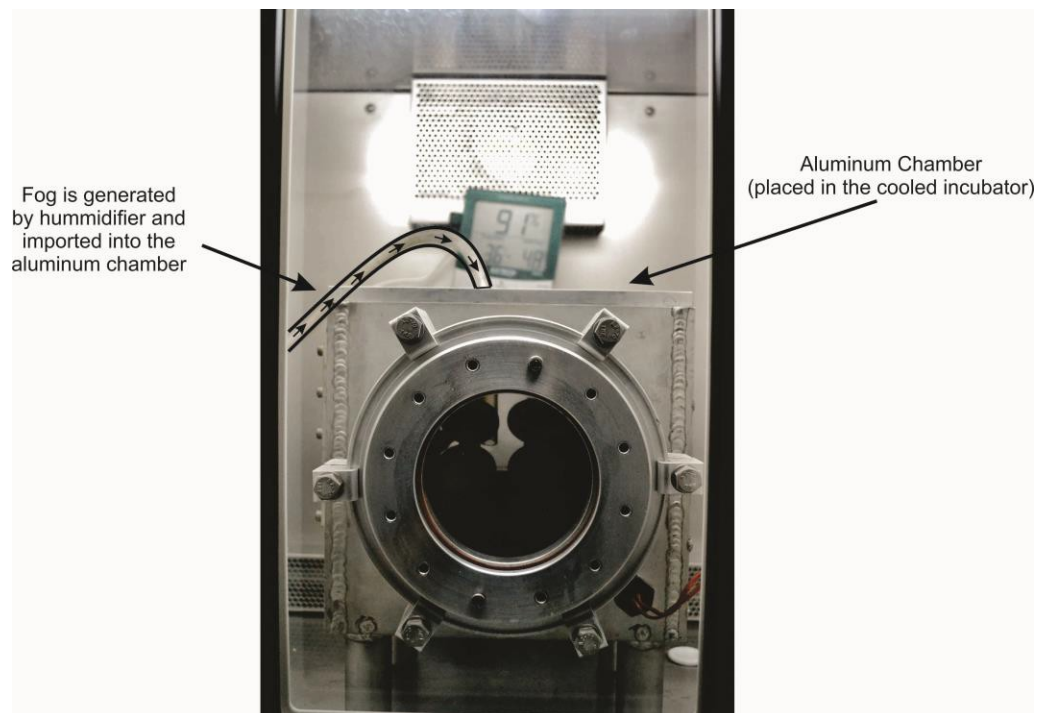


Figure 16. Image of showing custom apparatus used to ice accumulation test

III. K. Nano-Structure Synthesis Method

For the preparation of solution, 2.17g cerium (III) nitrate hexahydrate (STREM) and 5.8g hexamethylenetetramine (Alfa Aesar) were dissolved in 60 ml DI water. For the hydrothermal growth of CeO₂ nano-structure, aliquots of solution were sealed in 120 ml fluoropolymer digestion vessel (Savillex, MN, USA) and place into 70 °C water bath for 1.5, 3, 12 and 24 hours and stir at 300 rpm on the hot plate. The CeO₂ nano structure was synthesized and the white powders were cleaned by rinsing in DI water. The cleaned CeO₂ sample was dry on the hot plate for 1 hour at 80 °C. The hydrothermal nano-particles synthesis setup is shown in figure 17.

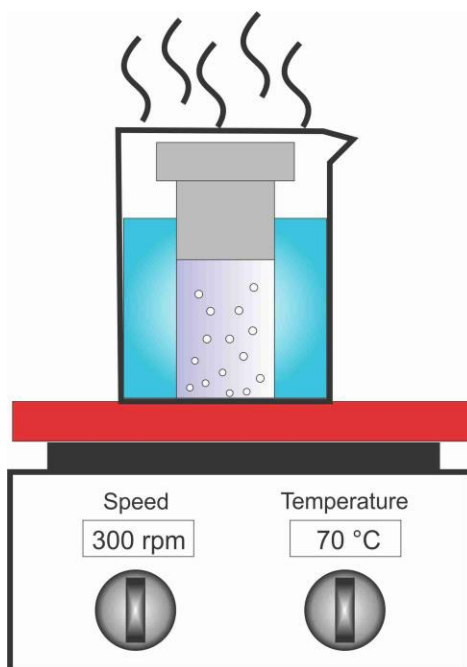


Figure 17. Image of showing hydrothermal nano-particles synthesis setup

Chapter IV: Wetting Behavior of Ceria Films

Ceria (CeO_2) is one of the rare earth oxide materials. In the last decade, ceria has been studied widely because of its attractive properties, such as high hardness ¹, high thermal stability ², high wear resistance ³, high capability release and storage oxygen ⁴, high refractive index ⁵ and high transparency ⁶. A recent study suggests that all rare earth oxide materials are hydrophobic due to screening of the $4f$ orbital ⁷. The unfilled electron shells in the $4f$ orbitals in rare earth oxide materials are shielded by filled electrons in their outer shells, which is believed to result in a lower tendency to bond with nearby water molecules resulting in hydrophobicity. In contrast, oxide materials generally have unfilled outer electrons shells in their outer orbits. These surfaces have a higher tendency to exchange electrons and bond with surrounding water molecules. Thus, oxide materials are generally hydrophilic ⁸.

However, the claim of intrinsic hydrophobicity of REO materials was countered by *Preston et al.* who suggested that the hydrophobicity of the REO materials is induced by adsorbed hydrocarbons ⁶⁸. *Khan et al.* claimed that the REO materials are intrinsically hydrophobic and also suggested that the hydrophobicity depends on the oxygen-to-metal-ratio at the oxide surface ⁶⁹. The question of whether REOs are intrinsically hydrophobic is still unsettled.

In this chapter, the intrinsic wetting behavior of CeO_2 surfaces will be studied. The thin films were deposited at different temperature and oxygen pressures on Si substrates by using pulsed laser deposition (PLD). Pulsed laser deposition method is able to form very smooth and high quality thin films to reduce the roughness effect during the

wettability characterization. The samples were divided into two different groups, those deposited in oxygen pressure of 50 mTorr and 1×10^{-6} Torr (vacuum) at different substrate temperature between room temperature and 700 °C. The experiments were repeated five times to ensure reproducibility. X-ray photoelectron spectroscopy (XPS) and water contact angle measurements were used for characterization of PLD CeO₂ films deposited under different conditions.

IV.A. The Effect of Oxygen Partial Pressure and substrate Temperature on the Wetting Behavior of Ceria Films

Figure 18a shows the water contact angle as a function of substrate temperature for two different sets of oxygen partial pressures: vacuum and 50 mTorr oxygen. The water contact angle measurements were taken 5 days after the deposition of the thin films with the samples being kept at ambient environment at room temperature (40-50% relative humidity). The results show the wetting behavior seems to be independent of the substrate temperature. There is a relationship between the wetting behavior and deposition oxygen pressure at the ceria surface. For the vacuum samples ($\sim 1 \times 10^{-6}$ Torr), the surface demonstrated hydrophobic behavior with static contact angle between ~ 90 degrees to ~ 100 degrees. On the other hand, the ceria thin films grown in 50 mTorr oxygen result in hydrophilicity with the static contact angle between ~ 25 degrees to ~ 35 degrees.

The time-dependence of the water contact angle was also studied to further understand the wetting behavior of ceria surfaces. Figure 18b shows the water contact angle as the time dependence after the thin films deposition at 200 °C in vacuum with the samples

kept in ambient environment. The ceria thin films initially had a water contact angle ~ 20 degrees after the deposition. After 1-2 days storage in ambient condition, the water contact angle increases to ~ 95 degrees to ~ 100 degrees. The results suggest that the ceria thin films were initially hydrophilic with hydrophobicity emerging after 24 hours to 48 hours.

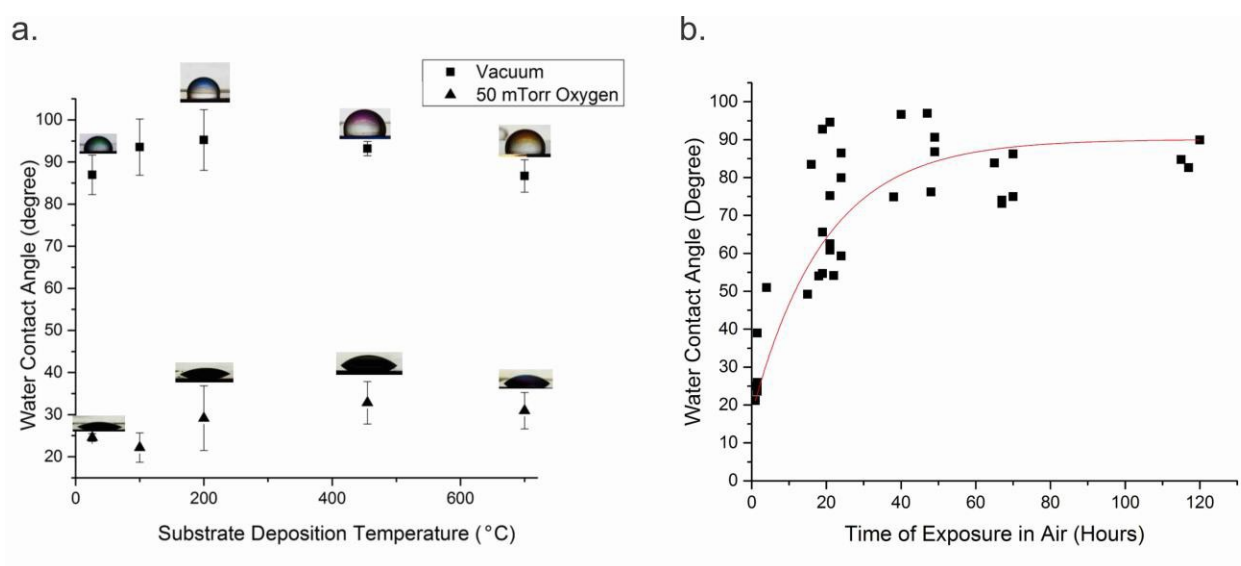


Figure 18 (a) wetting behavior of ceria thin films on the effect of substrate temperature and oxygen partial pressure and (b) time-dependent exposure in air to wetting behavior of ceria thin films deposited at 200 $^{\circ}\text{C}$ in vacuum.

IV. A. 1. Roughness of Ceria Thin Films

The surface roughness of the ceria thin films was measured by atomic force microscopy as shown in Figure 19. The average roughness of the thin films is 0.5 nm and 2.2 nm for those thin films deposited at 200 $^{\circ}\text{C}$ in vacuum and 50 mTorr oxygen, respectively. The results suggest that the ceria thin films are very smooth at the nano-scale. The surface

roughness slightly increases when the oxygen partial pressure increases. Thus, there is only a slight correlation of surface roughness with the water contact angle.

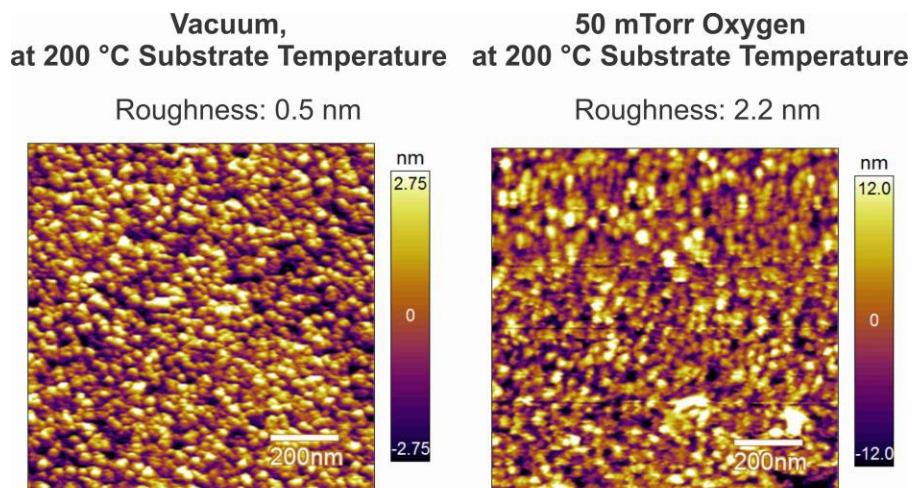


Figure 19. Roughness of ceria thin films deposited in different partial pressure

IV. A. 2. The Crystal Structure of Ceria Thin Films Grown by PLD

The XRD results in figure 20 show the crystal structure of ceria thin films grown at 200 in different oxygen pressure. CeO_2 (111) peak are found at 28.4 degree, when the thin films are deposited in vacuum and 50 mTorr environment. The thin films have a polycrystalline structure when deposited at low temperature. There is no correlation of material crystal structure with the water contact angle.

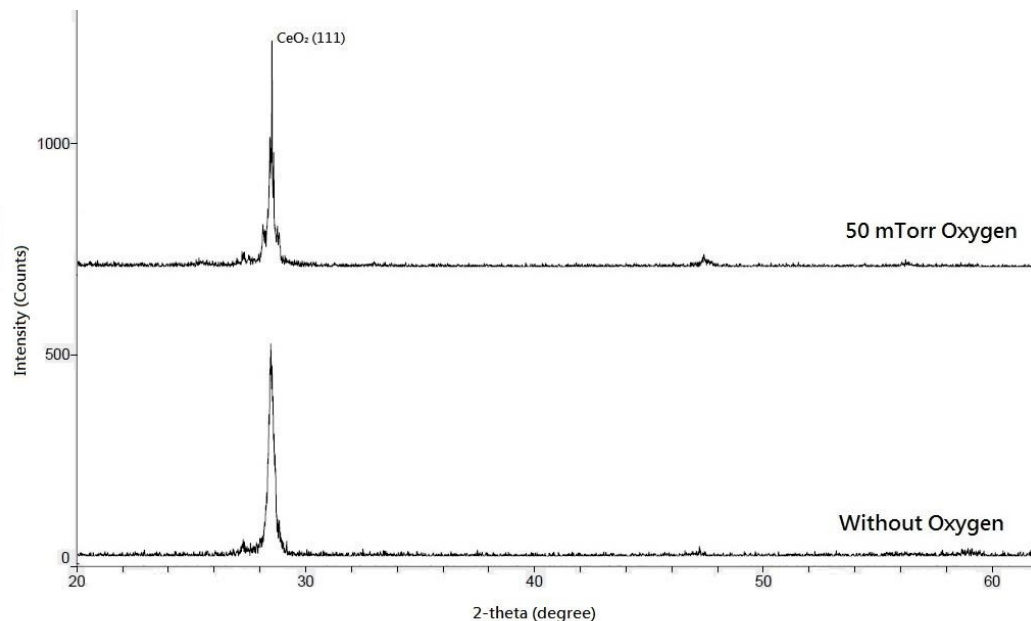


Figure 20. XRD diffraction pattern for ceria thin films deposited in vacuum and 50 mTorr oxygen at 200 °C.

IV. A. 3. Compositional Analysis by XPS

Figure 21 a-c shows the XPS spectra for the samples deposited in vacuum and 50 mTorr oxygen with 1 week storage in ambient environment. Figure 21a shows the XPS results for the Ce 3d spectra. The Ce 3d spectra suggests a slight increase in the concentration of Ce (III) in 50 mTorr oxygen. This is within the margin of error for the XPS. Figure 21b shows the XPS results for the O 1s spectra and it suggests that the OH-concentration is higher when the thin films are deposited in higher oxygen pressure. Figure 21c shows the XPS results for the C 1s spectra. The samples grown in vacuum have lower C3 and C4 components, which the C1 peak is dominant. In contrast, the samples grown in 50 mTorr oxygen have higher C3 and C4 component when the C1 component is lower (see figure 15 for C 1s peak assignment).

Figure 21 d-f shows the XPS spectra that were collected at different times for the samples grown in vacuum. Figure 21d shows the Ce 3d spectra and the results suggest there is slight increases with the concentration of Ce (III) after 1 week storage in ambient environment. Figure 21e shows the O 1s spectra and the result suggest the concentration of OH⁻ species slightly increases after 1 week of storage in ambient condition. Figure 21f shows the C 1s spectra and the results suggest that the C1 component increases after the deposition for 1 week.

In the observation for XPS spectra deposited in different oxygen pressure and the time-dependent studied after the deposition, the results show that the concentration of Ce (III) and OH⁻ have slight correlation with the water contact angle. However, the concentration of the hydrocarbon on the surface is believed to be a main factor on the wetting behavior of ceria surfaces. Further experiments will be performed to fully understand the role of the hydrocarbon in wetting behavior.

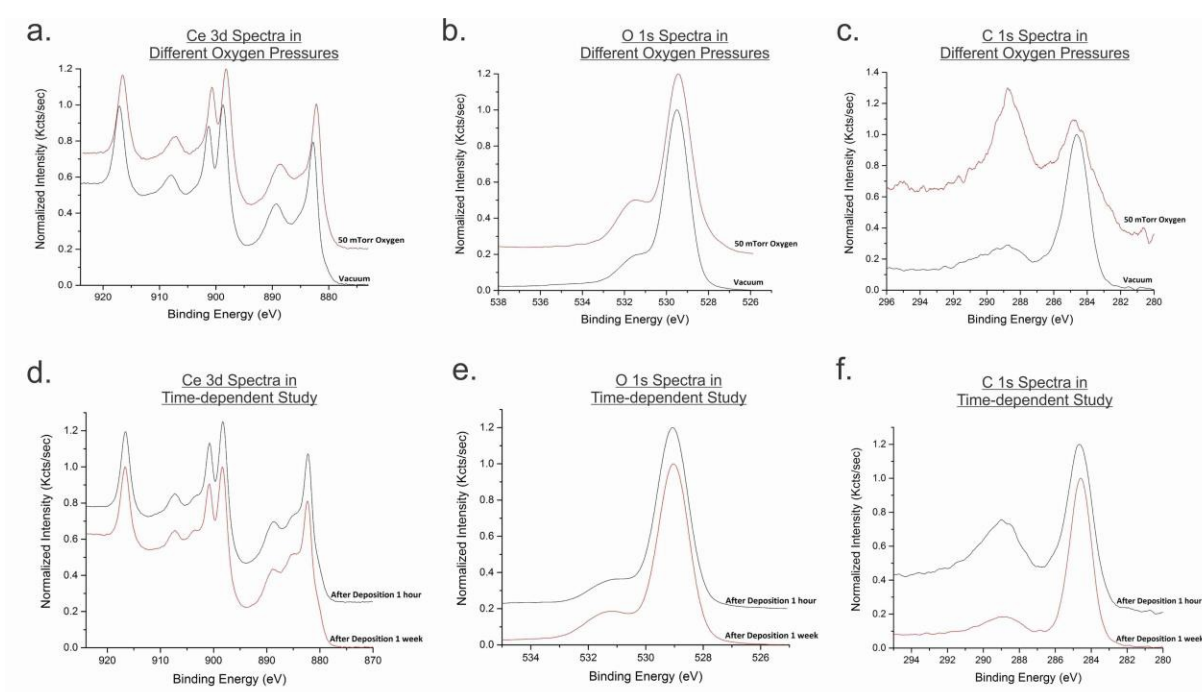


Figure 21. XPS spectrum for the ceria thin films grown in different oxygen partial pressure at 200 °C. (a) Ce 3d, (b) O 1s and (c) C 1s. In addition, the XPS spectrum was collected in different time after the deposition for the samples grown in vacuum (d) Ce 3d, (e) O 1s and (f) C 1s.

IV. B. The Effect of UV Irradiation Treatment in Air

The claim that REOs are intrinsically hydrophobic suggests that the wetting behavior can be tuned by an external stimulus. A UV irradiation treatment was performed in ambient conditions to understand the reversibility of wetting behavior on ceria thin films that were deposited in vacuum at 200 °C. The samples were exposed in the UV irradiation for 1 hour in air at room temperature. Then, the samples were stored in darkness for 3 days in ambient conditions. Figure 22a shows the water contact angle as a function of time after the initial 1 hour exposure to UV irradiation. The water contact angle decreases from ~95 degrees to ~20 degrees after 1 hour of exposure to UV irradiation. After 9 hours storage in darkness, the water contact angle recovers ~ 50% of

its initial value. The water contact angle recovers ~85% of its value after 3 days of storage in darkness. Figure 22b shows the reversibility of the water contact angle for 6 cycles of UV irradiation treatment. The results suggest that the reversibility decreased as the number of the UV irradiation cycles is increased. After 6 cycles of UV irradiation treatment, the maximum achievable contact angle is ~50% of the initial maximum obtained prior to the first UV irradiation treatment.

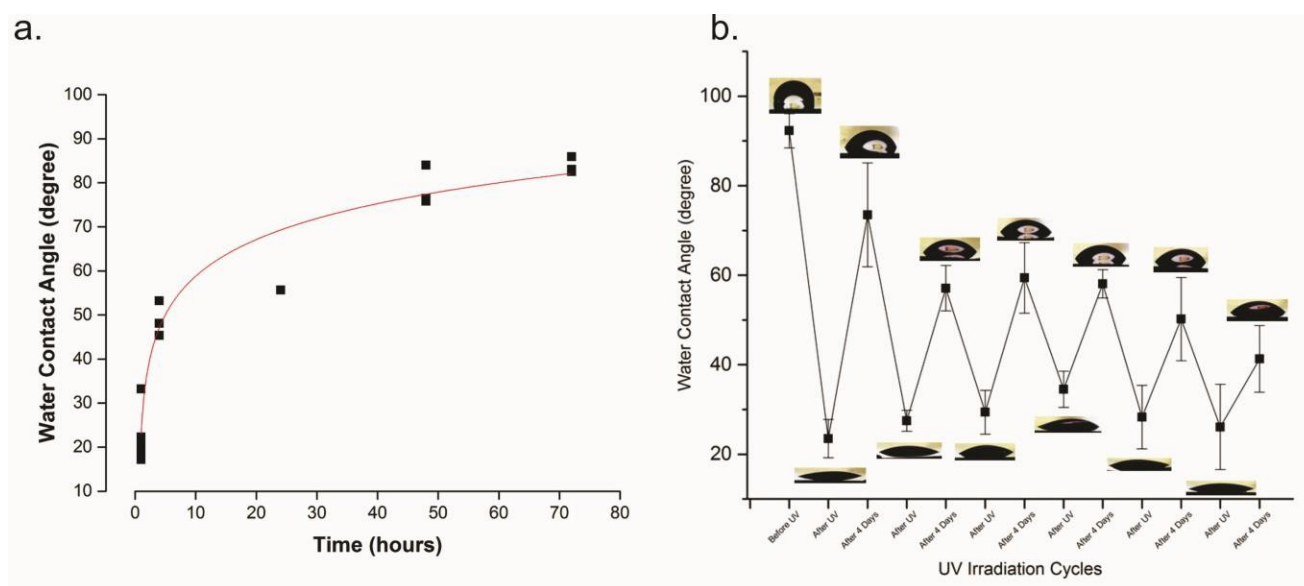


Figure 22. (a) The reversible wetting behavior over 72 hours after UV irradiation treatment in air. (b) The wetting behavior after 6 cycles of UV irradiation treatment in air.

IV. B. 1. XPS results for Ceria Films Exposed to UV Irradiation Treatment in Air

The XPS characterization of the samples is also performed for the UV irradiation cycles.

Figure 23a-c shows the spectra for Ce 3d, O 1s and C 1s on the ceria thin films after the UV irradiation treatment in air and after 1 week of storage in darkness. In figure 23a, the Ce 3d spectrum are very similar to each other, which indicates that the concentration of Ce (III) and Ce (IV) on the surface is not dramatically changed after the UV irradiation

treatment in air and after 1 week of storage in darkness. In the figure 23b, the O 1s spectrum shows the concentration of OH- slightly decreases after the UV irradiation treatment in air, then increases slightly after 1 week of storage in darkness. In the figure 23c, the C 1s spectrum shows the C3 and C4 peaks increase after UV irradiation treatment in air, then decrease after 1 week of storage in darkness. Table 1 shows the surface stoichiometry of carbon, oxygen, cerium and the ratio of O / Ce for the UV irradiation treatment in air. The concentration of carbon increases after the UV irradiation treatment and after 1 week of storage in darkness. However, the concentration of oxygen and cerium decreases after the UV irradiation treatment and after storage in darkness. The XPS results suggest that the wetting behavior does not seem to be related to the ratio of O / Ce because it is roughly the same after the UV the irradiation and after the storage in darkness. In addition, the wetting behavior seems to be related to the concentration of hydrocarbons at the surface. It suggests that higher hydrocarbon concentration is related to higher water contact angles.

Table 1. Relative concentration of various surface species on ceria thin films of the UV irradiation treatment in air

	C %	O %	Ce %	O / Ce
Before UV irradiation in air	14.6	57.9	27.5	2.11
After UV irradiation in air	17.4	56.1	26.5	2.12
After 1 week of storage in darkness	30.3	48.8	20.9	2.33

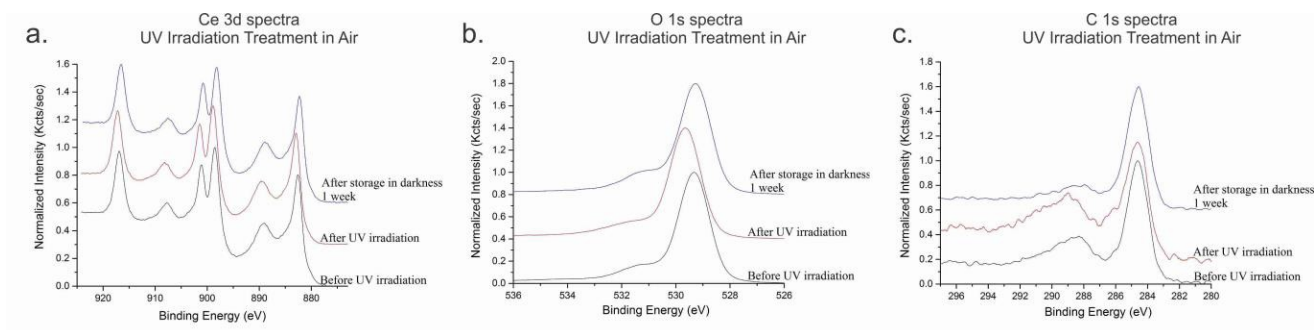


Figure 23. XPS spectrum for the ceria thin films of the UV irradiation treatment in air (a) Ce 3d, (b) O 1s and (c) C 1s.

IV. C. The Effect of Annealing Treatment in Air

Zubkov et al. and *Takeda et al.* studied the effect of hydrocarbon adsorption on the wetting of different oxide surfaces^{31, 87}. In this section, the effect of hydrocarbon adsorption and desorption on the water contact angle will be investigated by annealing heat treatment in air. Annealing heat treatment allows the hydrocarbon species desorb at the surface. Figure 24 shows the wetting behavior after 6 cycles of annealing treatment in air. The water contact angle decreases from ~ 95 degrees to ~ 40 degrees after 1 hours of annealing treatment in air at 200 °C. In the case of annealing heat treatment, the water contact angle recovers ~ 97% of its initial value after 3 days of storage in darkness. The contact angle is ~ 95% of its initial value after 6 cycles of annealing treatment in air. The annealing experiment results suggest that the hydrocarbon species at the ceria surface might be a main role to the wetting behavior.

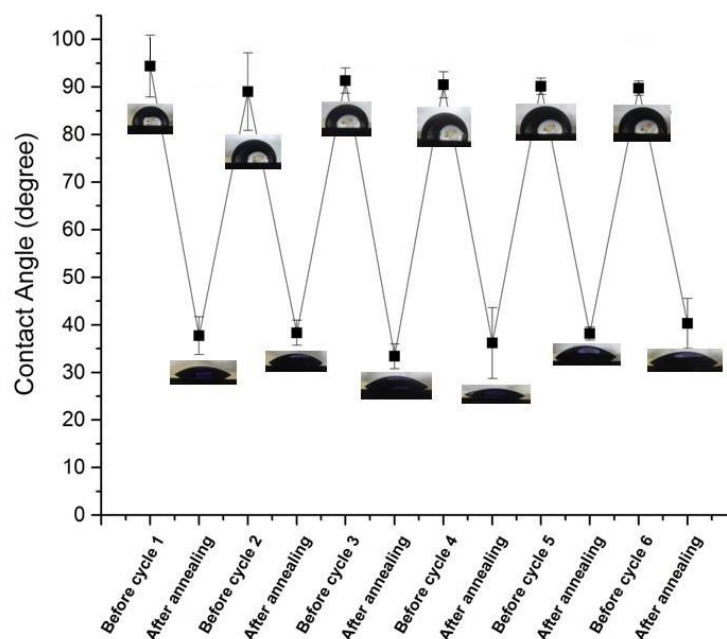


Figure 24. The wetting behavior after 6 cycles of annealing heat treatment at 200 °C in air

IV. C. 1. XPS Results for Ceria Films Annealing in Air

Figure 25a-c shows the XPS spectrum before and after annealing heat treatment in air. In the figure 25a, the Ce 3d spectrum indicates the Ce (III) concentration increases after the annealing treatment in air as the V' peak increases and then it decreases after 1 week of storage in darkness. In the figure 25b, the O 1s spectrum shows there is a little change in the OH- peak after the annealing treatment in air and after storage in darkness for 1 week. In the figure 25c, the C 1s spectrum shows the C3 and C4 components increase after 1 hour annealing treatment in air and then decreases after 1 week storage in darkness. Table 2 shows the surface stoichiometry of carbon, oxygen, cerium and the ratio of O / Ce for the annealing heat treatment in air. The data suggests that the O / Ce ratio slightly increases after annealing treatment and it corresponds to a decrease in the

contact angle. This is contrast to the work of *Khan et al.* who suggests the contact angle increases due to the increases the O / Ce ratio. The concentration of carbon decreases after the annealing treatment in air, then it increases after 1 week of storage in darkness. The data suggests that the hydrocarbon layer is removed by annealing treatment. It can determine the intrinsic wetting behavior of the ceria surface.

Table 2. Relative concentration of various surface species on ceria thin films of the annealing heat treatment at 200 in air

	C %	O %	Ce %	O / Ce
Before annealing in air	20.2	52.5	27.2	1.93
After annealing in air	15.2	58.2	26.6	2.19
After 1 week of storage in darkness	25.5	50.8	23.7	2.14

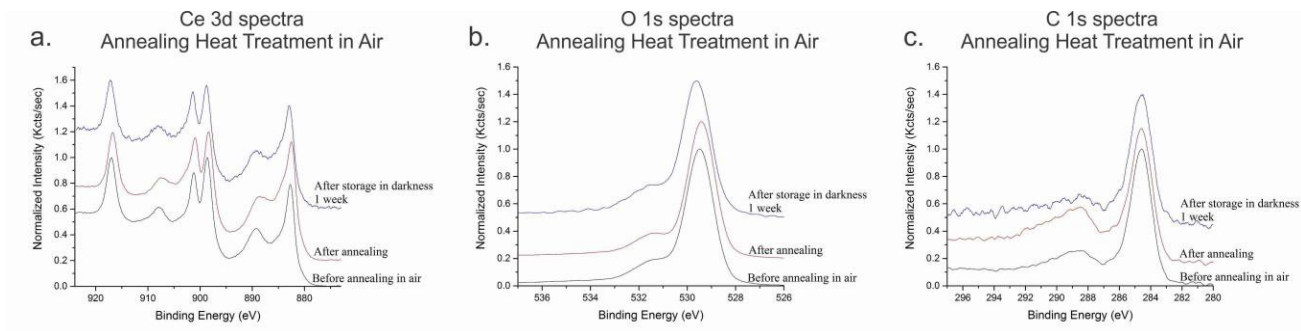


Figure 25. XPS spectrum for the ceria thin films of the annealing heat treatment at 200 in air (a) Ce 3d, (b) O 1s and (c) C 1s.

IV. D. Wetting Behavior for CeO₂ Films Storage in Air and Vacuum

The preceding experiments suggest that the hydrocarbons are mainly responsible for the wetting behavior of REO materials. However, all previous data was obtained after storage of the samples in ambient air. A critical experiment was performed to observe the time dependent behavior in different storage environments. A question needs to be

answered, would we observe the same time-dependent behavior shown in figure 18b if the ceria thin films were kept in high vacuum after the deposition for some time. Thus, the wetting behavior of ceria thin films storage in vacuum ($\sim 1 \times 10^{-7}$ Torr) for 5 days and after exposure to ambient air for 1 week will be observed and investigated. The ceria thin films were deposited at 200 in vacuum and kept inside the PLD chamber at that pressure for 5 days. The contact angle measurement and XPS characterization was performed immediately after removing the sample from the high vacuum environment. Then the samples were exposed to air and stored for 1 week in ambient conditions. Figure 26 shows the wetting behavior of ceria thin films stored in vacuum for 5 days and after exposure to ambient air for 1 week. The contact angle is ~ 48 degrees after 5 days storage in vacuum, increasing to ~ 102 degrees after exposure to ambient air for 1 week. Figure 18b and 22a shows that it is possible for the wetting behavior to transition from hydrophilic to hydrophobic behavior in 24 hours after the removal of the samples from the vacuum chamber. Therefore, figure 26 shows the wetting behavior of the ceria thin films is due to the storage conditions: ambient air and high vacuum.

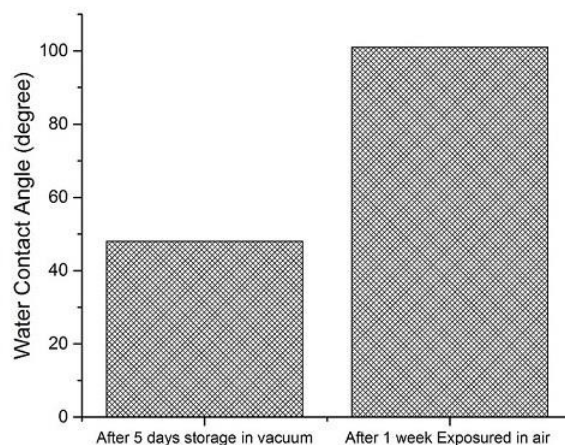


Figure 26. The wetting behavior of ceria thin films stored in vacuum for 5 days and after exposure to ambient air for 1 week

IV.D. 1. XPS Results for Ceria Films Storage in Vacuum

Figure 27a-c shows the XPS spectra after 5 days storage in vacuum and after 1 week exposure to ambient air for Ce 3d, O 1s and C 1s. For the Ce 3d spectrum, figure 27a, the V' peak slightly decreases after 1 week of exposure in air. For the O 1s spectrum, figure 27b, the OH- peak slightly increases after the exposure in air. For the C 1s spectrum, figure 27c, the C3 and C4 components decrease after the exposure in air. Table 3 suggests that adsorbing carbon compounds in air rapidly contaminate the surface as evidenced by the increase in carbon concentration from ~18.4% to 46.6% after removal from the deposition chamber and the concentration of cerium decreases from 29.9% to 10% on the contaminated surface.

Table 3. Relative concentration of various surface species on ceria thin films after 5 days of storage in vacuum and after 1 week exposure in air.

	C %	O %	Ce %	O / Ce
After 5 days storage in vacuum	15.8	54.3	29.9	1.8
After 1 week exposure of air	46.6	43.4	10	4.3

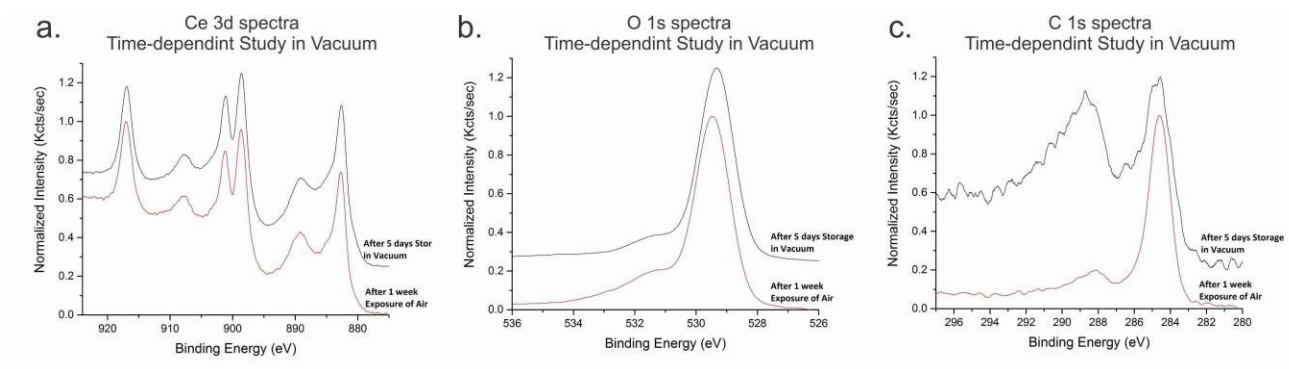


Figure 27. XPS spectra for the ceria thin films of after 5 days of storage in vacuum and after 1 week exposure in air (a) Ce 3d, (b) O 1s and (c) C 1s.

The wetting behavior of ceria thin films as a function of deposition pressure and substrate temperature, UV irradiation treatment and annealing treatment was studied. The results suggest that the wetting behavior of CeO_2 is controlled by the absorption of hydrocarbon at the surface. In general, oxide surfaces adsorb organic species from air, which can reduce the surface energy resulting in hydrophobicity.

Chapter V: UV Irradiation Effect on the Titanium Doped Cerium Films

In the previous chapter, the data suggests that the wetting behavior of ceria thin films is based on the chemical environment and may be further tuned by ultraviolet irradiation and annealing heat treatment. The ceria thin films were initially hydrophilic, but become hydrophobic after exposure to ambient air. The transition of the wetting behavior at the ceria surface is due to the adsorption of hydrocarbon species. In addition, UV irradiation and annealing heat treatment were used to convert hydrophobic ceria thin films to hydrophilic, with recovery of the hydrophobicity after store in darkness for several days.

Takeda et al. suggests that the electronegativities of the metal atom in the oxide control the wetting behavior for the oxide materials³¹. It further suggests that oxide with higher electronegativity increases the tendency to adsorb the hydrocarbon species, which the surface results in hydrophobicity³¹. In addition, they suggest that the ratio of $\text{OH}^- / \text{O}^{2-}$ ions on the surface controls hydrocarbon adsorption. The adsorption of carbon increases as the ratio of $\text{OH}^- / \text{O}^{2-}$ increases³¹. To date, there are no studies about the relationship of the adsorbed hydrocarbon and the wetting behavior on the two, mixed oxide surface, TiO_2 and CeO_2 .

In this chapter, the wetting behavior and the switchable wetting behavior of Ti-doped CeO_2 thin films will be investigated. The Ti-doped CeO_2 thin films were deposited on Si (100) substrate by pulsed laser deposition method. A CeO_2 (99.99% purity) target and Ti (99.99% purity) target were used during the laser deposition. The targets were rotated

and rastered to prevent pitting on the surface during the laser ablation. The Ti and CeO₂ targets were alternately ablated for 90 cycles. The thin films were deposited in high vacuum conditions (1×10^{-6} Torr) with the substrate temperature 200 °C. The role of the hydrocarbon species on the mixed oxide surface and the photo-resistant behavior will be discussed in the following sections.

V.A. The Effect of Electronegativity and Hydrophobicity in Oxides

Figure 28 shows the wetting behavior in the TiO₂ doped CeO₂ thin films. The TiO₂ samples have static water contact angles of 79 degrees. The CeO₂ thin films have static contact angles of 102 degrees. The doping samples (Ti50 CeO₂30, Ti50 CeO₂15 and Ti50 CeO₂8) have the static contact angle between ~96 degrees to 99 degrees. The water contact angle measurement were taken after 5 days of exposure to ambient air. Each experiment was repeated 7 times for the repeatability.

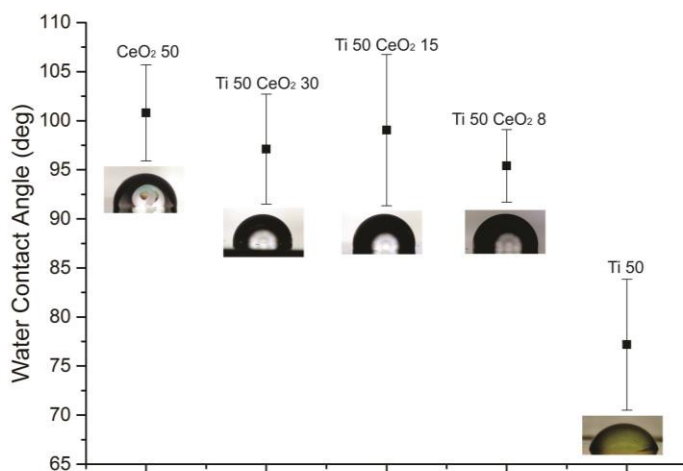


Figure 28. Wetting behavior of Ti doped CeO₂ thin films for those samples were deposited at 200 °C in vacuum condition.

V. A. 1. Roughness of the Titanium Doped Cerium Films

Figure 29 is atomic force microscopy results for the Ti-doped CeO_2 samples. The surface roughness and the morphology were determined. The results suggest that the Ti-doped CeO_2 thin films were very smooth. The surface roughness is 0.14 nm, 0.2 nm, 0.23 nm, 0.23 nm and 0.4 nm for the sample of Ti 50, Ti 50 CeO_2 8, Ti 50 CeO_2 15, Ti 50 CeO_2 30 and CeO_2 50, respectively. According to the surface roughness observation, there is no correlation to the wetting behavior to the surface roughness and the surface morphology.

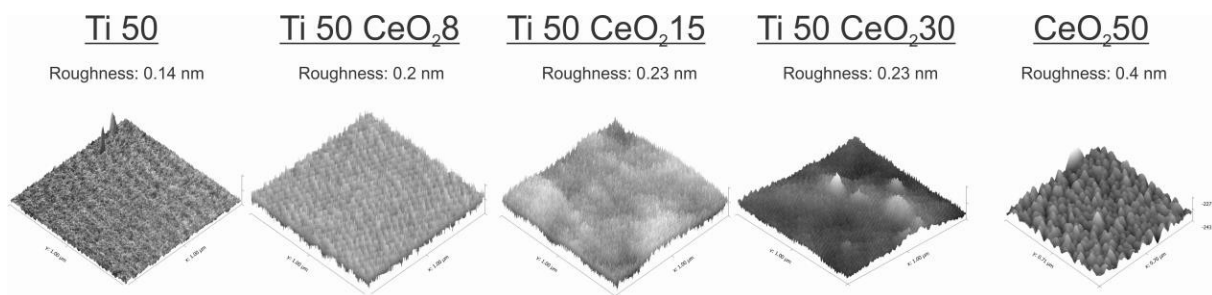


Figure 29. Roughness of Ti doped CeO_2 thin films which deposited in vacuum at 200 .

V. A. 2. XPS Results for the Titanium Doped Cerium Films

XPS surface characterization was used to determine the surface composition for the Ti-doped CeO_2 thin films. Table 4 shows the surface component for the carbon, oxygen, cerium and titanium. The XPS results suggest that the cerium concentration increase and titanium concentration decreases as the number of pulses for cerium increases. Thus, it confirms pulses laser deposition method can accurately control the ratio of cerium to titanium in mixed oxide films.

In addition, the concentration of carbon at the surface increases as the water contact angle increases when the CeO₂ 50 has a 102 degree static contact angle and Ti 50 has 79 degree static contact angle. This suggests that the electronegativity might control the hydrocarbon adsorption at the oxide surface, for which the wetting behavior will be different. Figure 30a-d shows the XPS results on Ti-doped CeO₂ thin films for C 1s, O 1s, Ce 3d and Ti 2p spectra. For the C 1s spectra, figure 30a, the C3 and C4 peak slightly decreases when the cerium concentration increases. For the O 1s spectra, figure 30b, the lattice oxygen peak shifts to the lower binding energy position when the concentration of cerium increases. The O²⁻ lattice of cerium is at ~529 eV and the O²⁻ lattice of titanium is 530.2 eV. The peak shift confirms the surface composition between the TiO₂ and CeO₂ on those samples. For the Ti 2p spectra, figure 30c, two main components were observed: Ti³⁺ (~456 eV) and Ti⁴⁺ (~458.3 eV). The XPS results show that TiO₂ thin films are dominated by Ti⁴⁺, but a small amount of Ti³⁺ still can be observed at the surface. For the Ce 3d spectra, figure 30d, it shows the oxygen defect increases as the cerium concentration is decreased. The presence of the V' peak which indicates Ce³⁺, is increased when the concentration of cerium increases.

In the observation for figure 30a-d and table 4, each oxide material has their unique wetting behavior because the amount of adsorbed hydrocarbon is dependent on the electronegativity of the metal atom for the oxide materials. *S. Takeda et al.* claimed that the wetting behavior of the oxide materials is related to the material electronegativities of the metal element directly bound to the oxygen atom. The electronegativity changes the surface polarity, which affects the absorption of OH⁻ groups at the surface. The OH⁻ group on the films is formed by the negative charge on the oxygen atoms. In general,

the OH⁻ group is hydrophilic, but it can become hydrophobic at the surface. *Takeda et al.* suggests that the OH⁻ group has a function as a trigger to adsorb the organic species in the air, such as hydrocarbon³¹. The XPS results suggest that larger electronegativity results in greater adsorption of hydrocarbons at the surface. The electronegativity of TiO₂ and CeO₂ () is calculated and it shows in table 5. It has been observed that CeO₂ thin films have larger contact angle and higher adsorption of hydrocarbon than TiO₂ thin films because the CeO₂ has larger electronegativity than TiO₂. Therefore, there is a correlation to the wetting behavior and the oxide material electronegativity of metal to oxygen atoms. The surface has higher contact angle when the negative charge on the oxygen atoms is larger because the surface can form more OH⁻ groups, which functions as a trigger to adsorb hydrocarbon.

Table 4. Relative concentration of various surface species on Ti doped CeO₂ thin films which deposited in vacuum at 200 °C.

	C %	O %	Ce %	Ti %
CeO₂ 50	49.2	36.9	13.8	0
Ti 50 CeO₂ 30	40.7	46.0	11.3	2
Ti 50 CeO₂ 15	41.5	40.4	11.5	6.6
Ti 50 CeO₂ 8	37.0	44.1	9.1	9.8
Ti 50	28.2	55.1	0	16.7

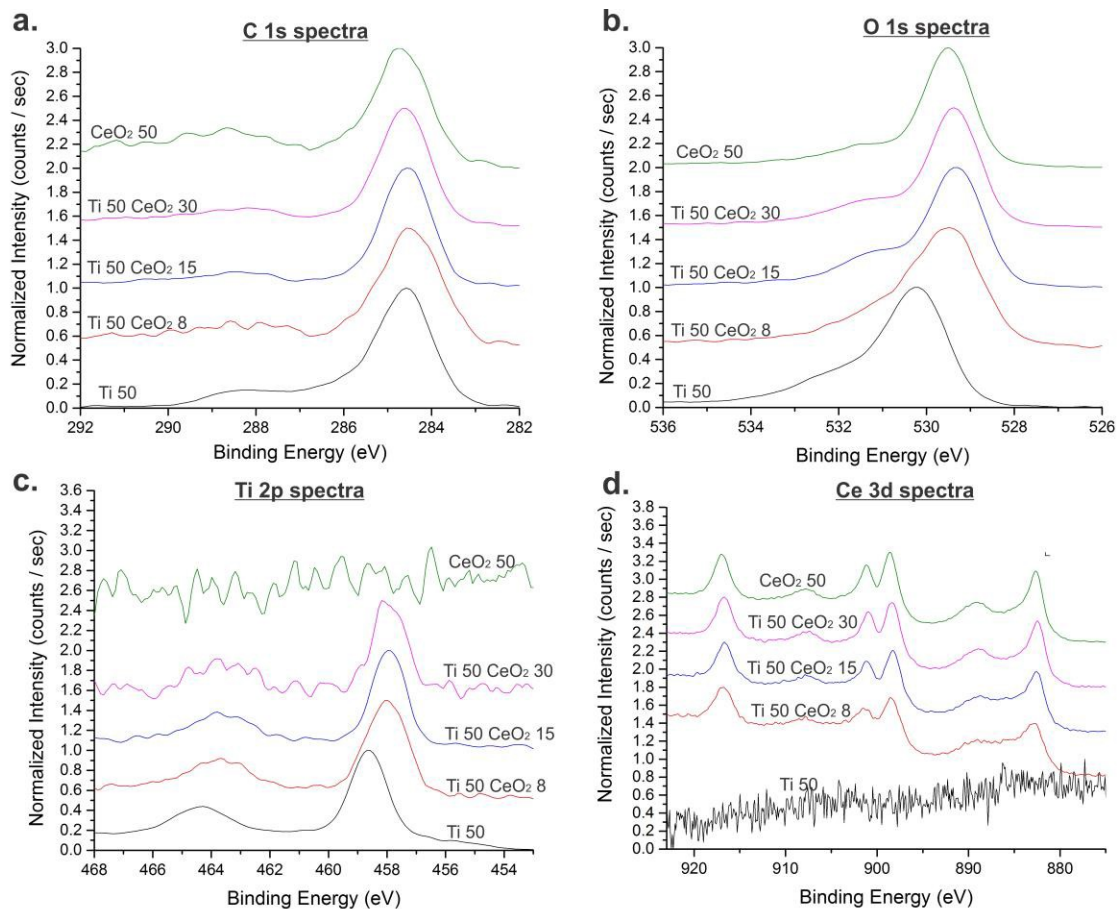


Figure 30. XPS spectrum for Ti-doped CeO₂ thin films which deposited in vacuum at 200 °C. (a) C 1s, (b) O 1s, (c) Ti 2p and (d) Ce 3d.

Table 5. Electronegative for TiO₂ and CeO₂

Element		Δ Metal - Oxygen
O	3.44	
Ti	1.54	-1.9
Ce	1.12	-2.32

V.B. 1. Wetting Characteristics due to UV Irradiation

Figure 31a shows the rate that water contact angle is reduced rate under exposure to UV irradiation. For the samples of Ti50 CeO₂ 8 and Ti50 CeO₂ 15, the reduction rate of the

water contact angle is slower than the other three samples Ti50, CeO₂ 50 and Ti50 CeO₂ 30, under the UV irradiation. The water contact angle on the CeO₂ 50 and Ti50 CeO₂ 30 decreases to ~24 degrees from ~100 degrees after 10 minutes exposure to UV irradiation. The similar behavior can also be observed on the Ti 50 surface. The contact angle decreases from ~79 degrees to ~24 degrees after 10 minutes of exposure to UV irradiation. However, the results shows the Ti50 CeO₂ 8 and Ti50 CeO₂ 15 samples have higher UV resistance. The water contact angle decreases from ~100 degrees to ~68 degrees for the Ti50 CeO₂8 and Ti50 CeO₂15 samples after 10 minutes exposure to UV irradiation. Figure 31b shows the wetting behavior reversibility over 6 cycles of UV irradiation treatment in ambient conditions. The wetting behavior can be recovered to 95% of its initial value after 6 cycles of UV irradiation treatment for the samples of CeO₂ 50, Ti50 CeO₂ 30, Ti50 CeO₂ 15 and Ti50 CeO₂ 8. However, the wetting behavior can only be recovered about the 85% of initial value for the Ti50 thin films. The results show titanium dioxide thin films have poor reversible wetting behavior in comparison to cerium dioxide thin films.

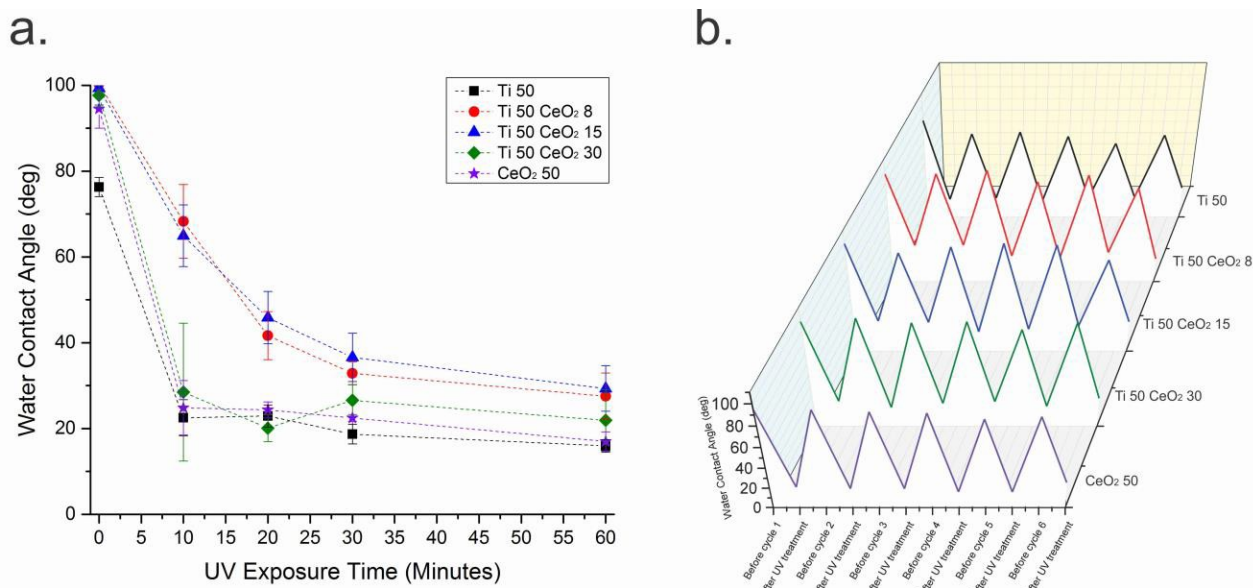


Figure 31. (a) The wetting behavior after UV irradiation treatment in ambient condition for Ti doped CeO₂ thin films. (b) Wetting behavior in 6 cycles of UV irradiation for the Ti doped CeO₂ thin films.

V.B. 2 XPS Results for Titanium-Doped Cerium Films Exposed to UV Irradiation in Air

Figure 32a shows that doping a small amount of CeO₂ in titanium can reduce the titanium dioxide susceptibility to UV irradiation. *Gao et.al* suggested that preventing photogenerated electrons and holes from the TiO₂ surface can reduce photocatalytic activity⁸⁸. The XPS spectra after the UV irradiation in ambient air was obtained to understand the role of cerium on TiO₂ in reduction of the UV irradiation activity. Figure 32a-d, Figure 33a-d and Figure 34a-c are the XPS spectrum after UV irradiation treatment for the Ti50 Ce O₂15, Ti50 CeO₂30 and CeO₂ 50 thin films, respectively. The XPS results suggest that the amount of Ce (III) decreases when the amount of pulses on the cerium target increases. The XPS results also show that the concentration of Ce (IV) slightly increases after 1 hour UV irradiation treatment and it decreases after 3 days

storage in darkness. The UV irradiation activity is dependent on the amount of the Ce (III) at the surface. The UV irradiation activity was reduced as the density of Ce (III) increased at the surface. Ce(IV) has a stable form because of the electronic structure $[\text{Xe}]4f^15d^16s^2$ and the empty inner 4f orbital shell. In contrast, Ce(III) will capture the holes to create an empty inner 4f orbital shell, resulting in Ce(III) cations being transformed to stable form of Ce (IV).

For the C 1s spectra, figure 32a, 33a and 34a, the XPS results confirm our earlier assertion that there is a correlation between the wetting behavior and hydrocarbon species at the oxide surface. A higher density of hydrocarbons at the surface will result in a higher static water contact angle. Figure 32a shows that the C3 and C4 components only slightly increase after 10 minutes of UV irradiation treatment for the Ti 50 and CeO₂ 15 samples whereas the C3 and C4 components dramatically increase for the Ti50 CeO₂ 30 and CeO₂ 50 samples. For the O 1s spectra, figure 32b, 33b and 34b, the XPS results suggest that the oxygen species (metal-oxygen bonds, OH) do not show a strong correlation to the wetting behavior after the UV irradiation treatment in ambient condition. For the Ti 2p spectra, figure 32c and 33c, there is no change in the Ti 2p spectrum after the UV irradiation treatment and after storage in darkness for 3 days. Therefore, Ti50 CeO₂ 8 and Ti50 CeO₂ 15 have a larger decrease in UV irradiation activity because the surface has high density of Ce (III), which can capture the holes at the surface. This is more evidence that there is a correlation between the wetting behavior and the concentration of hydrocarbons at the surface. The surface will become hydrophobic when the surface contains a higher density of hydrocarbon.

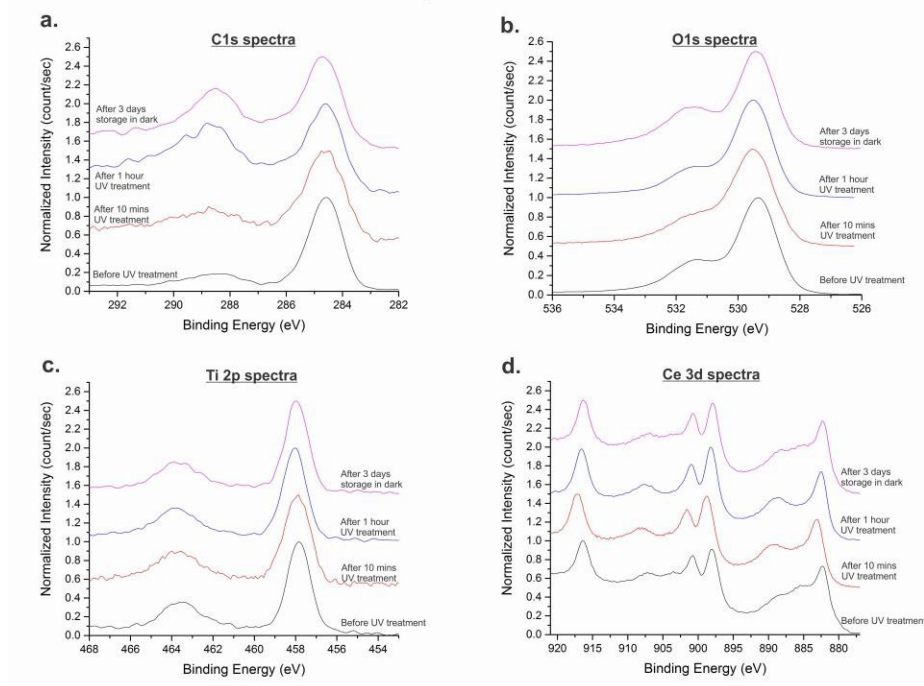


Figure 32. XPS spectrum for Ti 50 CeO₂ 15 thin films after the UV irradiation treatment in air. (a) C 1s, (b) O 1s, (c) Ti 2p and (d) Ce 3d.

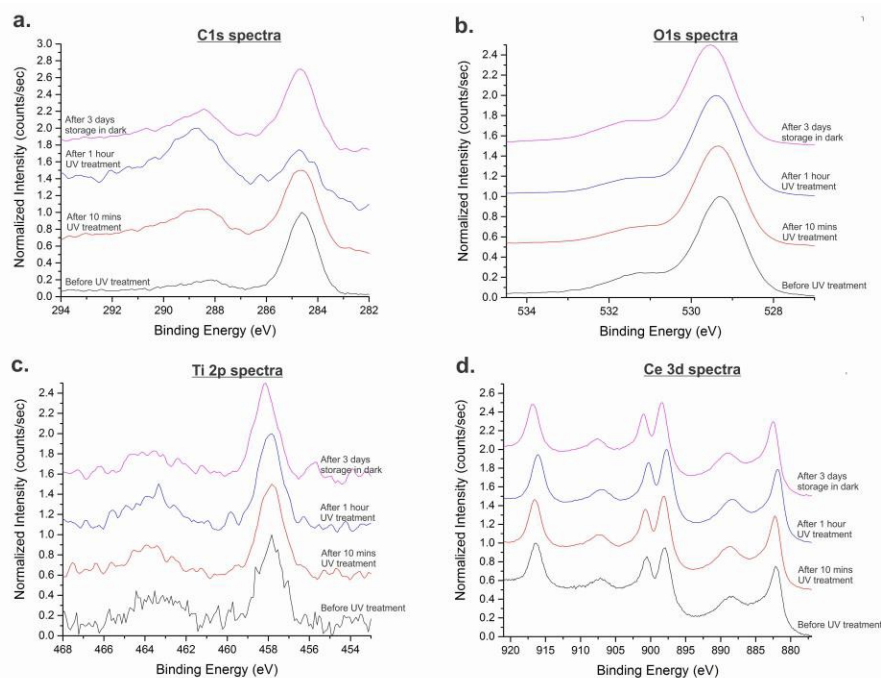


Figure 33. XPS spectrum for Ti 50 CeO₂ 30 thin films after the UV irradiation treatment in air. (a) C 1s, (b) O 1s, (c) Ti 2p and (d) Ce 3d.

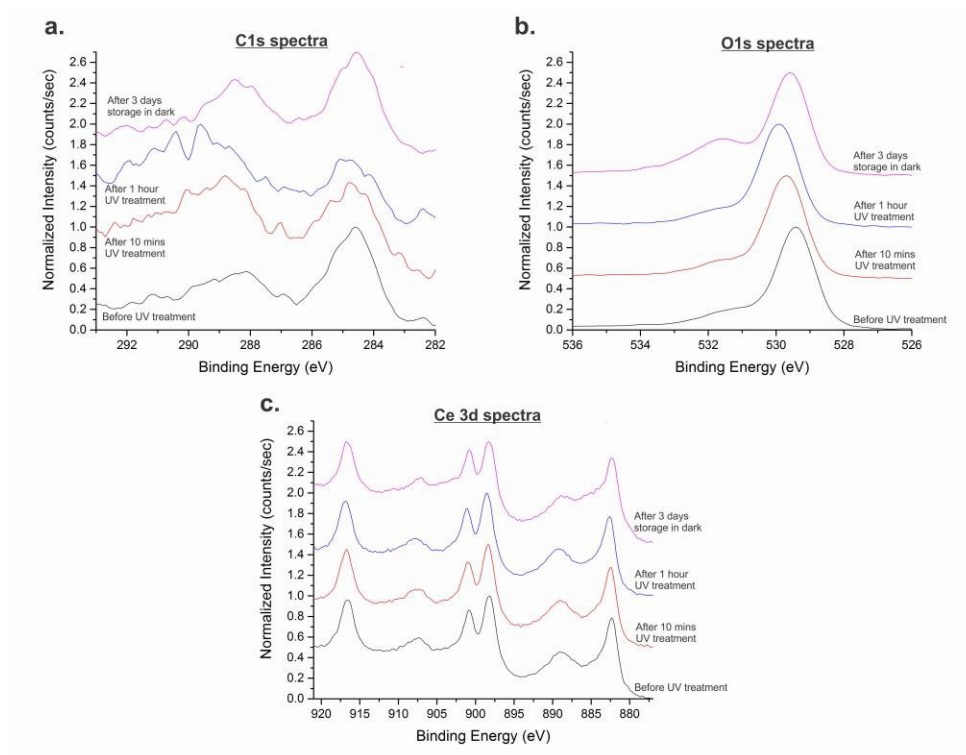


Figure 34. XPS spectrum for CeO₂ 50 thin films after the UV irradiation treatment in air. (a) C 1s, (b) O 1s, (c) Ce 3d.

Titanium oxide doped cerium thin films were deposited on Si substrate by pulsed laser deposition. The wetting behavior of TiO₂ and CeO₂ thin films depends on the electronegativity of the materials. The negative charge on the oxygen atoms will form the OH⁻ groups on the surface. The OH⁻ groups work as a trigger to adsorb the hydrocarbon species at the surface. The density of the hydrocarbon chains on the surface controls the wetting behavior of the thin films. A higher density of hydrocarbon chains results in a larger contact angle. In addition, the UV irradiation activity can be reduced by controlling the amount of Ce (III) at the surface. The Ce (III) anions can capture the

holes to transform to stable Ce(IV) that prevents the photogenerated electrons and holes at the surface.

Chapter VI: Fabrication of Cerium Dioxide Superhydrophobic Surface by Hydrothermal Method

Superhydrophobic surfaces have attracted interest from a fundamental science perspective and a number of applications, but the widespread has been limited by poor thermal stability and durability of state-of-the-art materials. Generally, polymers like as polymethyl methacrylate (PMMA) and polydimethylsiloxane (PDMS) have been widely used to form superhydrophobic surfaces because polymers have low surface energies.. However, polymers have poor thermal stability. To apply the superhydrophobic surface into more engineering applications, the surfaces must have high durability, good chemical stability, good thermal stability and UV resistance.

I will discuss efforts to develop a novel cerium dioxide superhydrophobic surface in this chapter. Cerium dioxide has a lot of attractive properties, such as anti-corrosion, high hardness, good thermal stability, good chemical stability and good wear resistance. In this chapter, the procedure for fabrication of the cerium dioxide superhydrophobic surfaces will be demonstrated. Anti-icing testing and the bouncing experiment will be performed to understand the wetting behavior of the superhydrophobic cerium dioxide surface.

Cerium dioxide superhydrophobic surface were deposited on 6061 aluminum alloys by hydrothermal method. Alloy substrates with dimensions of 1.75 inch diameter and 0.063 inch thickness were prepared to grow the cerium dioxide nanostructure. The alloy substrate was polished using 400, 600 and 1200 silicon grinding paper to remove the oxide layers. Then, the polished alloy substrate was ultrasonically cleaned in acetone for 10 minutes at room temperature.

For the preparation of the cerium nanostructures, 2.17g cerium (III) nitrate hexahydrate (STREM) and 5.8 g hexamethylenetetramine (HMT) (Alfa Aesar) were dissolved in 60 mL of DI water. For the hydrothermal growth of CeO₂, the polished alloy substrate was immersed into the solution with the polished surface facing up. Aliquots of each solution were sealed in 120 mL fluoropolymer digestion vessels (Savillex, MN, USA) and placed into 70 water baths for 1.5, 3, 12 and 24 hours. The CeO₂ nano structure was then grown on the alloy surface and was cleaned by rinsing in DI water. The cleaned CeO₂ sample was dried on the hot plate for 1 hour at 80 . A chemical modification to lower the surface energy was done by immersing the sample in the solution of stearic acid (STA) (Sigma-Aldrich) for 1 hour. The stearic acid solution was prepared by dissolving 0.01 g of stearic acid powder in 10 mL of ethanol. Finally, the treated CeO₂ sample was cleaned by rinsing in DI water and dried in air.

VI.A. Wetting Behavior of Superhydrophobic Cerium Dioxide Surfaces

The wetting behavior for the superhydrophobic cerium dioxide surfaces was determined by measurement of static water contact angle, contact angle hysteresis, roll-off angle and the rate of ice formation in freezing temperatures. The flower-like cerium nano-particles are initially superhydrophilic with ~10 degrees static contact angles. The surface becomes superhydrophobic with ~160 degree of static contact angle after 1 hour of stearic acid treatment.

VI. A. 1. Water Static Contact Angle

Figure 35 shows the static water contact angle for the superhydrophobic cerium dioxide surface after the stearic acid treatment. The superhydrophobic cerium dioxide coating provides very high water static contact angle on the hydrophilic 6061 aluminum alloy substrate. The superhydrophobic cerium dioxide samples (1.5 hours HMT, 3 hours HMT, 12 hours HMT and 24 hours HMT) have ~158 degrees water contact angle. Therefore, the cerium dioxide flower-like nano-particles can form superhydrophobic surfaces. A contact angle hysteresis measurement was then performed to understand the surface adhesion for those samples.

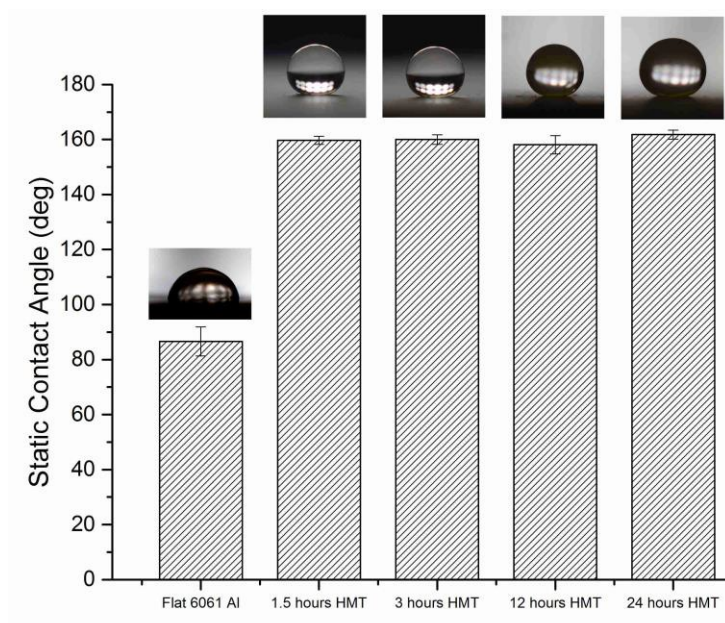


Figure 35. Static contact angle measurement for the superhydrophobic cerium dioxide surfaces after stearic acid treatment.

VI. A. 2. Contact Angle Hysteresis and Roll-off Angle

Figure 36a shows the roll-off angle for the superhydrophobic cerium dioxide surface. The water droplet did not roll off the flat 6061 aluminum surface, even though the

surface was tilted about 180 degrees. For the samples of 1.5 hours HMT, 3 hour HMT and 12 hours HMT, the surface provides very good water repellency because the water droplets roll-off the surface when it was tilted only about 1 – 3 degrees. However, the sample prepared for 24 hours using HMT has larger roll-off angle ~29 degrees.

Figure 36b shows the contact angle hysteresis for the cerium dioxide superhydrophobic surface. The sample with 1.5 hours HMT, 3 hour HMT and 12 hours HMT have ~2 degree contact angle hysteresis. For the 24 hours HMT samples, the contact angle hysteresis is ~5 degrees. There is a correlation to the roll-off angle and the contact angle hysteresis at the surface. A large contact angle hysteresis will result in a large roll-off angle. The results suggest that the reaction time between 1.5 hours to 12 hours is a preferred time to form superhydrophobic cerium dioxide surface with very high water repellency.

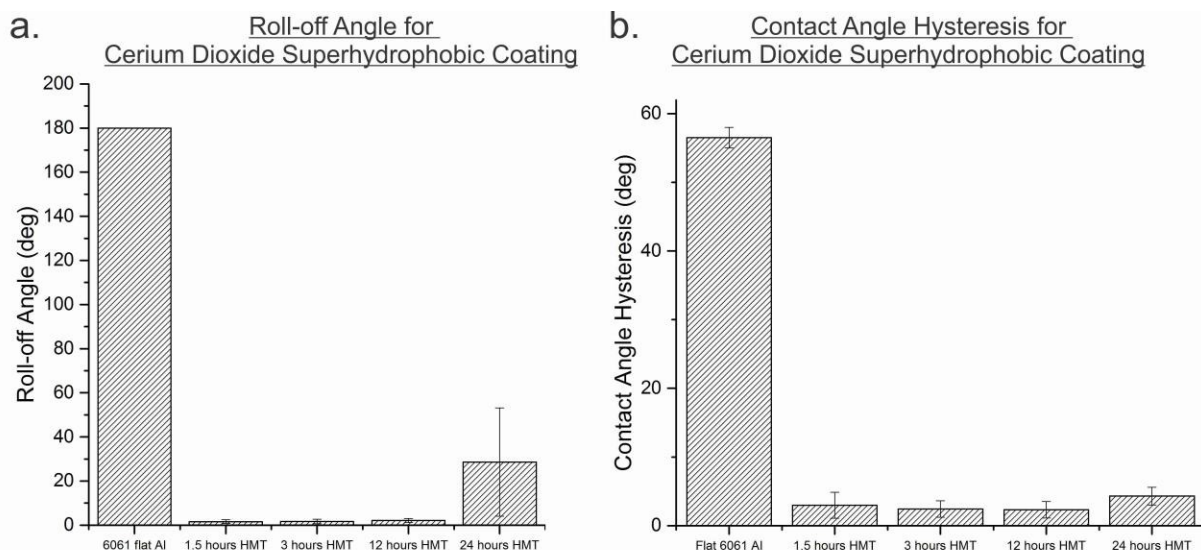


Figure 36. Wetting behavior for the cerium dioxide superhydrophobic coating after stearic acid treatment: (a) roll-off angle measurement and (b) contact angle hysteresis

VI.A. 3. Anti-icing Behavior

Figure 37 shows the anti-icing behavior of the superhydrophobic cerium-dioxide samples. After cooling down the surface to -10°C (RH 40% \pm 5) for 1 hour, there was no ice on the surface. Then, fog was generated by a humidifier and imported into the chamber for 10 minutes. After 10 minutes, ice formed on the surface and with two main shapes: flat or spherical. For the flat aluminum samples, 12 hours HMT and 24 hours HMT flat ice films are formed on the surface. On the other hand, most of the surface area for the sample of 1.5 hours HMT form a flat layer of ice, but there are some spherical shaped ice in some spots due to the non-uniformity of the surface. For the sample prepared with 3 hours HMT, spherical shaped ice is formed on the surface. The group of the samples was defrosted at room temperature (40 % RH) and the surface images were taken before defrosting and 5 minutes after the defrosting. For the sample made on flat aluminum and with 24 hours preparation time using HMT, the surface does not show superhydrophobicity because the water static contact angle is very small. For the sample with a 12 hour preparation time using HMT, some spots on the surface show superhydrophobicity and there are some high contact angle water droplets condense on the surface from the melting ice. In some spots, the ice never froze, surface was just coated with a film of liquid water. For the 1.5 hours HMT and 3 hours HMT samples, the surface is filled with a lot of small high contact angle droplets. In the anti-icing experiment, 3 hours HMT sample has the best icephobicity because the surface tends to form spherical shaped ice due to the high contact angles formed by condensed water droplets.

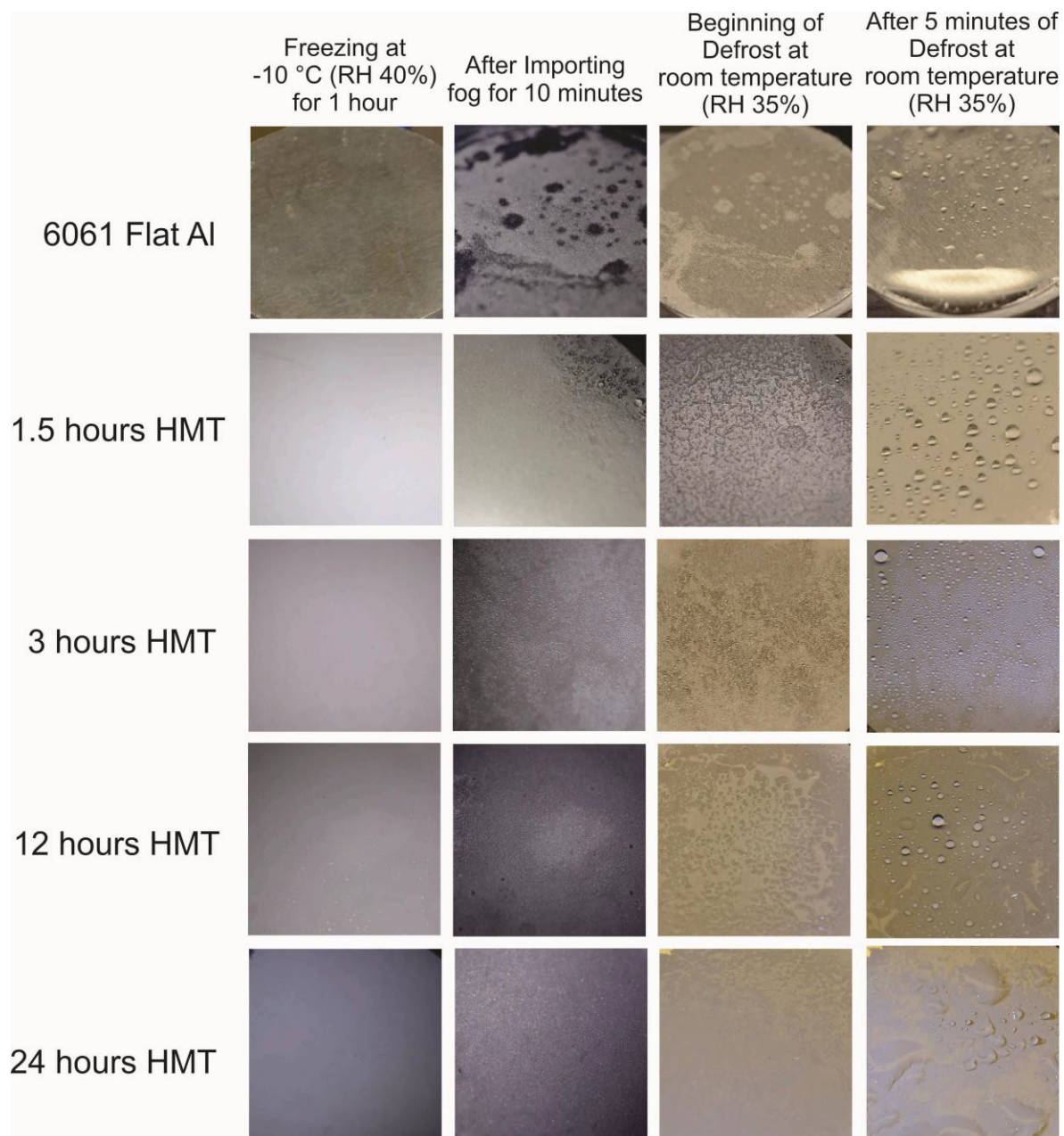


Figure 37. The anti-icing behavior for the superhydrophobic cerium dioxide surface.

VI. B. Surface Morphology and Surface Chemistry for the Superhydrophobic Cerium Dioxide Surfaces.

It is important to understand the effect of the surface roughness for the flower-like cerium dioxide nano-particles. Optical profiler and scanning electron microscopy was

used to measure the surface roughness and determine the surface morphology. In addition, the XPS characterization was used to confirm the surface composition for the cerium dioxide nano-particles.

VI. B. 1. Surface Stoichiometry of the Superhydrophobic Cerium Dioxide Surface

X-ray photoelectron spectroscopy (XPS) was used to determine the surface chemistry and the surface stoichiometry. The XPS characterization was performed on the samples prepared for 3 hours using HMT. Figure 38a-d shows the XPS spectra for the C 1s, O 1s, Al 2p and Ce 3d peaks before and after the stearic acid treatment. The cerium dioxide nano-particles are initially superhydrophilic after the hydrothermal synthesis processes. Then, the nano-particles become superhydrophobic after the stearic acid treatment with ~ 158 degree static contact angle. For the C 1s spectra, figure 38a, it shows that the hydrocarbon peak (~ 284.6 eV) becomes a dominant peak in the C 1s spectra after the STA treatment. In the previous chapters, the hydrocarbon species have been suggested to play a main role to control the surface wetting behavior at the oxide surface. For the O 1s spectra, figure 38b, there is no difference after the STA treatment. For the Al 2p spectra, figure 38c, the main peak (~ 74.3 eV Al_2O_3) slightly decreases after the STA treatment. The Al 2p spectra results suggest that the cerium dioxide nano-particles were coated by stearic acid after the treatment. The reduced intensity in the spectra is due to the reduction in the sensitivity of the electrons in the respective element. Similarly, the Ce 3d spectra, figure 38d, shows the intensity of peaks is slightly reduced after the treatment.

The surface has 16.2 % carbon, 57.5 % oxygen, 19.4 % cerium and 7 % aluminum before the treatment. After the treatment, the surface has 54.2% carbon, 33.2% oxygen, 9.4 % cerium and 3.2 % aluminum. Stearic acid is a saturated fatty acid with an 18-carbon chain in which the tail is water repellent. The concentration of carbon increases and the concentration of oxygen, cerium and aluminum decrease because a thin layer of STA is coated on the cerium dioxide nano-structure. Therefore, the stearic acid changes the wetting behavior of cerium dioxide surface from superhydrophilic to superhydrophobic, because of the long chain of hydrocarbon species.

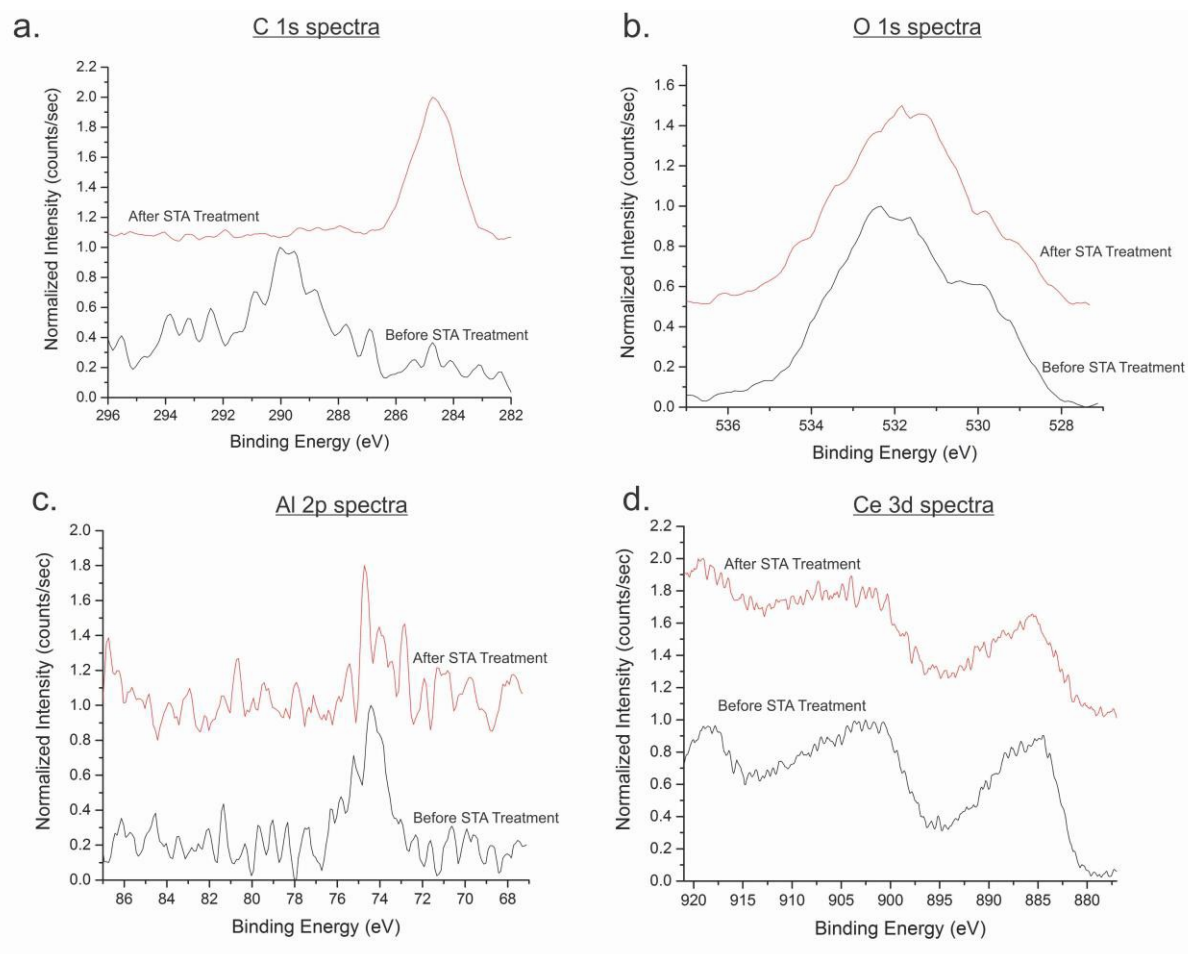


Figure 38. the XPS spectra for (a) C 1s, (b) O 1s, (c) Al 2p and (d) Ce 3d before and after the stearic acid treatment.

VI. B. 2. Surface Roughness of the Superhydrophobic Cerium Dioxide Surface

Surface energy and surface roughness are the main factors in forming a superhydrophobic surface. Table 6 is the optical profiler results for the cerium dioxide superhydrophobic surface. The surface roughness is shown for the cerium dioxide nano-particles formed by using different reaction times. The surface roughness is 3.94 μm , 5.07 μm , 2.81 μm and 2.68 μm for the 1.5 hours HMT, 3 hours HMT, 12 hours HMT and 24 hours HMT respectively. The surface adhesion increases when the surface roughness decreases.

Table 6. The surface roughness for the cerium dioxide nano-particles in different reaction time.

1.5 hours HMT	3 hours HMT	12 hours HMT	24 hours HMT
3.94 μm	5.07 μm	2.81 μm	2.68 μm

VI. B. 3. Surface Morphology of the Superhydrophobic Cerium Dioxide Surface

The SEM images, figure 39a-d, show that the surface roughness is controlled by the flower-like morphology. The flower-like nano-structure starts to form between 1.5 hours to 12 hours of the hydrothermal reaction time. After 12 hours in HMT solution, a second layer is formed on the nano-flake. After 24 hours in HMT solution, the double-layer covers the entire flower-like structure, reducing the surface roughness to 2.68 μm . It is believed that Cassie-Baxter state occurs for the samples with 1.5 hours, 3 hours and 12 hours HMT, as shown in figure 40. The air-pocket is trapped between the flower-likes nano-structure leading to a high static contact angle and low adhesion. On the other hand, the Wenzel state may occur for samples with 24 hours HMT. Wenzel state is

when the liquid penetrates between the nano-structures and when the surface adhesion increases. Therefore, the surface roughness affects the wetting behavior and the adhesion at the surface.

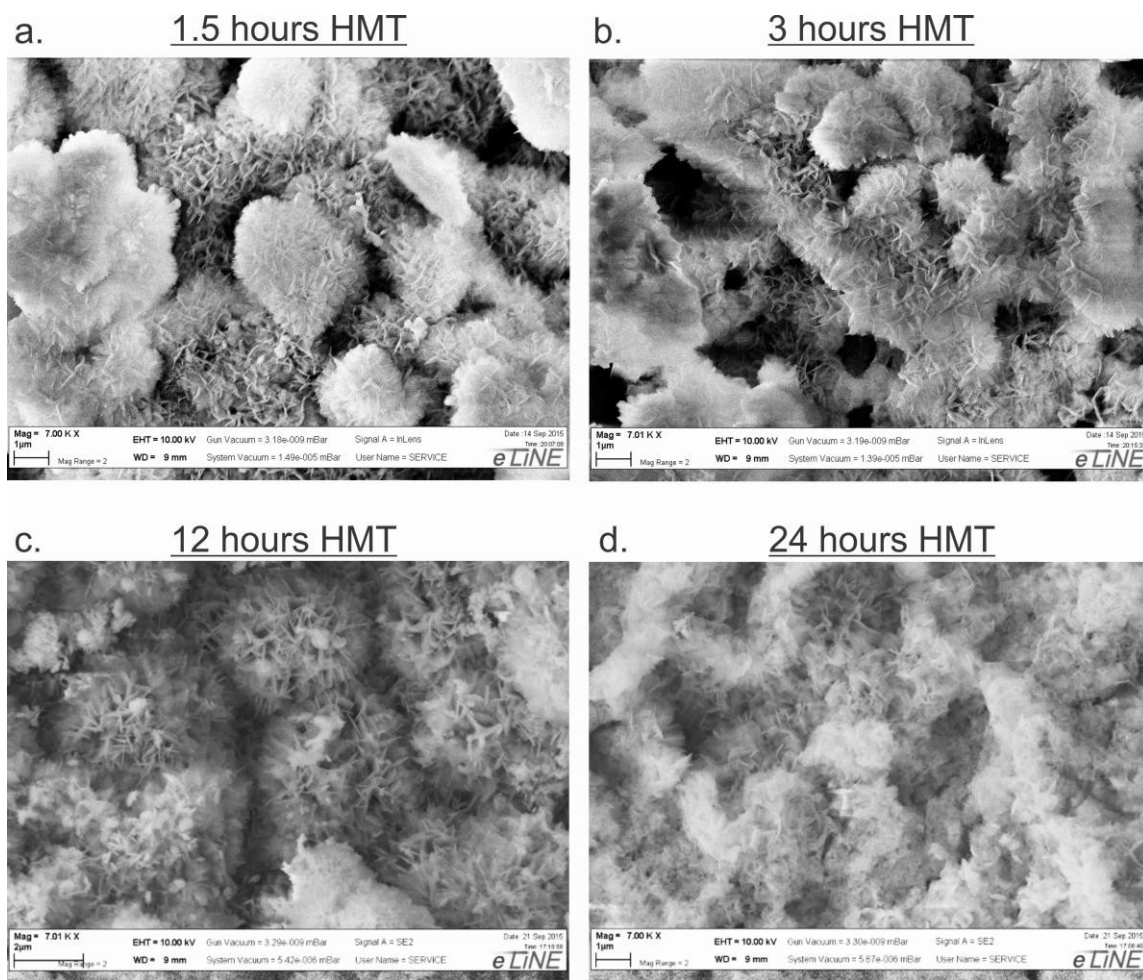


Figure 39. Scan electron microscopy images for the cerium dioxide nano-particles which synthesis in different reaction time, (a) 1.5 hours, (b) 3 hours, (c) 12 hours and (d) 24 hours.

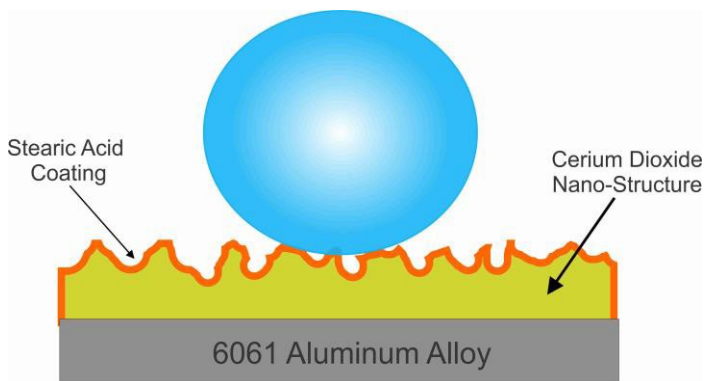


Figure 40. Schematic depiction of the cerium dioxide nano-particles coating on aluminum alloy substrate with Cassie-Baxter state.

VI.C. Dynamic Effect of Superhydrophobic Cerium Dioxide Surface

The bouncing experiment provides more information on the wetting behavior for the cerium dioxide nano-particles. At the spreading stage, the impact velocity spreads the droplet over the dry surface to form liquid lamella or a crown. *Yarin et al.* suggests that there are six kinds of shapes after water droplet impact on a dry surface: deposition, prompt splash, corona splash, receding break-up, partial rebound and complete rebound⁷². A high-speed camera was used to capture the receding break-up, complete rebound and partial rebound scenarios for the impact droplet on the dry superhydrophobic cerium-dioxide surface. Figure 41 shows the bouncing effect on a surface fabricated from cerium dioxide nano-particles at room temperature with impact velocity of 1.98 m/s. The high speed images show that receding break-up can be observed between 29.3 ms and 43.9 ms. After the droplet spreads out to the maximum diameter, the lamella starts to retract, causing some of the drops to be left behind. The receding lamella can break up into several numbers of fingers that can be further divided due to the invisible capillary wave⁷².

There is remaining kinetic energy in the liquid lamella at the end of the spreading. The kinetic energy is possibly not to fully be dissipated at the receding stage and it can still generate upward force in the liquid from the surface. In the bouncing experiment results, the capillary wave was reflected back from the surface and drives the liquid lamella upward between 43.9 ms and 131.7 ms. At 109.8 ms, the impact droplet completely bounces off from the surface for the samples made with 1.5 hours HMT and 3 hours HMT. However, the droplet partially bounces off from the surface for the samples of 12 hours HMT and 24 hours HMT. This partial rebounding behavior may be due to the high surface adhesion which restricts the upward force by the capillary wave. The high-speed camera image for the impact droplet on the dry superhydrophobic cerium-dioxide surface demonstrates the effect of the surface adhesion and bouncing behavior. Low adhesion surfaces can easily make the impact droplet completely bounce off from the surface.

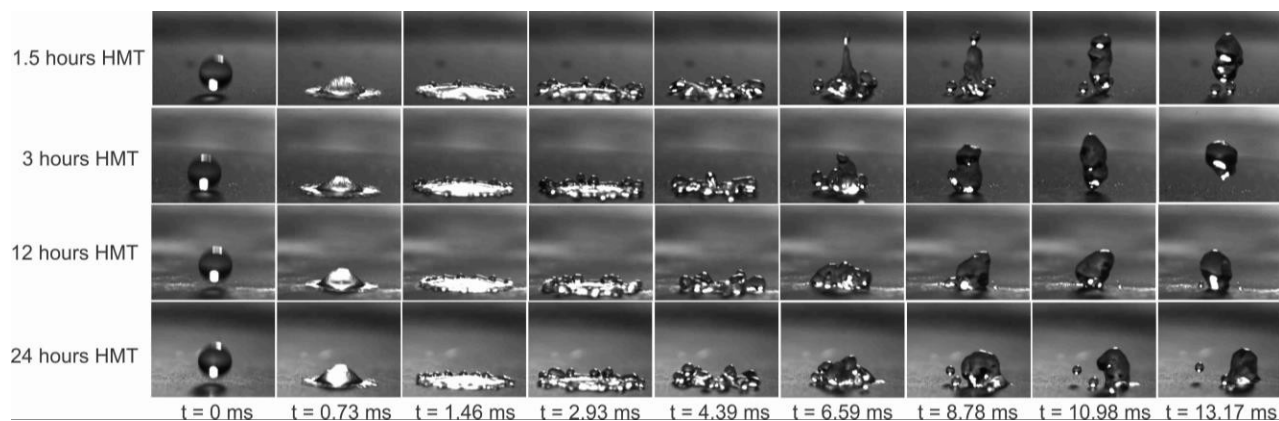


Figure 41. Bouncing effect on cerium dioxide nano-particles surface at room temperature with impact velocity of 1.98 m/s.

Figure 42 shows the bouncing behavior of water droplets on cerium dioxide nano-particles surfaces at -25 surface temperature with impact velocity of 1.98 m/s. The results suggest that the surface has higher adhesion at the cold temperatures. The droplets on the 1.5 hours HMT and 3 hours HMT surfaces partially rebounded after the impact; in contrast, they completely rebounded at room temperature. For the samples of 12 hours HMT and 24 hours HMT, deposition was observed on the cold surface. In this observation, it shows that the wetting behavior is dependent on the surface temperature. The cold temperature changes the viscosity and surface tension of the water droplet. The impact droplets are more likely to deposit on the cold surface instead of rebounding. In addition, the bouncing experiment at -25 results shows the samples of 1.5 hours and 3 hours have very good anti-icing property.

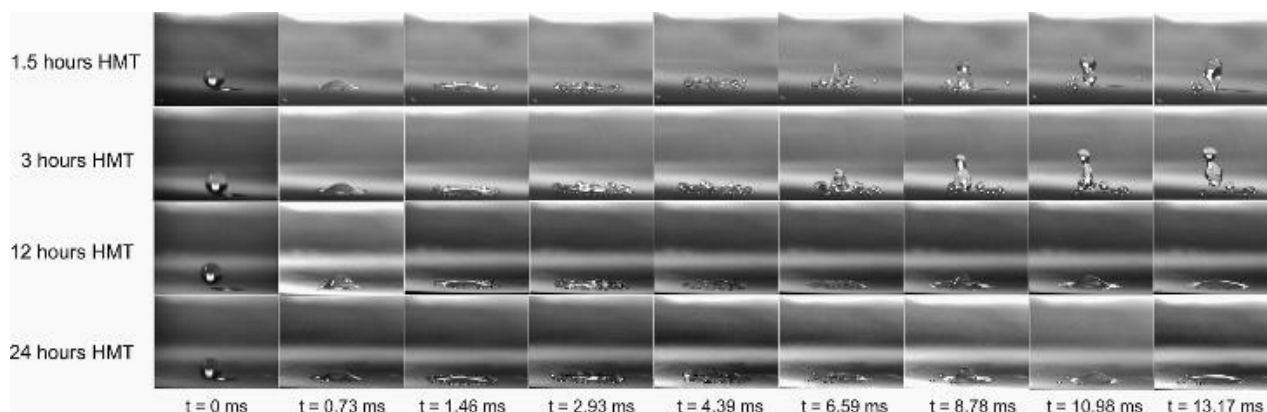


Figure 42. Bouncing effect on cerium dioxide nano-particles surface at -25 with impact velocity of 1.98 m/s.

The superhydrophobic cerium-dioxide surfaces were fabricated by a two-step processes: hydrothermal method to form flower-like nano-structures and reduction of the surface

energy by stearic acid coating. The surface has a very high superhydrophobicity with ~160 degrees static contact angle, but the surface adhesion depends on the surface roughness and the thickness of the coating. The bouncing experiment shows the surface adhesion affects the droplet impact and rebound from the surface. In addition, the ice-formation depends on the surface roughness. The results demonstrate the coating has extremely high water repellency, but the durability and stability is very poor. In addition, the uniformity of the films is very poor and the volume of solution and vessel used to prepare the nanostructures limits the amount of the coating. Therefore, a durable and stable superhydrophobic coating that can be applied on a large area is needed.

*** Dr Rakesh Prasad Sahu and Dr Alexander Yarin were contributed to the works in this section for the experiment of bouncing behavior at room temperature and sub-zero temperature on superhydrophobic cerium dioxide coating.**

Chapter VII: Fabrication of Chemical and Thermal Stable Cerium Dioxide Nano-Composite

The wetting behavior of cerium dioxide thin films by pulsed laser deposition and the fabrication of superhydrophobic cerium dioxide coating by hydrothermal method was studied in previous chapters. The XPS results suggest that the hydrophobicity of the cerium dioxide is induced by absorption of hydrocarbon. In addition, the fabrication of superhydrophobic cerium dioxide nano-particle coating was developed in the previous chapter. However, the superhydrophobic cerium dioxide coating by hydrothermal method has very poor uniformity, poor thermal stability, low adhesion and low wear resistance. In addition, polymers like polydimethylsiloxane (PDMS) have been used widely to form superhydrophobic surfaces currently, but they suffer from poor thermal stability and limited mechanical durability. The poor durability and stability of the current state-of-the-art superhydrophobic surfaces limits the use of these remarkable materials. Therefore, a novel cerium-dioxide nano-composite coating will be designed to achieve good thermal stability and chemical stability.

The superhydrophobic cerium dioxide nano-composite surfaces were fabricated using two-step processes: synthesis of nano-flower like particles by hydrothermal method and preparation of nano-composite coating. For the cerium dioxide nano-structure synthesis process, 2.17g of cerium (III) nitrate hexahydrate (STREM) and 5.8 g hexamethylenetetramine (Alfa Aesar) were dissolved into 60 mL of DI water. The solution was stirred for 10 minutes at 300 rpm and 60 °C. Then, the solution was sealed into 120 mL fluoropolymer digestion vessel (Savillex, MN, USA) and placed in the hot water bath for 3 hours to 6 hours at 70 °C. The white powder was collected by centrifuge

in DI water for 5 minutes at 4000 rpm speed and repeated for 4 cycles. The cleaned powder was dried in an oven at 60 °C for 12 hours.

The cerium dioxide nano-composite coating was prepared by mixing the dry cerium dioxide nano-particles in polyurethane polymer (MINWAX). The ratio of dry nano-particles and the polymer is about 1:1 and dissolved in 40 mL of acetone. First, the polymer was dissolved into the acetone and placed in the ultrasonic bath for 5 minutes. Then, cerium dioxide nano-particles was added into the polymer solution and placed into the ultrasonic bath for 30 minutes. The nano-composite coating was ready to spray on the clean aluminum alloy surface which was ultrasonically cleaned in acetone solution for 10 minutes. Then, the coating was sprayed on the aluminum alloy surface at 80 °C by airbrush with a 0.3 mm nozzle diameter and 60 psi air pressure.

VII. A. Wetting Behavior of Cerium Dioxide Nano-composite Coating

Figure 43 shows the wetting behavior for the novel superhydrophobic cerium dioxide nano-composite coating. The cerium dioxide nano-composite coating has very good water repellent properties. It has static water contact angle of ~155 degrees and 11.8 degrees of contact angle hysteresis. In addition, the aluminum alloy substrate and the polyurethane polymer coating on aluminum alloy has similar wetting behavior. The aluminum alloy substrate has ~93 degree of static contact angle and ~35 degree contact angle hysteresis. The polyurethane polymer coating on aluminum alloy has ~92 degree of static contact angle and ~36 degree contact angle hysteresis. Therefore, the results

suggest that the cerium dioxide nano-composite coating provides superhydrophobicity at the surface.

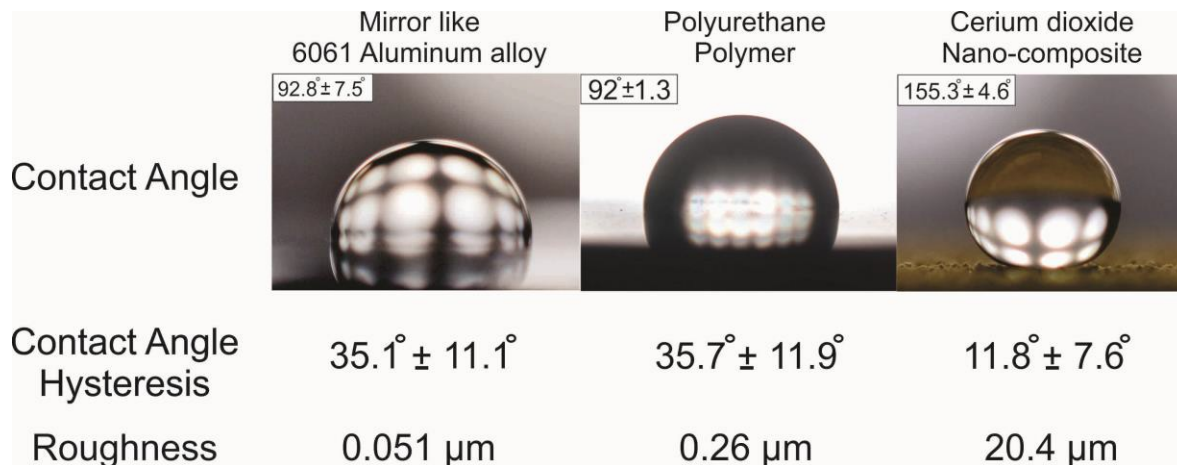


Figure 43. The wetting behavior for the novel superhydrophobic cerium dioxide nano-composite coating: static contact angle, contact angle hysteresis and surface roughness.

VII. A. 1. Surface Roughness and Surface Morphology of Cerium Dioxide Nano-composite Coating

Figure 44a-b show the optical profiler results and surface morphology for the cerium dioxide nano-composite coating. Figure 43 suggests that the superhydrophobicity for the cerium dioxide nano-composite coating is due to the surface roughness. The nano-composite coating has very high surface roughness, which is about 20 m. The mirror like aluminum alloy and the polyurethane polymer coating has very surface which the roughness is 0.051 m and 0.26 m, respectively. Figure 44b shows that the cerium dioxide nano-composite coating forms a flower-like structure at the surface. Cassie-Baxter state possibly occurs on the flower-like micro structure at the surface, so the water droplet will sit on the micro-structure with very high static contact angle. Further

tests will be performed to understand the stability of coating and it includes: boiling test, immersion in acidic test and basic solutions.

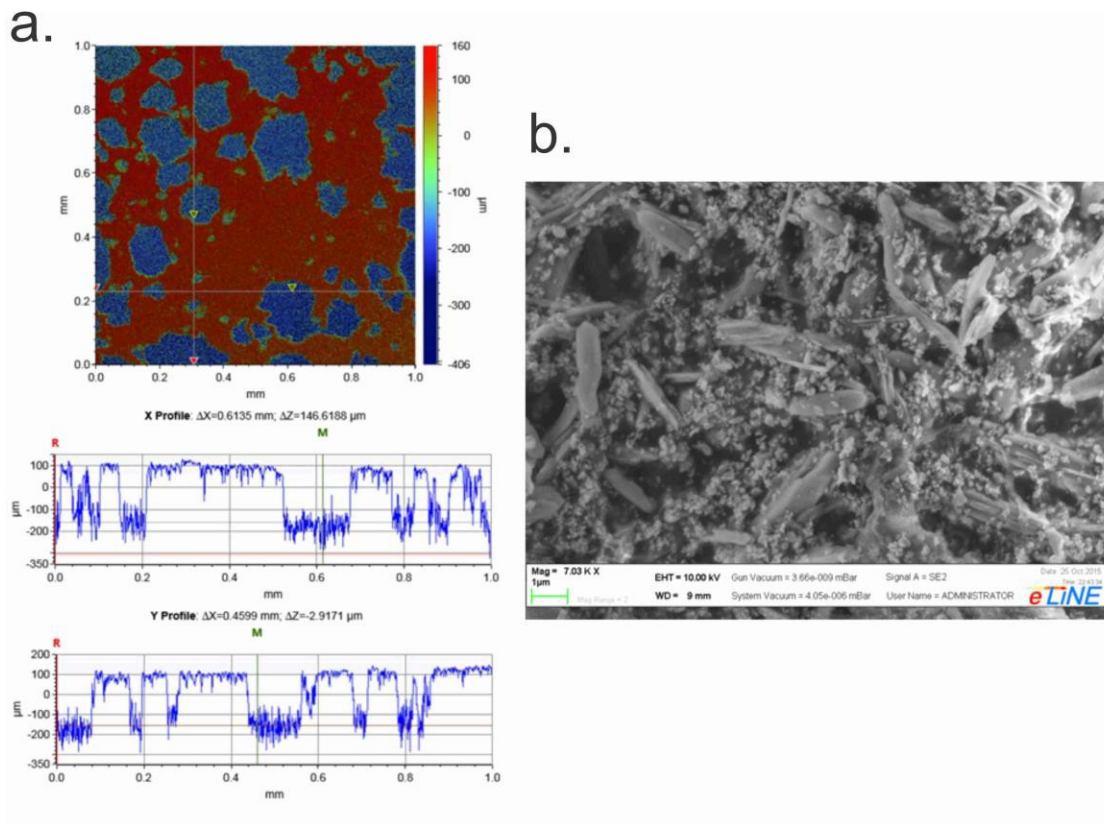


Figure 44. (a) The optical profiler results and (b) surface morphology for the cerium dioxide nano-composite coating.

VII. B. Stability of Cerium Dioxide Nano-composite Coating

The stability of the cerium dioxide nano-composite coating will be determined by boiling test, immersion in acidic basic solutions. The samples will be placed in boiling water for 24 hours. For the immersion in chemicals, the samples will be placed in hydrochloric solution and sodium hydroxide solution for several days.

VII. B. 1. Stability in Boiling Conditions

The new kind of nano-composite water repellent material begins with thermal stability test, 24 hours boiling at 280 °C. The nano-composite coating was sprayed on the flat mirror like 6061 aluminum alloy surface. In figure 45a, the aluminum alloy surface has been oxidized after boiling. For the polymer coating, the polymer coating has been burnt off. For the nano-composite coating, there was no visible damage on the surface, but the color has been changed to deep yellow from a lighter yellow. Figure 45b, shows that the nano-composite coating retains its high static contact angle of ~ 150 degrees after 24 hours of boiling in water at 280 °C, while the contact angle of the aluminum alloy surface decreases to ~ 40 degrees from ~ 95 degrees due to the oxidation on the aluminum alloy surface. Figure 45c shows the contact angle hysteresis on each surface after the boiling experiment. The surface adhesion slightly increases after the boiling for nano-composite coating. The difference is within the range of the measurement error. Therefore, the boiling experiment results shows that the newly discovered nano-composite coating has higher thermal stability than polymer coating, which can protect the aluminum alloy surface to avoid the oxidation.

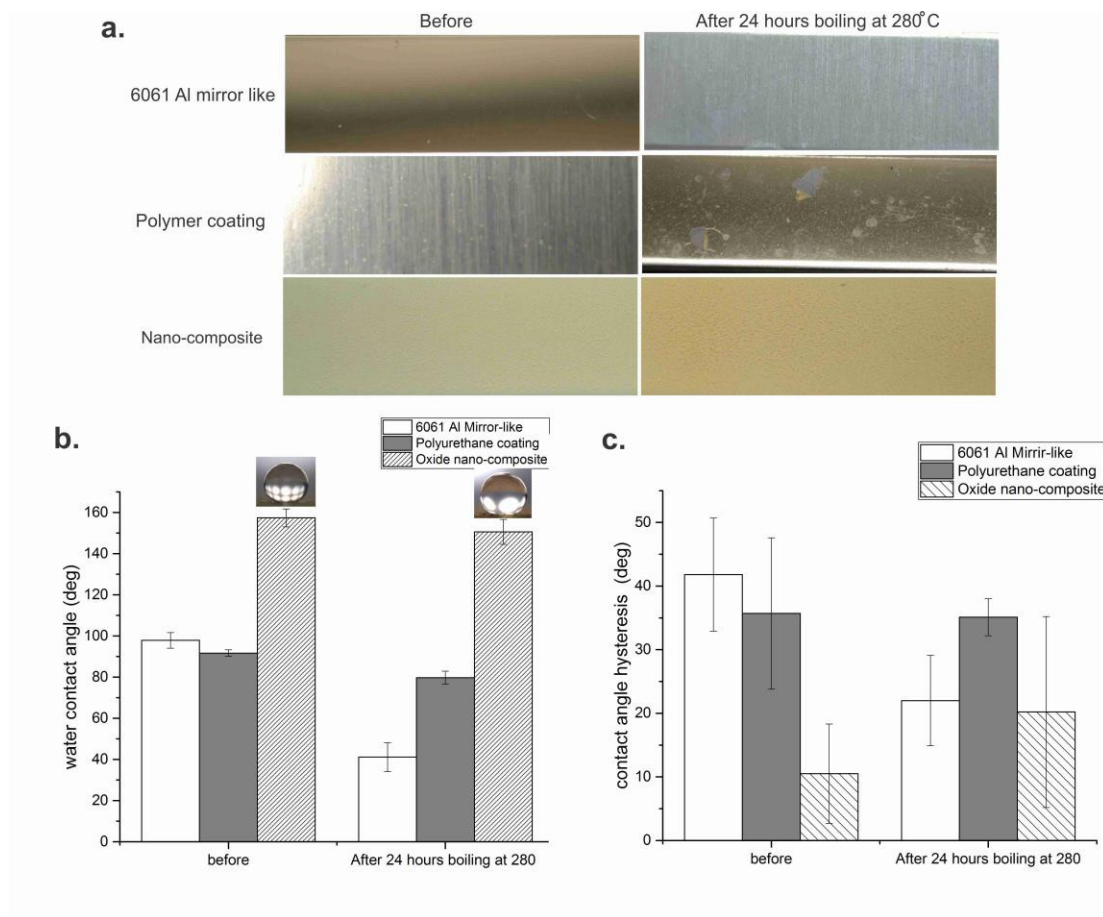


Figure 45. Boiling test results for cerium dioxide nano-composite coating (a) top view of the surface, (b) static contact angle and (c) contact angle hysteresis

VII. B. 2. Chemical Stability in Acidic Conditions

The data in figure 46a-c shows that the novel nano-composite coating also provides protection against corrosion of aluminum surface in acidic environments. Figure 46b-c demonstrates that the nano-composite coating retains its superhydrophobicity after 3 days of immersion in 0.01 M hydrochloric (HCL) solution (~2 pH) with above 150 degrees water static contact angle and ~ 11 degrees of contact angle hysteresis. On the other hand, the contact angle slightly increases after 1 day of immersion in HCL and then reduces to ~ 79 degrees for the surface without coating. Figure 46a suggests that

the increases in contact angle after 1 day of immersion is due to the increase in surface roughness by etching. Therefore, the nano-composite coating and polymer coating can provide surface protection in acidic environments and the nano-composite has good chemical stability.

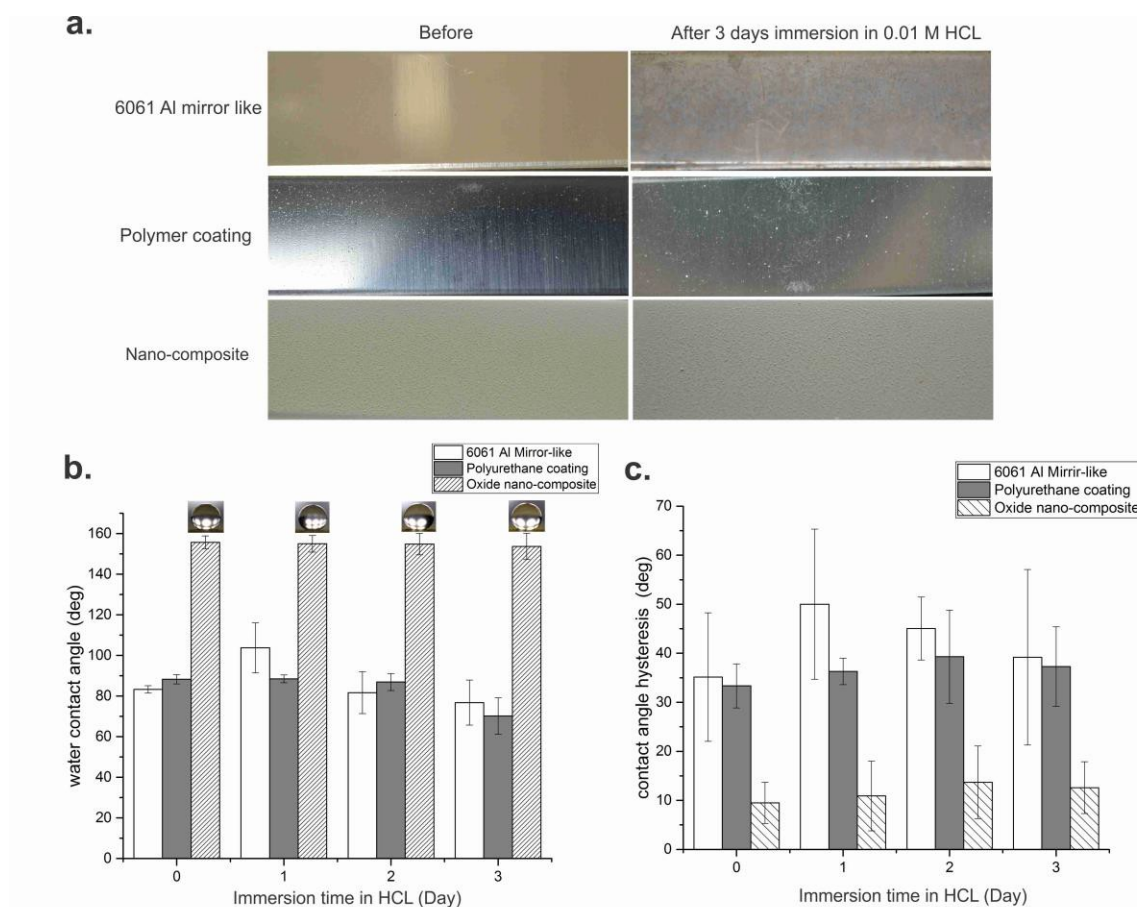


Figure 46. Immersion in acidic test results for cerium dioxide nano-composite coating (a) top view of the surface, (b) static contact angle and (c) contact angle hysteresis

VII. B. 3. Chemical Stability in Base Conditions

The data in figure 47a-c shows that our novel nano-composite coating also provides protection against corrosion of aluminum alloys in basic (high pH) environments. Figure

47a shows that the aluminum alloy surface was damaged by the basic solutions after 1 day of immersion in sodium hydroxide (NaOH). However, the polymer coating and our novel, nano-composite coating can efficiently reduce the corrosion rate on the aluminum alloy surface. Figure 47b-c show the nano-composite coating retains its superhydrophobicity after 3 days of immersion in 0.01 M NaOH solution (~ 13 pH) with static contact angles above ~ 150 degrees contact angle hysteresis of ~ 11 degrees. For the aluminum alloy surface, the hydrophobicity decreases to ~ 10 degree becoming superhydrophilic. Therefore, the immersion test in NaOH shows that the nano-composite coating has good chemical stability in acidic and basic environments.

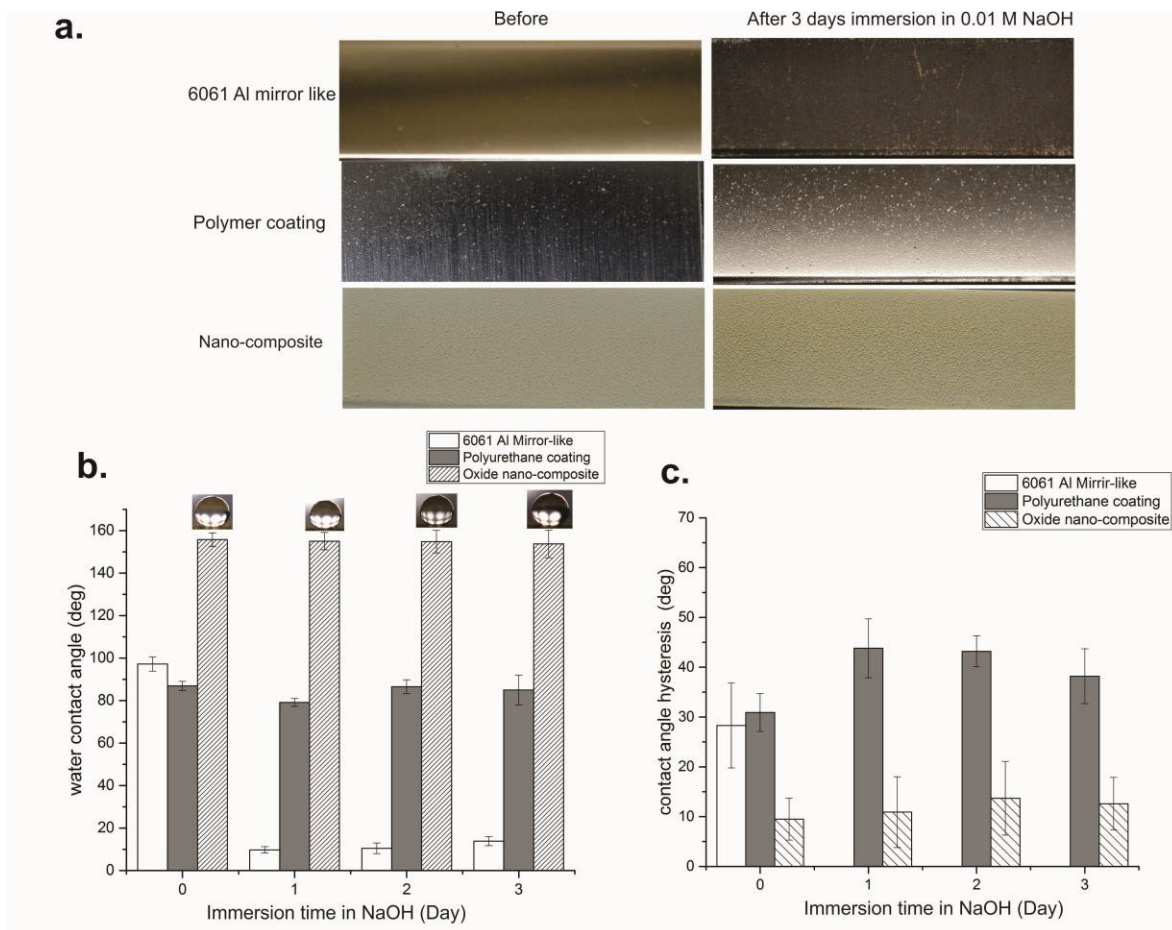


Figure 47. Immersion in base test results for cerium dioxide nano-composite coating (a) top view of the surface, (b) static contact angle and (c) contact angle hysteresis

VII. C. 1. Observation of Water Droplet Bouncing at Room Temperature

Figure 48 shows the bouncing behavior of a novel cerium dioxide nano-composite coating on mirror like aluminum alloy at room temperature. Complete rebounding can be observed after the initial droplet impact. For the flat aluminum surface and polymer coating, deposition can be found because of the smooth surface roughness. In contrast, receding break up and partial rebounding can be observed at the nano-composite surface due to the high surface roughness. These results suggest that the bouncing behavior is also dependent on the surface roughness and surface chemistry.

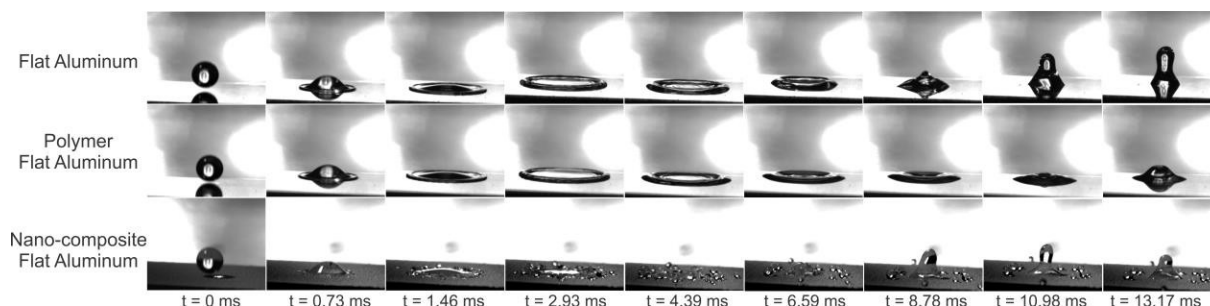


Figure 48. Bouncing behavior of a novel cerium dioxide nano-composite coating on mirror-like aluminum alloy at room temperature

*** Dr Rakesh Prasad Sahu and Dr Alexander Yarin were contributed to the works in this section for the experiment of bouncing behavior at room temperature on superhydrophobic cerium dioxide nano-composite coating on mirror-like aluminum alloy.**

VII. C. 2. Observation of Water Droplet Bouncing at sub-zero Temperature

Figure 49 shows the bouncing behavior of a novel cerium dioxide nano-composite coating on mirror like aluminum alloy at -25°C . The droplets spread out and then began to form ice. Since the cold temperature increases the viscosity of the water droplet, the contact time is increased and the ice more easily formed. For the superhydrophobic cerium dioxide coating, the droplets broke up into many small droplets and then started to form ice. Therefore, the results suggest that the wetting behavior is dependent on the surface temperature and surface roughness.

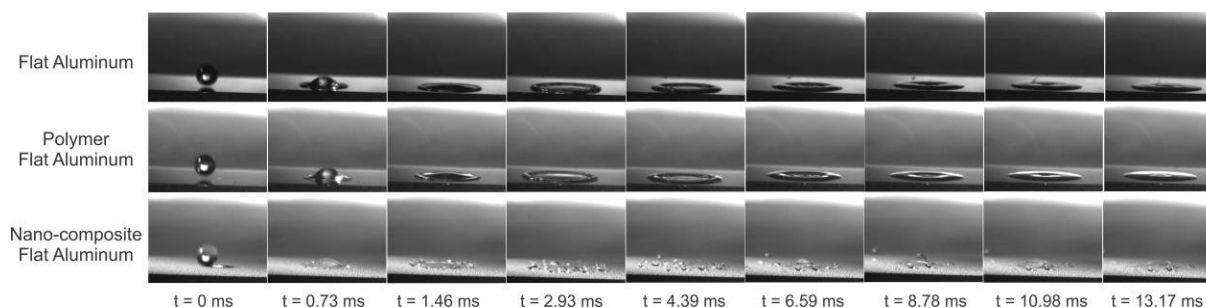


Figure 49. Bouncing behavior of a novel cerium dioxide nano-composite coating on mirror like aluminum alloy at -25 °C.

A novel cerium dioxide nano-composite coating was designed. The nano-composite coating has better stability than polymer coating in boiling test, acidic test and basic test. The superhydrophobicity of the nano-composite coating is due to the high surface roughness from the cerium-dioxide flower-like nano-structure. The surface durability is better than hydrothermal fabrication method, but the durability of the coating needs to be improved for advance applications.

*** Dr Rakesh Prasad Sahu and Dr Alexander Yarin were contributed to the works in this section for the experiment of bouncing behavior at sub-zero temperature on superhydrophobic cerium dioxide nano-composite coating on mirror-like aluminum alloy.**

Chapter VIII: Fabrication of Mechanically Durable Cerium Dioxide Superhydrophobic Surface

The stability of the cerium dioxide nano-composite coating was determined by performing the boiling test, immersion in acidic and basic solutions. The previous test results suggest that the cerium dioxide nano-composite coating provides a good thermal and chemical stability. However, the samples made using the fabrication method described in chapter 7 have low durability. In addition, the coating method is not efficient because it requires a huge amount of nano-particles to form a preferred surface roughness to obtain superhydrophobicity. In this chapter, the cerium dioxide nano-composite coating will be refined to improve the durability and the fabrication efficiency.

Synthesis of cerium dioxide nanoparticles were obtained by using hydrothermal processes. 5.8 g hexamethylenetetramine (Alfa Aesar) and 2.17 g cerium(III) nitrate hexahydrate (STREM) were dissolved into 60 mL of DI water in a beaker and stirred for 10 minutes at 300 rpm in 60 C. The solution was sealed into 120 ml fluoropolymer digestion vessel (Savillex, MN, USA) and placed into hot water bath for 3 hours at 70 C. After three hours, the white powder was collected by centrifuge with DI water for 5 minutes and repeat 4 cycles. The cleaned powder was dried in oven at 60 C for 12 hours.

Preparation of composite nano-structure coating was prepared by mixing 0.15 g of polyurethane (MINWAX) with 20 ml of acetone ultrasonically for 5 minutes. Then, 0.1 g of the cerium dioxide nanoparticles was added to the polymer solution and placed in

ultrasound cleaner for 30 minutes. The coating was sprayed onto the etched aluminum substrate at 80 °C of hot plate temperature by airbrush with 60 psi. 6061 Al mirror like sheet (McMaster-Carr) were cut into 5 cm x 1.5 cm with 2 mm thickness. The Al alloy substrates were etched by being immersed in 4M HCL for 5 minutes at room temperature. Then, the substrate was cleaned by DI water and boiled in hot DI water for 2 hours.

VIII.A. Wetting Behavior of Improved Mechanically Durable Cerium Dioxide Superhydrophobic Surface

Figure 50 shows the wetting behavior for the refined cerium dioxide nano-composite coating on etched aluminum alloy surface. The polyurethane polymer coating on the etched aluminum substrate has a static contact angle of ~124 degrees and ~41.8 degrees of contact angle hysteresis. On the other hand, the refined cerium dioxide nano-composite coating has a ~150 degrees static contact angle and ~ 23 degree contact angle hysteresis.

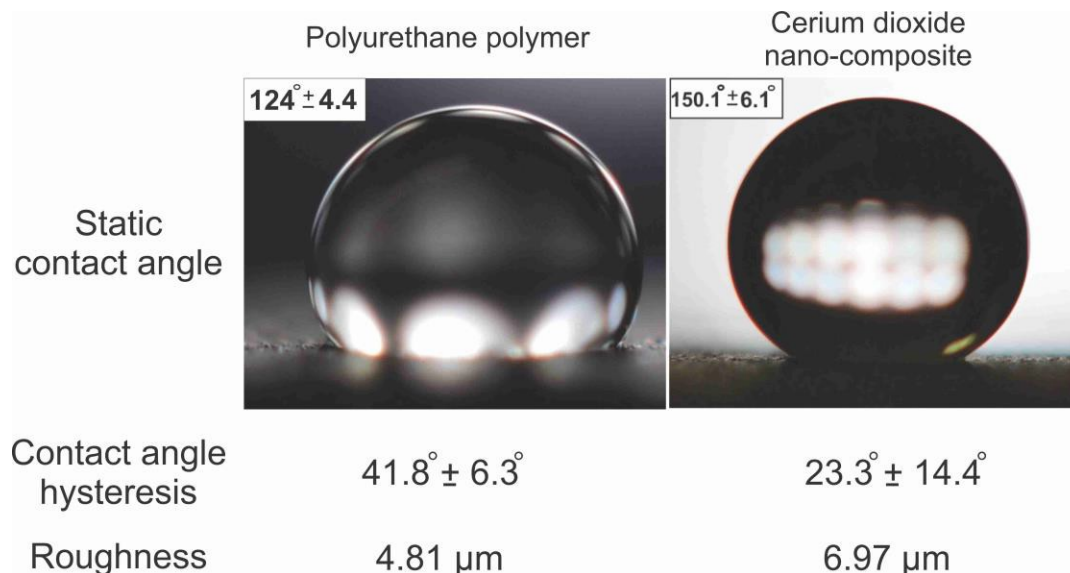


Figure 50. The wetting behavior for the refined cerium dioxide nano-composite superhydrophobic coating on etched aluminum alloy surface: static contact angle, contact angle hysteresis and surface roughness.

VIII. A. 1. Surface Roughness and Surface Morphology

The optical profiler results suggest that the surface roughness is a main factor in the cerium dioxide nano-composite superhydrophobic coating. The polymer coating has a lower surface roughness with 4.81 μm than the nano-composite coating with 6.97 μm surface roughness. In addition, the particle size was determined by transmission electron microscopy (TEM). Figure 51 shows the average particles size is about 6 nm in diameter. The cerium dioxide nano-particles have poly-crystalline structure through the 3 hours of hydrothermal method at 70 $^{\circ}\text{C}$. The hydrophobicity of the surface increases because the nano-composite coating increases the surface roughness.

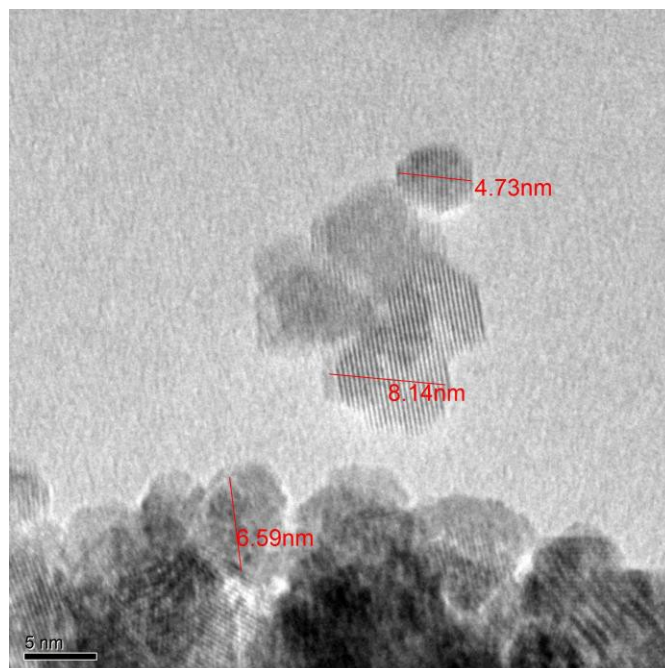


Figure 51. The TEM images for the cerium dioxide nano-particles size

* **Xue Rui** was contributed to the works in this section for measurement of the cerium dioxide nano-particle size.

VIII. A. 2. Observation of Water Droplet Bouncing at Room Temperature

The bouncing experiment was also performed on the etched aluminum alloy samples. Figure 52 shows the bouncing behavior of a novel cerium dioxide nano-composite coating on etched aluminum alloy at room temperature. For the etched aluminum alloy surface, the droplet spread out until reaching to the maximum diameter and then it broke up into many small droplets during the receding stage because of the high surface roughness. The droplets were deposited on the surface due to the high surface adhesion. For the polyurethane coating on etched aluminum samples, the droplets broke up into small droplets during the receding stage, and then started rebounding at the surface.

However, the droplets were partially rebounding at the surface due to the high surface adhesion. For the nano-composite coating, the extended finger is longer than polymer coating after the receding stage because the surface adhesion is smaller on nano-composite coating than polymer coating.

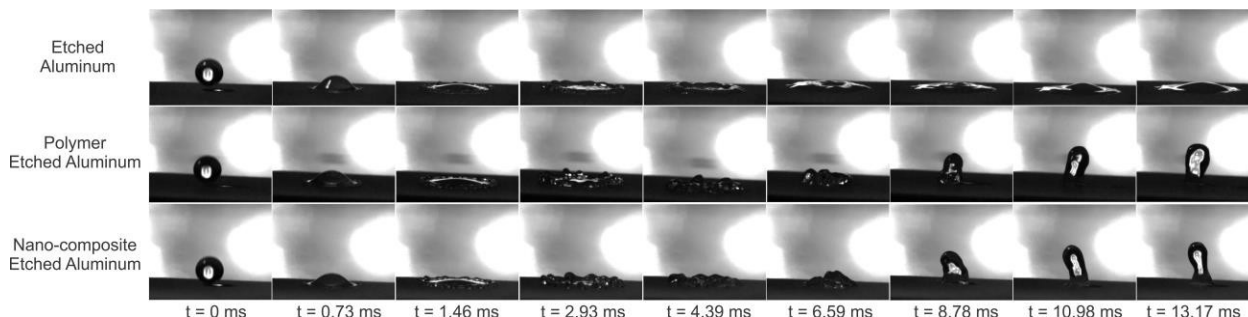


Figure 52. Bouncing behavior of a novel cerium dioxide nano-composite coating on etched aluminum alloy at room temperature

*** Dr Rakesh Prasad Sahu and Dr Alexander Yarin were contributed to the works in this section for the experiment of bouncing behavior at room temperature on superhydrophobic cerium dioxide nano-composite coating on etched aluminum alloy.**

VIII. A. 3.Observation of Water Droplet Bouncing at sub-Zero Temperature

Figure 53 shows the bouncing behavior of a novel cerium dioxide nano-composite coating on etched aluminum alloy at -25°C . The results suggest that the ice starts to form at the edge of lamella at $t = 6.59\text{ ms}$. The observation shows that the low surface temperature reduces the rebounding activity because the viscosity of the droplets is increased by the cold temperature.

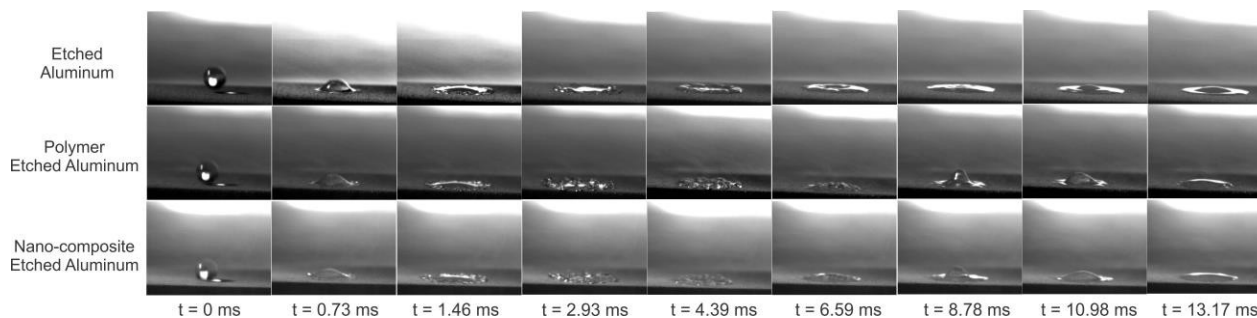


Figure 53. Bouncing behavior of a novel cerium dioxide nano-composite coating on etched aluminum alloy at -25 °C.

*** Dr Rakesh Prasad Sahu and Dr Alexander Yarin were contributed to the works in this section for the experiment of bouncing behavior at sub-zero temperature on superhydrophobic cerium dioxide nano-composite coating on etched aluminum alloy.**

VIII. B. Durability of Cerium Dioxide Nano-composite Coating

The durability of the nano-composite coating on aluminum alloy surface was studied by performing tape tests and the mechanical abrasion test. The peels test was performed by 30 peels of tape. The mechanical abrasion test was performed by scribing a 720 cm abrasion length.

VIII. B. 1. Peels Test

The adhesion of the nano-composite coating on the aluminum alloy surface was studied by performing tape tests. Figure 54a shows the static contact angle after 30 peels of tape and the average static contact angle decreases to 143 degrees from 150 degrees. In addition, the contact angle hysteresis increases after 5 peels of tape as shown in figure

54b. Figure 55 shows the surface roughness and the surface morphology after 30 peels. The surface roughness decreases from 7.38 μm to 6.69 μm after the tape tests. It suggests that the superhydrophobicity is reduced because of the damaged micro-structure at the surface. The SEM images suggest that, the cerium dioxide nano-composite coating has a good adhesion because the cerium dioxide nano-particles can still be observed after 30 peels of tape tests. Therefore, the refined cerium dioxide nano-composite coating has good adhesion and maintains a good static contact angle after the tape tests.

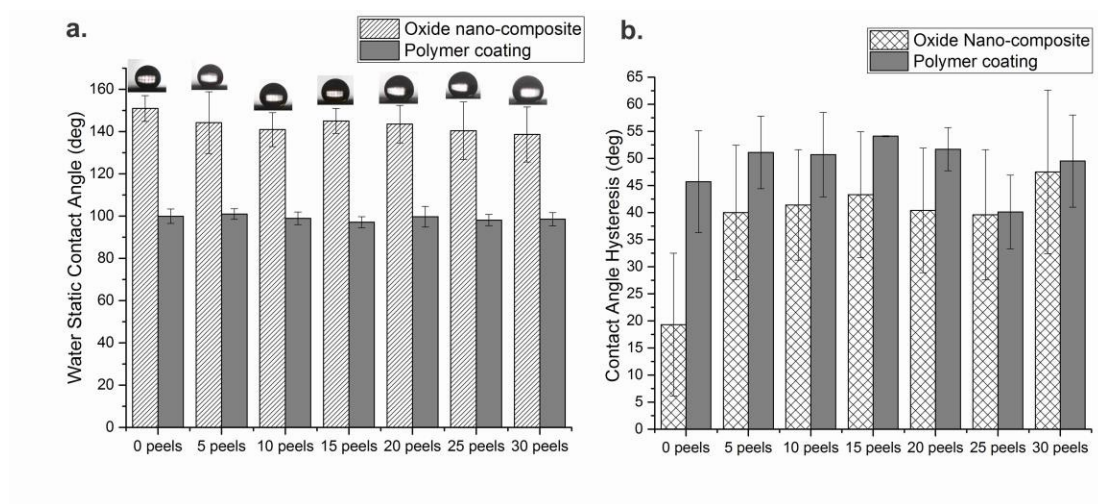


Figure 54. The wetting behavior for the refined cerium dioxide nano-composited coating after the tape test, (a) static contact angle and (b) contact angle hysteresis.

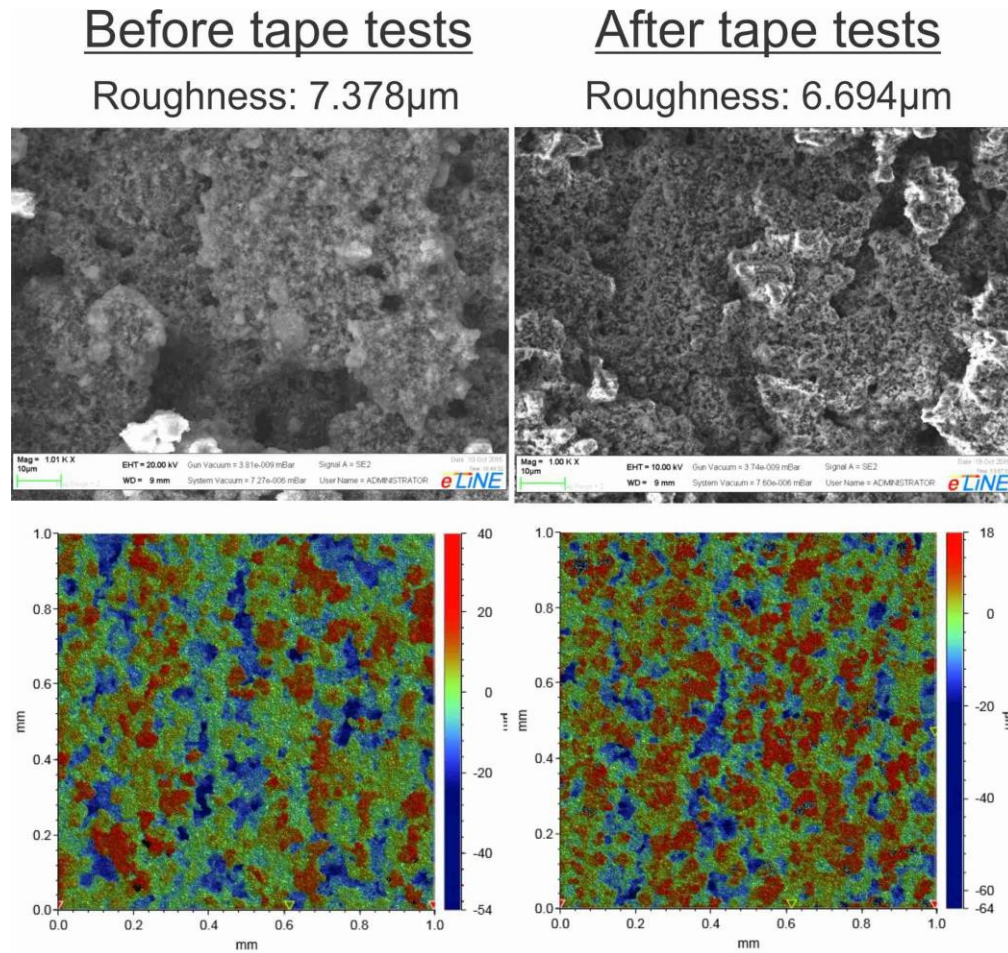


Figure 55. The surface roughness and the surface morphology for the refined cerium dioxide nano-composited coating after the tape test

VIII. B. 2. Abrasion Test

Mechanical abrasion tests were performed by brushing the surface to fully understand the durability of the nano-composite coating,. Figure 56a shows that the static contact angle decreased from ~ 148 degrees to ~ 140 degrees after a 120 cm abrasion length. The final static contact angle is ~ 138 degrees after 720 cm abrasion length. Figure 56b shows the contact angle hysteresis for 720 cm abrasion length. The contact angle hysteresis increases from ~ 21 degrees to ~ 34 degrees after the abrasion test. Figure 57

shows the surface roughness and surface morphology after the abrasion test. The surface structure was slightly damaged by the mechanical abrasion, resulting in a reduction of the surface roughness. The surface roughness decreases from 6.51 μm to 6.13 μm . However, the nano-composite coating has good adhesion to the substrate, which can still provide a good hydrophobicity with very high static contact angle.

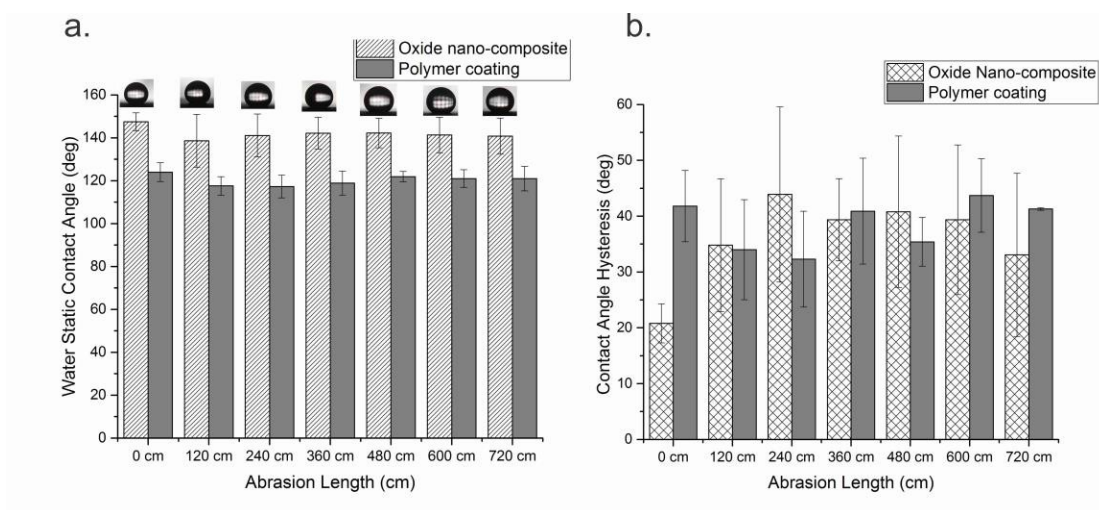


Figure 56. The wetting behavior for the refined cerium dioxide nano-composited coating after the mechanical abrasion test, (a) static contact angle and (b) contact angle hysteresis.

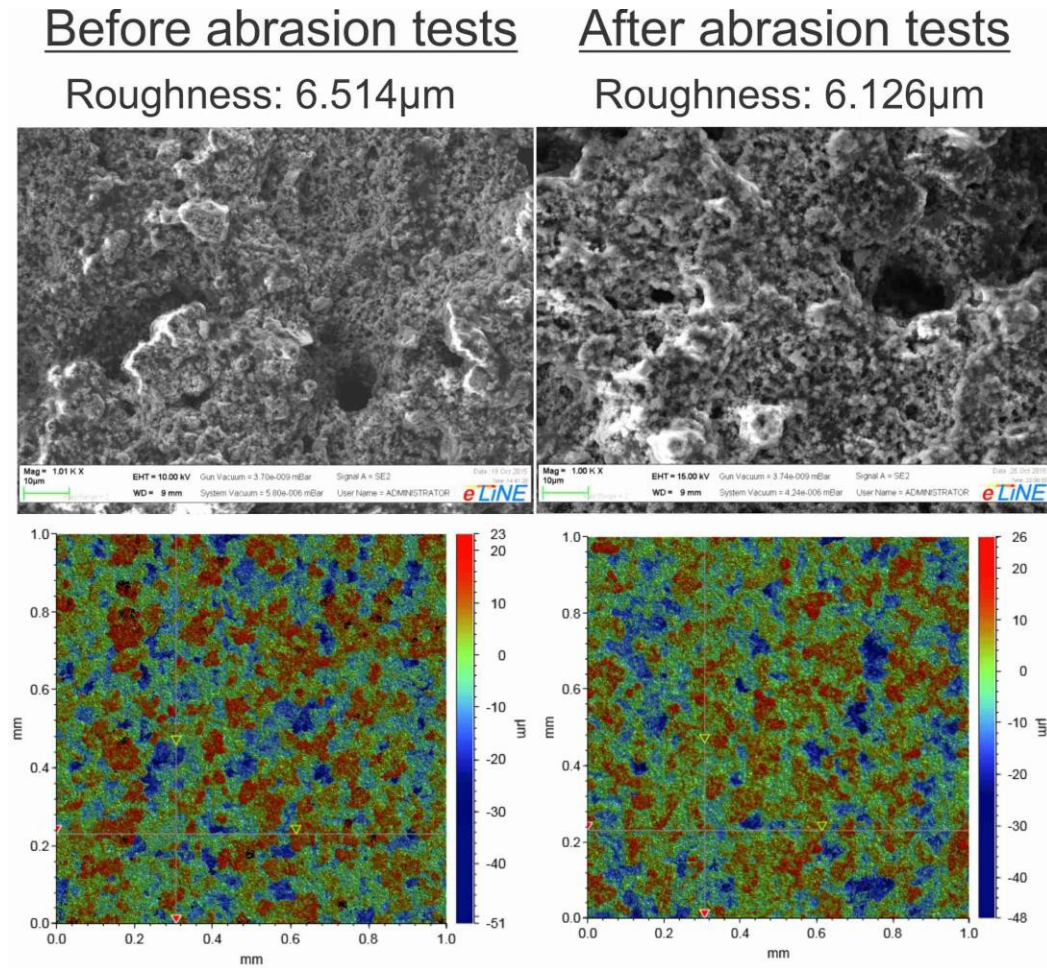


Figure 57. The surface roughness and the surface morphology for the refined cerium dioxide nano-composited coating after the mechanical abrasion test

VIII. B. 3. UV Irradiation Effect

In the previous work, I showed that the hydrophilicity can be induced by UV irradiation.

Figure 58 shows the UV resistance of the superhydrophobic cerium dioxide surface.

After 1 hour exposure of UV irradiation, the static water contact angle is reduced to ~120 degrees from ~150 degrees for the nano-composite coating. For the polymer coating, the contact angle is reduced from ~120 degrees to 95 degrees. The reduced hydrophobicity for nano-composite coating and polymer coating is similar. In this

observation, polyurethane has no UV resistance and hydrophilicity can be induced by UV irradiation.

XPS was used to understand the effect of UV irradiation and the surface chemistry. Figure 59a-c shows the XPS spectra for the cerium dioxide nano-composite coating before and after the UV irradiation treatment. Figure 59a is the survey scan before the UV irradiation treatment for the nano-composite coating. The results suggest that the cerium dioxide nano-particles are completely coated by polyurethane polymer because only carbon and oxygen peaks were observed at the surface. For the C 1s spectra, figure 59b, the hydrocarbon peak (~ 284.6 eV) decreases after the 1 hour of exposure in UV irradiation. For the O 1s spectra, figure 59c, the results have no changes after the UV irradiation treatment. Therefore, the hydrophobicity decreases because the hydrocarbon species decrease at the surface.

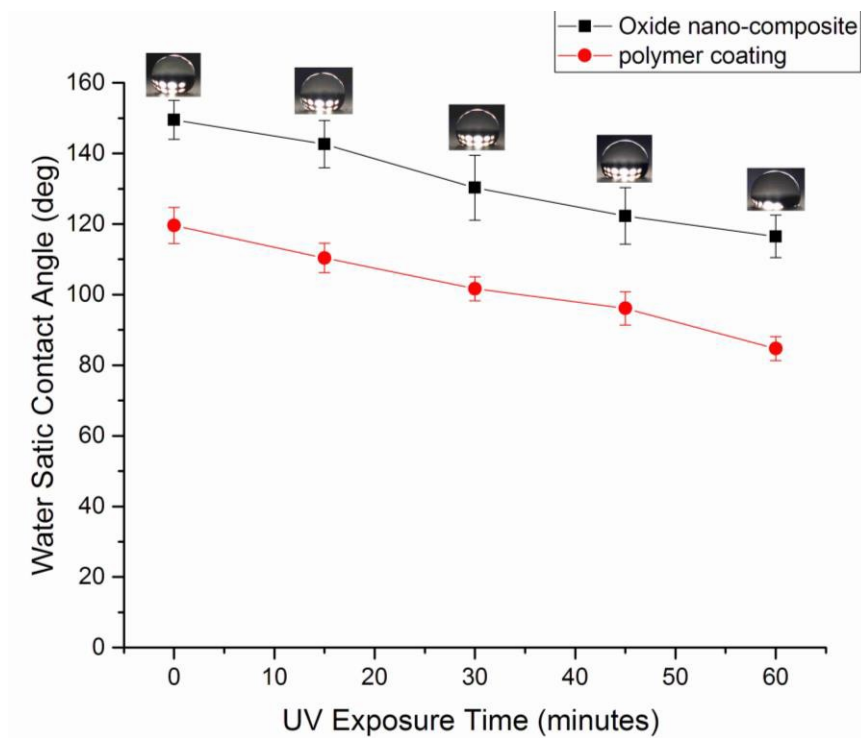


Figure 58. The UV irradiation in wetting behavior of refined cerium dioxide nano-composite coating

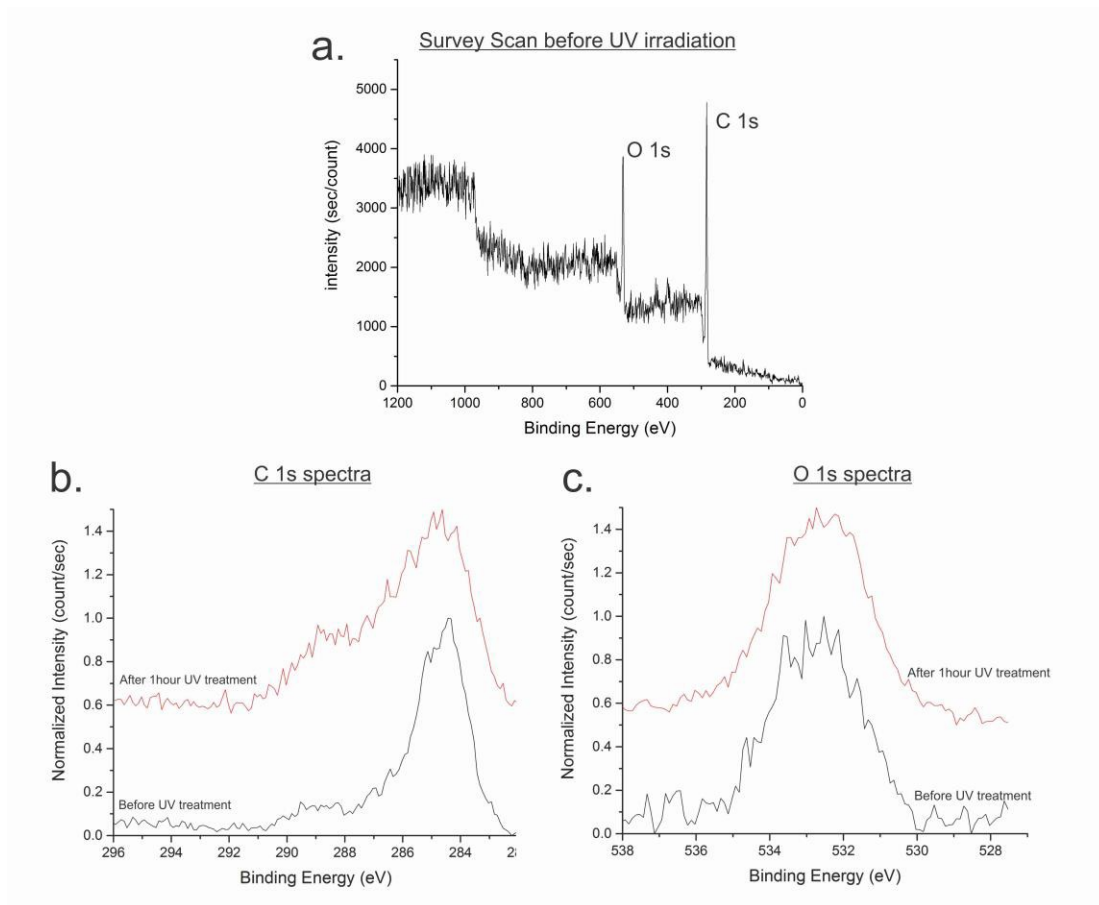


Figure 59. XPS analysis of UV irradiation for refined cerium dioxide nano-composite coating, (a) survey scan before UV irradiation, (b) C 1s spectra and (c) O 1s spectra.

The refined cerium dioxide nano-composite coating has better durability than the coatings prepared by hydrothermal method and the original design. In addition, this refined fabrication method is able to use a smaller amount of nano-particles to provide superhydrophobicity compared with the original design. However, this novel cerium dioxide nano-composite coating still needs to be modified to achieve higher durability, water repellency and UV resistance.

IX. Summary, Conclusion and Ongoing Work

In this report, the wetting behavior of cerium dioxide has been studied by pulsed laser deposition method. The results suggest that the hydrophobicity of the cerium dioxide is induced by hydrocarbon species at the surface. The cerium dioxide surface becomes more hydrophobic if the surface has a higher concentration of hydrocarbon species. In chapter 5, the wetting behavior for the mixed oxides thin films (Ti-doped CeO_2) has been studied. I found that the electronegativity of the metal and oxygen atoms controls the wetting behavior at the oxide surface. Larger electronegativity of the oxide material provides larger hydrophobicity because the ions more readily react with ambient air to form OH- group, which works as a trigger to adsorb more hydrocarbon species at the surface. The susceptibility to UV irradiation activity can be reduced by adding a small amount of cerium ions. The Ce (III) anions at the Ti doped CeO_2 surface can capture the holes to transform to stable Ce(IV) that prevents the photogenerated electrons and holes at the surface.

The cerium dioxide superhydrophobic surface has been fabricated by hydrothermal method. The cerium dioxide flower-like nano-particles become superhydrophobic after the stearic acid treatment with ~ 160 degree static contact angle. The results suggest that cerium dioxide can be used to form superhydrophobic surfaces, but this method has very poor durability, thermal stability and chemical stability. A novel cerium dioxide nano-composite coating was innovated. This nano-composite coating provides good thermal stability and chemical stability to avoid oxidation on the aluminum alloy surface. Finally, the durability of the cerium dioxide nano-composite coating can be increased by etching

the aluminum alloy surface prior to coating. The testing results show that the nano-composite coating has good adhesion to the aluminum alloy surface.

The bouncing experiment shows that superhydrophobic cerium dioxide coating after stearic acid treatment has very good water repellency. Surface roughness and surface chemistry can affect the water bouncing behavior at the surface. Receding break-up can be observed on the rough surface. The bouncing experiment results suggest that the surface temperature also is a main factor, which can control the anti-icing property. Low surface temperature increases the viscosity of the water droplets, so the bouncing water droplets have lower rebounding activity at the cold surface. Therefore, cold temperature will reduce the anti-icing behavior.

In the future, a new polymer will be innovated to improve the adhesion and the durability. This new polymer needs to be UV resistant and low cost. In addition, the icing behavior on the superhydrophobic surface needs to be studied because superhydrophobicity often does not result in “ice-phobicity”. Frost can be formed at the surface and it can increase the hydrophilicity at the surface. It is very important to create a real anti-icing surface with high durability.

REFERENCES:

- ¹ Koji Tsukuma; Masahiko Shimada. *Strength, Fracture Toughness and Vickers Hardness of CeO² Stabilized Tetragonal ZrO² Polycrystals*. *Journal of Materials Science*. 1985, Vol. 20 (4), 1178-1184.
- ² H. J Beie; A. Gnorich. *Oxygen Gas Sensor Based on CeO² Thick and Thin Film*. *Sensors and Actuators B: Chemical*. 1991, Vol. 4 (3-4), 393-399.
- ³ Venu Mangam; Sumit Bhattacharya; Karabi Das; Siddhartha Das. *Friction and Wear Behavior of Cu-CeO² Nanocomposite Coating*. *Surface and Coatings Technology*. 2010, Vol. 205 (3), 801-805.
- ⁴ M. A. Henderson; C.L. Perkins; M.H. Engelhard; S. Thevuthasan; C. H. F. Peden, *Redox Properties of Water on the Oxidized and reduced surface of CeO₂ (111)*, 2003, Vol. 526, 1-18.
- ⁵ G. Balakrishnan; S. Tripura Sundari; P. Kuppasami; P. Chandra Mohan; M. P. Srinivassan; E. Mohandas; V. Ganesan; D. Sastikumar. *A Study of Microstructural and Optical Properties of Nano-crystalline Ceria Thin Film Prepared by PLD*. *Thin Solid Films*. 2011, Vol. 519 (8), 2520-2526.
- ⁶ B. Elidrissi; M. Addou; M. Regragui; C. Monty; A. Kachouane. *Structure and Optical Properties of CeO² Thin Film Prepare by Spray Pyrolysis*. *Thin Solid Films*. 2000, Vol. 379 (1-2), 23-27.
- ⁷ Gisele Azimi; Rajeev Dhiman; Hyuk-Min Kwon; Adam T. Paxson; Kripa K. Varanasi. *Hydrophobicity of Rare Earth Oxide Ceramics*. *Nature Materials*. 2013, Vol. 12, 315-320.
- ⁸ Santiago Romero-Vargas Castrillon; Nicolas Giovabattista; Ihan A. Aksay; Pablo B. Debenedetti. *Effect of Surface Polarity on Water*. *J. Phys. Chem*. 2009, Vol. 113 (5), 1438-1446.
- ⁹ Liang-Shu Zhong; Jin-Song Hu; An-Min Cao; Qiang Liu; Wei-Guo Song; Li-Jun Wan. *3D-Flowerlike Ceria Micro/Nano Composite Structure and Its Application for Water Treatment and CO Removal*. *Chem. Mater*. 2007, 19 (7), 1648-1655.
- ¹⁰ Gary Jacobs; Emilie Chenu, Patricia M. Patterson; Leann Williams; Dennis Sparks; Gerald Thomas; Burtron H. Davis. *Water-Gas Shift Comparative Screening of Metal Promoters for Metal Ceria System and Role of the Metal*. *Applied Catalysis A: General*. 2004, Vol. 258 (2), 203-214.
- ¹¹ M.F. Mmontemor; R. Pinto; M. G. S. Ferreira. *Chemical Composition and Corrosion Protection of Silane Films Modified with CeO² Nanoparticles*, *Electrochimica Acta*. 2009, Vol. 54 (22), 5179-5189.

- ¹² Yang Zhou; Xu Xiao-Liang; Gong Mao Gang; Liu Ling; Liu Yang Song, *Wettability and Formation Mechanism of ZnO Micro-Spheres Composed Film*, *Chin. Phys. B*, 2010, Vol. 19 (12).
- ¹³ M. Thieme; F. Streller; F. Simon; R. Frenzel; A.J. White, *Superhydrophobic Aluminium-Based Surfaces: Wetting and Wear Properties of Different CVD-Generated Coating Types*, *Applied Surface Science*, 2013, Vol. 283, 1041-1050.
- ¹⁴ Manas K. Sarkar; Kausik Bal; Fuen He; Jintu Fan, *Design of an Outstanding Superhydrophobic Surface by Electro-spinning*, *Applied Surface Science*, 2011, Vol. 257, 7003-7009.
- ¹⁵ Lingfei Hong; Tingrui Pan, *Surface Microfluidics Fabricated by Photopatternable Superhydrophobic Nanocomposite*, *Microfluid Nanofluid*, 2011, Vol.10, 991-997.
- ¹⁶ Stijn van Pelt; Arjan Frijns; Rajesh Mandamparambil; Jaap den Toonder, *Local Wettability Tuning with Laser Ablation Redeposits on PDMS*, *Applied Surface Science*, 2014, Vol. 303, 456-464.
- ¹⁷ Tolga Aytug; Daniela F Bogorin; Parans M Paranthaman; John E Mathis; John T Simpson; David K Christen, *Superhydrophobic Ceramic Coatings Enabled by Phase-separated Nanostructured Composite TiO_2 – Cu_2O thin films*, *Nanotechnology*, 2014, Vol. 25.
- ¹⁸ Checco A; Ocko BM; Rahman A; Black CT; Tasinkevych M; Giacomello A; Dietrich S, *Collapse and Reversibility of the Superhydrophobic State on Nanotextured Surfaces*, *PhysRevLett*. 2014, Vol 111.
- ¹⁹ Qian BT; Shen ZQ, *Fabrication of Superhydrophobic surfaces by Dislocation-selective Chemical Etching on Aluminum, Copper and Zinc Substrates*, *Langmuir*, 2005, Vol. 21, 9007 -9009.
- ²⁰ Qian Feng Xu; Yang Liu; Fang-Ju Lin; Bikash Mondal; Alan M. Lyons, *Superhydrophobic TiO_2 -Polymer Nanocomposite Surface with UV-Induced Reversible Wettability and Self-Cleaning Properties*, *ACS Appl. Mater. Interfaces*. 2013, Vol. 5, 8915-8924.
- ²¹ Yong Chae Jung; Bharat Bhushan, *Dynamic Effects of Bouncing Water Droplets on Superhydrophobic Surfaces*, *Langmuir*. 2008, Vol. 24, 6262-6269.
- ²² Daniel Ebert; Bharat Bhushan, *Wear-resistant Rose Petal-Effect Surface with Superhydrophobicity and High Droplet Adhesion using Hydrophobic and Hydrophilic Nanoparticles*, *Journal of Colloid and Interface Science*, 2012, Vol. 384, 182-188.

- ²³ Yongmei Zheng; Xuefeng Gao; Lei Jiang, *Directional Adhesion of Superhydrophobic Butterfly Wings*, *Soft Matter*. 2007, Vol. 3, 178-182.
- ²⁴ N.B. Vargaftik; B.N. Volkov; L.D. Voljak, *International Tables of the Surface Tension of Water*, *J. Phys. Chem. Ref. Data*, 1983, Vol. 12.
- ²⁵ Aurelie Lafuma; David Quere, *Superhydrophobic states*, *Nature Materials*, 2003, Vol.2.
- ²⁶ J. Bico; C. Marzolin; D. Quere, *Pearl Drops*, *Europhys. Lett.*, 1999, Vol. 2, 220-226.
- ²⁷ M.Nosonovsky; B. Bhushan, *Hierarchical Roughness Optimization for Biomimetic Superhydrophobic Surface*, *Ultramicroscopy*, 2007, Vol. 107, 969-979.
- ²⁸ B. Bhushan; Y.C. Jung, *Natural and Biomimetic Artificial Surfaces for Superhydrophobicity Self-Cleaning Low Adhesion and Drag Reduction*, *Progress in Materials Science*, 2011, Vol. 56, 1-108.
- ²⁹ Subhayu Basu; Mukul M. Sharma, *Measurement of Critical Disjoining Pressure for Dewetting of Solid Surfaces*, *Journal of Colloid and Interface science*, 1996, Vol. 181, 443-455.
- ³⁰ Mikell P. Groover, *Fundamentals of Modern Manufacturing 4th*, Wiley, New York, 2010
- ³¹ Satoshi Takeda; Makoto Fukawa; Yasuo Hayashi; Kiyoshi Matsumoto, *Surface OH group Governing Adsorption Properties of Metal Oxide Films*, *Thin Solid Films*, 1999, Vol. 339, 220-224.
- ³² Koji Tsukuma; Masahiko Shimada, *Strength, Fracture Toughness and Vickers Hardness of CeO₂ Stabilized Tetragonal ZrO₂ Polycrystals*, *Journal of Materials Science*, 1985, Vol. 20 (4), 1178-1184.
- ³³ H.J Beie; A. Gnorich, *Oxygen Gas Sensor Based on CeO₂ Thick and Thin Film*, *Sensors and Actuator B: Chemical*, 1991, Vol. 4 (3-4), 393-399.
- ³⁴ Venu Mangam; Sumit Bhattacharya; Karabi Bas; Siddhartha Das, *Friction and Wear Behavior of Cu-CeO₂ Nanocomposite Coating*, *Surface and Coatings Technology*. 2010, Vol. 205 (3), 801-805.
- ³⁵ M.F. Stroosnijder; V. Buttmann; T. Fransen; J.H. W. de Wit, *Corrosion of Alloy 800H and the Effect of Surface Applied CeO₂ in a Sulfidizing Oxidizing Carburizing Environment at 700 degree C*, *Oxidation of Metals*, 1990, Vol. 33(5), 371-397.
- ³⁶ B. Elidrissi; M. Addou; M. Regragui; C. Monty; A. Kachouane, *Structure and Optical Properties of CeO₂ Thin Film Prepare by Spray Pyrolysis*, *Thin Solid Films*, 2000, Vol. 379 (1-2), 23-27.

- ³⁷ G. Balakrishnan; S. Tripura Sundari; P. Kuppasami; P. Chandra Mohan; M. P. Srinivassan; E. Mohandas; V. Ganesan; D. Sastikumar, *A Study of Microstructural and Optical Properties of Nano-Crystalline Ceria Thin Film Prepared by PLD*, *Thin Solid Films*, 2011, Vol. 519 (8), 2520-2526.
- ³⁸ Friedrich Esch; Stefano Fabris; Ling Zhou; Tiziano Montini; Cristina Africh; Paolo Fornasiero; Giovanni Comelli; Renzo Rosei, *Electron Localization Determines Defect Formation on Ceria Substrates*, *Science*, 2005, Vol. 309, 752-755.
- ³⁹ D.R Mullins; S.H Overbury; D.R Huntley, *Electron Spectroscopy of Single Crystal and Polycrystalline Cerium Oxide Surfaces*, *Surface Science*, 1998, Vol. 409 (2), 307-319.
- ⁴⁰ G Praline; B D Koel; R L Hance; H Lee; J M White, *X-ray Photoelectron Study of the Reaction of Oxygen with Cerium*, *Journal of Electron Spectroscopy and Related Phenomena*, 1980, Vol. 21, 17-30.
- ⁴¹ A. Laachir; V. Perrichon; A. Badri; J. Lamotte; E. Catherine; J C Lavalley; J. El Fallah; L. Hilaire; F le Normand; E. Quemere; G. N Sauvion; O. Touret, *Reduction of CeO₂ by Hydrogen*, *J. Chem. Soc. Faraday Trans*, 1991, Vol. 87 (10), 1601-1609.
- ⁴² Milena Stepien; Jarko J. Saarinen; Hannu Teisala; Mikko Tuominen; Mikko Aromaa; Jurkka Kuusipalo; Jyrki M. Makela; Martti Toivakka; *Surface Chemical Analysis of Photocatalytic Wettability Conversion of TiO₂ Nanoparticle Coating*, *Surface & Coatings Technology*, 2012, Vol. 208, 73-79.
- ⁴³ Huan Liu; Lin Feng; Jin Zhai; Lei Jiang; Daoben Zhu, *Reversible Wettability of a Chemical Vapor Deposition Prepared ZnO Film between Superhydrophobicity and Superhydrophilicity*, *Langmuir*, 2004, Vol. 20, 5659-5661.
- ⁴⁴ Gargi Dutta; Srijan Kumar Saha; Umesh V. Waghmare, *Effects of Zr and Ti doping on the Dielectric Response of CeO₂: A Comparative First-Principles Study*, *Solid State Communications*, 2010, Vol. 150, 2020-2022.
- ⁴⁵ D.R. Mullins; S.H. Overbury; D.R. Huntley, *Electron Spectroscopy of Single Crystal and Polycrystalline Cerium Oxide Surface*, *Surface Science*, 1998, Vol. 409, 307-319.
- ⁴⁶ A. Pfau; K.D. Schierbaum, *The Electronic Structure of Stoichiometric and Reduced CeO₂ Surface: an XPS, UPS and HREELS Study*, *Surface Science*, 1994, Vol. 321, 71-80.
- ⁴⁷ Huan Liu; Lin Feng; Jin Zhai; Lei Jiang; Daoben Zhu, *Reversible Wettability of a Chemical Vapor Deposition Prepared ZnO Film between Superhydrophobicity and Superhydrophilicity*, *Langmuir*, 2004, Vol. 20, 5659-5661.
- ⁴⁸ Gudrun Petzold; Simona Schwarz; Victoria Dutschk, *Polyelectrolyte-surfactant complexes and their influence on the wettability of different polymer surfaces*, *Colloid Polym Sci*, 2014, Vol. 292, 2197-2205.

- ⁴⁹ B.B. Patil; S.H. Pawar. *Structural, Morphological and Electrical Properties of Spray Deposited Nano-crystalline CeO₂ Thin Film*. *Journal of Alloy and Compounds*. 2011, Vol. 509 (2), 414-420.
- ⁵⁰ Mansour S. Al-Robaee; K. Narasimha Rao; S. Mohan. *Influence of Substrate Temperature on the Properties of Oxygen-Ion Assisted Deposited CeO₂ Film*. *Appl. Phys.* 1992, Vol. 71, 2380.
- ⁵¹ N. Guillou; L.C. Nistor; H. Fuess; H. Hahn. *Microstructural Studies of Nanocrystalline CeO₂ produced by Gas Condensation*. *Nanostructured Materials*. 1997, Vol. 8 (5), 545-557.
- ⁵² Naoki Wakiya; Makoto Yoshida; Takanori Kiguchi; Kazuo Shinozaki; Nobuyasu Mizutani. *RF-Magnetron Sputtered Heteroepitaxial YSZ and CeO₂/YSZ/Si (001) thin films with Improved Capacitance Voltage Characteristics*. *Thin Solid Films*. 2002, Vol. 411 (2), 268-273.
- ⁵³ D. Barreca; A. Gasparotto; E. Tondello; C. Sada; S. Polizzi; A. Benedetti. *Nucleation and Growth of Nanophasic CeO₂ Thin Films by Plasma-Enhanced CVD*. *Chemical Vapor Deposition*. 2003, Vol. 9 (4), 199-206
- ⁵⁴ M. Schem; T. Schmidt; J. Gerwahn; M. Wittmar M. Veith; G.E. Tompson; I.S. Molchan; T. Hashimoto; P. Skeldon; A. R. Phani; S. Santucci; M. L. Zheludkevich. *CeO₂ Filled Sol-Gel Coating for Corrosion Protection of AA2024-T3 Aluminum Alloy*. *Corrosion Science*. 2009, Vol. 51 (10), 2304-2315.
- ⁵⁵ Ming Wei; Dan Zhi; Kwang-Leong Choy. *Electrostatic Spray Assisted Vapour Deposition and Structural Characterization of Cerium Oxide Films on Biaxially Textured Ni Tapes*. *Materials Letters*. 2006, Vol. 60 (12), 1519-1523.
- ⁵⁶ J.F. Moulder; W.F. Stickle; P.E. Sobol; K.D. Bomben; G.E. Muilenberg, *Handbook of X-Ray Photoelectron Spectroscopy*, 2nd edition Perkin-elmer, Eden Prairie, 1992
- ⁵⁷ Faical Larachi; Jerome Pierre; Alain Adnot; Alain Bernis. *Ce_{3d} XPS Study of Composite CexMn1-xO2-y wet oxidation catalyst*. *Applied Surface Science*. 2002, Vol. 195 (1-4), 236-250.
- ⁵⁸ Ahmidou Laachir; Vincent Perrichon; Ahmed Badri; Jean Lamotte; Eugene Catherine; Jean Claude; Jaafar El Fallah; Lionel Hilaire; Francois Le Normand; Eric Quemere; Guy Noel Sauvion; O. Touret, *Reduction of CeO₂ by Hydrogen*, *J. Chem. Soc. Faraday Trans*, 1991 Vol 87 (10), 1601-1609.
- ⁵⁹ Michael Rieutord, *Fluid Dynamics: An Introduction*, Springer, France, 2015, p. 212
- ⁶⁰ J. Kaspar; P. Fornasiero; M. Graziani, *User of CeO₂-based oxides in the three-way catalysis*, *Catalysis Today*, 1999, Vol. 50, 285-298.

- ⁶¹ Rong Wang; Nobuyuki Sakai; Akira Fujishima; Toshiya Watanabe; Kazuhito Hashimoto, *Studies of Surface Wettability Conversion on TiO₂ Single-Crystal Surfaces*, *J. Phys. Chem. B*, 1999, Vol. 103, 2188-2194.
- ⁶² E. Perry Murray; T. Tsai; S. A. Barnett, *A direct-methane Fuel Cell with a Ceria-based Anode*, *Nature*, 1999, Vol. 400, 649-651.
- ⁶³ Vaibhaw Kumar; Jeffrey R. Errington, *Impact of Small-Scale Geometric Roughness on Wetting Behavior*, *Langmuir*, 2013, Vol 20, 11815-11820.
- ⁶⁴ Yang Wang; Xiangdong Wang; Zhongjie Du; Chen Zhang; Ming Tian; Jianguo Mi, *Evaluation of Macroscale Wetting Equations on a Microrough Surface*, *Langmuir*, 2015, Vol. 31, 2342-2350.
- ⁶⁵ Grzelak E. M; Errington J. R. *Nanoscale limit to the applicability of Wenzel's equation*, *Langmuir*, 2010, Vol. 26, 13297-13304.
- ⁶⁶ Frederic Leroy; Florian Muller-Plathe, *Can Continuum Thermodynamics Characterize Wenzel Wetting States of Water at the Nanometer Scale?*, *J. Chem. Theory Comput.*, 2012, Vol.8, 3724-3732.
- ⁶⁷ Hari Acharya; Nicholas J. Mozdierz; Pawel Keblinski; Shekhar Garde, *How Chemistry, Nanoscale Roughness, and the Direction of Heat Flow Affect Thermal Conductance of Solid-Water Interfaces*, *Ind. Eng. Chem. Res.*, 2012, Vol. 51, 1767-1773.
- ⁶⁸ Daniel J. Preston; Nenad Miljkovic; Jean Sack; Ryan Enright; John Queeney; Evelyn N. Wang, *Effect of Hydrocarbon Adsorption on the Wettability of rare earth oxide ceramics*, *Applied Physics Letters*, 2014, 105 (1)
- ⁶⁹ Sami Khan; Gisele Azimi; Bilge Yildiz; Kripa K. Varanasi, *Role of Surface Oxygen to Metal Ratio on the Wettability of Rare-Earth Oxides*, *Applied Physics Letters*, 2015, 106
- ⁷⁰ Celestini F; Kofman R. *Vibration of submillimeter-size supported droplet*, *Phys Rev E*, 2006, 73:041602
- ⁷¹ Jung YC; Bhushan B, *Dyanmic effects induced transition of droplets on biomimetic superhydrophobic surfaces*, *Langmuir*, 2009, Vol.25, 9208-9218.
- ⁷² Yarin A.L, *Drop Impact Dynamics: Splashing, Spreading, Receding, Bouncing...*, *Annu. Rev. Fluid Mech*, 2006, Vol. 38, 159-192.
- ⁷³ Mark David Fisher; Michael Kang-Jen Lee; Randall Gene Schmidt; Shengqing Xu, *"Metal Thermal Stabilization of Polydiethylsiloxane and Copolymers thereof."* Patent WO 2014160112 A1, 2 October 2014.

- ⁷⁴ Bhushan B; Jung YC; Koch K., *Self-cleaning Efficiency of Artificial Superhydrophobic Surface*, *Langmuir*, 2009, Vol. 25, 3240-9.
- ⁷⁵ Vakarelski, I. U., Patankar, N. A., Marston, J. O., Chan, D. Y. C. & Thoroddsen, S. T. *Nature*, 2012, Vol. 489, 274–277.
- ⁷⁶ Xiaoxue Zhang; Ling Wang; Erkki Levanen, *Superhydrophobic surfaces for the reduction of bacterial adhesion*, *RSC Advances*, 2013, Vol. 3, 12003
- ⁷⁷ P. Tang; W. Zhang; Y. Wang; B. Zhang; H. Wang; C. Lin; L. Zhang, *Effect of superhydrophobic surface of titanium on Staphyococcus aureus adhesion*, *J. Nanomater*, 2011, 178921.
- ⁷⁸ Jianyong Lv; Yanlln Song; Lei Jiang; Jianjun Wang, *Bio-Inspired strategies for Anti-icing*, *ACS Nano.*, 2014, Vol. 8 (4), 3152-3169.
- ⁷⁹ Richard D; Clanet C; Quere D, *Surface Phenomena Contact Time of a Bouncing Drop*, *Nature*, 2002, Vol. 417, 811-812.
- ⁸⁰ Clanet C; Beguin C; Richard D; Quere D, *Maximal Deformation of an Impacting Drop*, *J. Fluid Mech.*, 2004, Vol. 517, 199-208.
- ⁸¹ Mishchenko L; Hatton B; Bahadur V; Raylor J; Krupenkin T; Alzenberg J, *Design of ice-free Nanostructured Surfaces Based on Repulsion of Impacting Water droplets*, *ACS Nano*, 2010, Vol. 4, 7699-7707.
- ⁸² Bhushan B; Jung YC, *Wetting Study of Patterned Surfaces for Superhydrophobicity*, *Ultramicroscopy*, 2007, Vol. 107, 1033-41.
- ⁸³ Martines E; Seunarine K; Morgan H; Gadegaard N; Wilkinson CDW; Ridhle MO, *Superhydrophobicity and Superhydrophilicity of Regular Nanopartterns*, *Nano Lett*, 2005, Vol. 5, 2097-2103.
- ⁸⁴ Shan Peng; Xiaojun Yang; dong tian; Wenli Deng, *Chemically Stable and Mechanically Durable Superamphiphobic Aluminum Surface with a Micro/Nanoscale Binary Structure*, *ACS Appl. Mater. Interfaces*, 2014, Vol. 6, 15188-15197.
- ⁸⁵ A. Y. Vorobyev; Chunlei Guo, *Multifunctional Surfaces Produced by Femtosecond Laser Pulses*, *J. Appl. Phys.*, 2015, Vol. 117, 033103
- ⁸⁶ Klein RJ; Biesheuvel PM; Yu BC; Meinhart CD; Lange FF, *Producing superhydrophobic surfaces with nano-silica spheres*, *Z. Metallkd*, 2003, Vol. 94, 377-380.
- ⁸⁷ Tykhon Zubkov; Dirk Stabhl, Tracy L. Thompson; Dimitar Panayotov; Oliver Diwald; John T; Yates Jr, *Ultraviolet Light-Induced Hydrophilicity Effect on TiO₂ (110) (1x1)*.

Dominant Role of the Photooxidation of Adsorbed Hydrocarbons Causing Wetting by Water Droplets, J.Phys. Chem.B, 2005, Vol. 109, 15454-15462.

⁸⁸ *Han Gao; Bing Qiao; Ting-Jie Wang; Dezheng Wang; Yong Jin, Cerium Oxide Coating of Titanium Dioxide Pigment to Decrease Its Photocatalytic Activity, Ind. Eng. Chem. Res, 2014 Vol. 53, 189-197*

⁸⁹ *S.P.S. Badwal; D. Fini; F. T. Ciacchi; C. Munnings; J. A. Kimpton; J. Drennan, Structural and Microstructural Stability of Ceria-gadolinia Electrolyte Expose to Reducing Environments of High Temperature Fuel Cells, J. Mater. Chem. A, 2013 (1), 10768-10782.*

VITA

NAME: Sin Pui Fu

EDUCATION: B.S., Mechanical Engineering, University of Illinois at Chicago (UIC), Chicago, Illinois, 2012

Ph.D., Mechanical and Industrial Engineering, University of Illinois at Chicago (UIC), Chicago, Illinois, 2016

EXPERIENCE: Teaching Assistant for the course of introduction in engineering design, UIC, Fall and Spring 2011-2016

Interdisciplinary Product Development-Dunkin Donut and prince Castle LLC – Innovation of Sandwich Station, 2013-2014

Feedman Seating Company – Dynamic Impact Testing Modeling and Experimental Design of Aries Seat, 2011-2012

Dissemination of Research:

1. On the Wetting Behavior of Ceria Thin Films Grown by Pulsed Laser Deposition, Sin-Pui. Fu, J. Rossero, C. Chen, C. Takoudis and J. T. Abiade, submitted to *Scientific Reports*.
2. Fouling Induced Hydrophobicity of Mixed Oxide Thin Films Prepared by Pulsed Laser Deposition, Sin-Pui Fu, Chen Chen and J. T. Abiade, submitted to *ACS Applied Materials & Interfaces*.

FELLOWSHIP: Faydor Litvin Fellowship, UIC, 2012

MEMBERSHIP: ASME, First Robotics Coordinator, UIC, 2012